LBL-28926
Preprint

Lawrence Berkeley Laboratory
UNIVERSITY OF CALIFORNIA

Materials & Chemical
Sciences Division

Submitted to the Journal of Chemical Physics

Crossed Molecular Beams Study of the Reaction $D + H_2 \rightarrow DH + H$ at Collision Energies of 0.53 and 1.01 eV

R.E. Continetti, B.A. Balko, and Y.T. Lee

April 1990

Prepared for the U.S. Department of Energy under Contract Number DE-AC03-76SF00098.

DISCLAIMER

LBL-28926

Crossed Molecular Beams Study of the Reaction $D + H_2 \rightarrow DH + H$ at Collision Energies of 0.53 and 1.01 eV

R.E. Continetti, B.A. Balko, and Y.T. Lee

Department of Chemistry
University of California

and

Materials and Chemical Sciences Division
Lawrence Berkeley Laboratory
University of California
Berkeley, CA 94720

This work was supported by the Director, Office of Basic Energy Sciences, Chemical Sciences Division of the U.S. Department of Energy under Contract No. DE-AC03-76SF00098.

Crossed Molecular Beams Study of the Reaction $D + H_2 \rightarrow DH + H$ at Collision Energies of 0.53 and 1.01 eV.

R.E. Continetti, B.A. Balko and Y.T. Lee,

Department of Chemistry, University of California at Berkeley and

Materials and Chemical Sciences Division, Lawrence Berkeley Laboratory,

Berkeley, CA 94720

Abstract

This paper reports the first extensive product differential cross section (DCS) measurements for the $D + H_2 \rightarrow DH + H$ reaction with sufficient resolution to resolve product DH vibrational states. Using a D-atom beam produced by the photodissociation of DI at 248 nm, product velocity and angular distributions were measured at 12 laboratory (LAB) angles at a nominal collision energy of 0.53 eV and at 22 LAB angles at a nominal collision energy of 1.01 eV with a crossed-molecular beams apparatus. After correction of the raw product time-of-flight (TOF) spectra for modulated background, a comparison with recent exact quantum mechanical scattering calculations was made using a Monte Carlo simulation of the experimental conditions. The simulation showed that although the theoretical predictions qualitatively agree with the measurements, some significant discrepancies exist. Using the Monte Carlo simulation, a best-fit set of DH(v,J) DCS's which showed good agreement with the measurements was found. At the detailed level of the state-to-state DCS significant differences were observed between theory and experiment for rotationally excited DH(v,j) products. These results suggest that some regions of the current *ab initio* H_3 potential energy surfaces, particularly the bending potential at high energies, may need further examination.

1. Introduction

Studies of the hydrogen exchange reaction $H + H_2 \rightarrow H_2 + H$ have played a fundamental role in the development of both exact and approximate theories of chemical reaction dynamics. The potential energy surface on which this reaction occurs is the best known for any chemical reaction between neutral species[1,2], and, within the last year exact 3-D quantum scattering calculations have become possible for the isotopic variant $D + H_2 \rightarrow DH + H$[3,4]. Several experimental studies have been aimed at testing the theoretical predictions of the dynamics of the hydrogen exchange reaction, including measurements of reaction rate constants[5], product-state distributions[6,7] and product differential cross sections (DCS's).[8,9,10,11,12] A detailed dynamical observable, the product vibrational state-resolved DCS, has only recently become measurable[13,14]. DCS measurements provide a stringent test of *ab initio* potential energy surfaces and scattering calculations for this fundamental elementary reaction. In this paper, extensive DCS measurements with product vibrational-state resolution on the reaction $D + H_2 \rightarrow DH + H$ at nominal collision energies of 0.53 and 1.01 eV are reported and compared with recent theoretical predictions.

1.1. Theoretical Progress

Theoretical calculation of the H_3 potential energy surface (PES) started as early as 1929[15], and the landmark paper by Eyring and Polanyi[16] on the hydrogen atom exchange reaction in 1931 initiated the field of chemical reaction dynamics. Since that time, considerable progress has been made on the calculation of an accurate PES.[17] Currently, two analytic fits to *ab initio* energies calculated for several hundred H_3 configurations are available, the LSTH (Liu-Siegbahn-Truhlar-

Horowitz)[1] and DMBE (Double Many-Body Expansion)[2] PES's. These surfaces are very similar, indicating a minimum energy path in which the atoms are collinear, and are both, in principle, 'chemically' accurate within the Born-Oppenheimer approximation for the configurations represented by the *ab initio* points. The LSTH PES has a smaller root-mean-square error relative to the calculated *ab initio* energies for H_3 configurations near the threshold for the reaction, however, the collinear barrier on this surface is 9.80 kcal/mol, 0.15 kcal/mol higher than that given by the most recent ab initio calculations[18] and Quantum Monte Carlo calculations[19]. The DMBE PES fits a slightly larger set of *ab initio* configurations, including more bent configurations, and also has the correct symmetry properties to account for the conical intersection with the first excited electronic state of H_3. Figure 1 illustrates the energetics of the hydrogen exchange reaction for the D + H_2 isotopic combination, including the reaction threshold and the classical barrier height for the collinear configuration.

The H_3 system has seen considerable use as a theoretical prototype for the development of approximate theories of chemical dynamics. Several groups have carried out extensive quasi-classical trajectory (QCT) studies of the D + H_2 → DH + H reaction in the last decade[20,21,22], calculating product-state distributions (integral cross sections), and DCS's over a range of collision energies. These studies have confirmed the earlier finding by Karplus and coworkers[23] that the D + H_2 → DH + H reaction is dominated by collinear collisions near threshold, giving direct backward-scattering of the DH product, with progressively more sideways/forward scattering as the collision energy increases. A variety of approximate quantum-mechanical scattering treatments have also been applied to the H_3 system in general, including the D + H_2 → DH + H isotopic variant.[24] The recent advances in exact quantum scattering calculations finally make a solid benchmark available with which to interpret the accuracy of the various approximate methods.

Exact 3-D quantum scattering calculations were first performed on the hydrogen exchange reaction at low energies by Schatz and Kuppermann some time ago[25], however, the extension of such calculations to higher energies and the other isotopic variants of this reaction was not trivial. The development of new computational algorithms allowed Zhang and Miller to perform the first fully converged 3-D quantum calculations on the H + H_2 reaction at energies up to 1.3 eV in 1988,[26] and these results were subsequently confirmed using a different approach by Manolopoulos and Wyatt.[27] Fully converged 3-D quantum scattering calculations on the D + H_2(v=0,j=0) → DH(v,j) + H reaction based on the LSTH PES were recently published by Zhang and Miller (ZM).[3] These results represent one of the most extensive sets of calculations on the dynamical attributes of an elementary reaction to date, and provide an excellent database with which to compare the experimental DCS's presented in this paper. Recent results by Zhao, Truhlar, Schwenke and Kouri (ZTSK) have confirmed the results of ZM and provided additional predictions of the D + H_2(v=0,j=0,1) → DH(v,j) + H dynamics on the DMBE PES.[4] The DH(v,j) DCS's for the H_2(j=0) reaction calculated by these two groups on these two similar PES's are in good agreement, with all of the qualitative features of the DCS reproduced in both calculations. The agreement between the calculations is not quantitative, however, indicating the effect of the minor differences in the PES's.

1.2. Experimental Progress

Great effort has been devoted to measurements of dynamical observables to compare with the detailed theoretical predictions available for the hydrogen exchange reaction. In the last 60 years, improved experimental techniques have allowed chemists to go beyond the measurement of rate constants for the reaction,

to product-state distributions (PSD's) and finally to product state-resolved DCS's. DCS measurements as a function of scattering angle are one of the most sensitive probes of the reaction dynamics, particularly when they can be measured for individual product quantum states. However, such measurements have been traditionally difficult to make on the D + H_2 reaction for several reasons. Intense D atom beams with sufficient kinetic energies to overcome the potential energy barrier are difficult to generate with well-defined velocity distributions, the cross section for the reaction at ≈ 1 eV collision energy is only ≈ 1 $Å^2$, and ambient and beam-correlated DH produce large background signals in mass spectrometric detectors. However, with the powerful pulsed UV lasers available today, photodissociation of the hydrogen halides or hydrogen sulfide has become a viable option for the generation of intense, nearly monoenergetic pulsed beams of H or D atoms. This development is now making a new generation of molecular beam experiments on the hydrogen exchange reaction possible.

In spite of the difficulties associated with crossed molecular beams studies of the hydrogen exchange reaction, some of the earliest crossed beams machines were used to study it.[28] By 1970, a study of the product angular distribution for the D + H_2 → DH + H reaction at $\langle E_c \rangle$ = 0.48 eV was published.[8] The broad collision energy distribution and the lack of product velocity measurements prevented any DH(v,j) product-state resolution in the experiment, however, the results showed that the product DH was directly backward scattered in the center-of-mass (CM) frame at the low mean collision energy. More recently, Kwei and Lo[9] reported angular distribution measurements for the reaction T + H_2 → TH + H at E_{rel} = 0.70 eV. This study made use of a radiochemical technique for measuring the scattered TH, and showed that the TH products were also directly backward scattered in the CM at this higher collision energy.

The first extensive measurements of product velocity-angle distributions for the D + H_2 → DH + H reaction were reported in 1986 by Goetting, Mayne and Toennies.[10] Using a high-intensity arc-heated D atom beam crossed with a dense, cryogenically cooled H_2 beam, time-of-flight (TOF) spectra of the laboratory (LAB) velocity distributions at 16 LAB angles were measured at $\langle E_c \rangle$ = 1.5 eV. Arc-heated beam sources operate at extremely high temperatures, and the D-atom beam unfortunately had a very broad velocity distribution ($\Delta v/v \approx 1$), precluding resolution of DH vibrational states in the TOF spectra. At the elevated nominal collision energy of 1.5 eV, the DH-product CM angular distribution was seen to peak near $\theta_{cm} \approx 90°$, in accordance with QCT predictions on the LSTH PES.[20]

Toennies' group has also reported product angular distributions for the D + H_2(v=1) → DH + H reaction.[11] In this experiment, a high temperature nozzle produced H_2(v=1) which was crossed with a thermal D-atom beam produced in a microwave discharge. The H_2 beam, in addition to containing a large fraction of H_2(v=0), had a broad distribution of rotational states populated, so these experiments have only been compared to QCT predictions to date, since quantum mechanical predictions are not available for such a wide range of reagent states. These measurements were also found to be in good agreement with QCT calculations, given the level of averaging inherent in the experiment.

The first product velocity distribution measurement on the reaction D + H_2 → DH + H which showed product vibrational-state resolution was reported for limited scattering angles by Buntin, Giese, and Gentry in 1987.[13] In their experiment, energetic D atoms were produced by the photodissociation of D_2S at 193 nm. DH TOF measurements were made at LAB angles which probed backward-scattered DH(v=0) and DH(v=1) products at collision energies of 0.85, 0.95, 1.05 and 1.20 eV. However, the long counting times required precluded measurements of the product angular distributions.

Progress has also been made in measuring PSD's for the isotopic variants of the hydrogen exchange reaction as a function of collision energy. Until recently, such measurements were not available due to the difficulties associated with spectroscopic probing of the H_2 molecule. Recent advances in non-linear spectroscopies such as Coherent Anti-Stokes Raman Scattering (CARS) and Resonance-Enhanced Multiphoton Ionization (REMPI) have solved this problem, making PSD measurements possible on the H_2 molecule and its isotopic variants. Zare's group was the first to report REMPI measurements of the DH PSD's for the H + $D_2 \rightarrow$ HD + D reaction at collision energies of 0.55 and 1.30 eV in 1984.[6] Valentini's group nearly simultaneously reported the first CARS measurements of the DH PSD's for this reaction.[7] Careful calibration of the REMPI signals has resulted in near-quantitative agreement between the two techniques for this isotopic variant of the reaction.

Both the REMPI and the CARS measurements have been extended over a wider range of collision energies, and to other isotopic variants. In particular, the CARS technique has been applied to the measurement of the PSD's of the D + $H_2 \rightarrow$ DH + H reaction at E_c = 0.67 and 0.79 eV[29], and the REMPI technique has recently been applied to the D + H_2(v=0) and D + H_2(v=1,j=1) $\rightarrow$ DH(v=1,j) + H reactions at E_c = 1.32 eV (see discussion).[30] An extensive study of the energy dependence of the PSD's for the H + $H_2 \rightarrow H_2$ + H reaction has yielded experimental evidence which suggests the occurrence of dynamic resonances.[31] Although these resonances, as manifested in the sharp features shown in the energy dependence of the reaction cross section, were first predicted theoretically in one-dimensional quantum scattering calculations, fully converged 3-D quantum scattering calculations have shown that these effects should 'wash-out' in 3-D, and not be observable in the PSD measurements.[26,27] This discrepancy between theory and experiment is currently the subject of considerable controversy.

2. Experimental

The general features of the high-resolution universal crossed-molecular-beams apparatus used in these studies have previously been described in detail.[32] A full description of the modifications made to the basic apparatus for these pulsed-molecular beam scattering experiments has also been previously given[33], but the salient points will be reviewed here. A schematic view of the experimental arrangement is shown in Figure 2. A pulsed D-atom beam was produced by crossing a deuterium iodide (DI) beam with an excimer laser. The D-atom beam was subsequently collimated by a set of three defining apertures. After travelling 48.3 mm, the D-atom beam crossed a pulsed H_2 molecular beam orthogonally in the main scattering chamber, which had a working pressure of $\approx 1 \times 10^{-6}$ torr H_2 with both the DI photolysis target beam and the H_2 molecular beam running. The scattered DH products entered the detector by first passing through a slot in a synchronized chopping wheel (not shown) and then a small tube attached to the face of the detector (not shown). This chopper served to gate the detector opening, reducing the gas load on the detector and thus, the background count rate at m/e = 3. A schematic timing diagram for the experiment is shown in Figure 3.

The apparatus was equipped with a triply differentially pumped UHV detector which rotated about the beam crossing point in the plane defined by the atomic and molecular beams. Each of the three pumping stages were pumped by 220 l/sec ion pumps, with 400 l/sec magnetically suspended turbomolecular pumps (Seiko-Seiki) assisting in the second and third (ionization) regions. The detector had a nominal angular resolution of 1.25°. DH products travelled 34.3 cm from the center-of-rotation to the electron-impact ionizer. The uncertainty in the flight path was about .75 cm, predominantly due to the size of the ionizer. The DH products

were ionized, mass selected with a quadrupole mass spectrometer and counted with a Daly-type ion counting assembly.[34] A custom-built 4096 channel multi-channel-scaler (MCS) recorded the TOF of the ions relative to the dissociation laser pulse. The TOF of the neutral DH products from the interaction region to the ionizer, and, therefore, the DH product velocities, were then determined. An LSI-11/73 microcomputer interfaced to the MCS via a CAMAC crate controlled data acquisition.

2.1 D-Atom Beam Source

The D-atom beam was generated by the photodissociation of DI in a differentially pumped region consisting of a large chamber pumped by a VHS-10 10" diffusion pump (DP) and two liquid-N_2-cooled cryo-panels, with a smaller photolysis chamber nested within. The photolysis chamber was pumped by a VHS-4 4" DP and one liquid-N_2-cooled cryo-panel. The 248 nm KrF output from a Lambda Physik EMG 202 MSC excimer laser was crossed with a pulsed beam of DI produced by expansion of 140 torr DI through a 0.75 mm aperture. A home-built piezoelectric pulsed valve, based on the design of Proch and Trickl[35], was used to generate the DI target beam. The output of the excimer laser was polarized by a 10-plate Brewster angle stack polarizer. The polarizer attenuated ≈ 55 % of the beam, leaving light with better than 95 % polarization. Under typical operating conditions, the laser delivered ≈ 140 mJ of polarized 248 nm light to the photolysis volume. Using an Applied Photonics C-5000 gas processor, constant laser power could be maintained with the laser's ILC feedback circuit (Lambda Physik) for in excess of 1 million shots (≈ 3 hours at 100 Hz). The laser beam was focussed to a 3 x 3 mm spot at a distance of 3 mm from the nozzle aperture with two uncoated fused silica cylindrical lenses of focal length (fl) 19 and 24 cm. The liquid-N_2-cooled cryo-panels reduced the rate at

which pump oil and iodine contaminated the 19 cm fl lens, which also formed the vacuum seal through which the laser beam passed.

TOF spectra of the D-atoms produced with the laser polarization parallel and perpendicular to the direction of detection (and beam propagation) are shown in Figure 4. These spectra were recorded by rotating the mass spectrometric detector to look into the D-atom beam. Two peaks, due to the production of both $I(^2P_{3/2})$ and $I(^2P_{1/2})$ in the UV photodissociation of DI, are observed in the TOF spectra. As the polarization dependence observed in the TOF spectra show, the ground-state $I(^2P_{3/2})$ channel results from a perpendicular dissociative transition and the $I(^2P_{1/2})$ channel results from a parallel transition.[36] Ideally, with perfect polarization of the laser and in the absence of any curve-crossing in the dissociation of DI on a repulsive excited-state surface, the D atoms correlated with these two processes could be completely spatially separated.[37] However, in practice, the D-atom TOF spectra are broadened by collisions in the free-jet after dissociation, with an additional underlying broad component apparently due to D atoms produced by the exchange reaction D + D'I → D' + DI. [33] Although this effect was undesirable, beam intensity requirements made it necessary to operate the beam source under these conditions. The solid-line fits to the TOF spectra were generated with a modified version of the Monte Carlo program used to simulate the reactive scattering data.[33] This program also generated a D-atom number-density velocity distribution corrected for all apparatus averaging effects which was used in the simulation of the reactive scattering data. The D-atom beam velocity distribution parameters are summarized in Table 1. Photodissociation of DI and the other hydrogen halides under single collision conditions was used to calibrate the TOF measurements, providing information on the product flight length, ion flight time and the effective size of the ionizer. The D-atom beam was collimated to a nominal point-source angular divergence of ≈ 6°. DI of ≈ 97 % isotopic purity was synthesized as needed by

combination of the elements over a platinum catalyst.[33] The DI cylinder was maintained at a temperature of - 55°C.

2.2 H_2 Beam Source

A piezoelectric pulsed valve[36] with a 0.5 mm diameter nozzle placed 18 mm from a 1.5 mm diameter home-made electroformed skimmer was used to generate the H_2 beam, with an H_2 stagnation pressure of 1200 torr. The distance from the skimmer opening to the crossed-beams interaction region was 12.5 mm. The pulsed H_2 beam had an angular distribution characterized by a full-width at half-maximum (FWHM) of 8°. The velocity distributions of the para- (p-) and normal- (n-)H_2 beams, summarized in Table 1, were measured with a synchronous TOF technique, which enabled measurement of the velocity distribution as a function of time in the gas pulse. The results of Pollard, *et. al.* indicate that under these expansion conditions, the p-H_2 beam contained approximately 20 to 30 % H_2 (j = 2), with the balance in j = 0, while the n-H_2 beam contained H_2(j=0:1:2) in the ratio 18:75:7 %.[38] The pulsed-beam temporal profile in the free jet had a FWHM of ≈ 175 μsec, while the portion of the beam transmitted through the skimmer had a FWHM of ≈ 80 μsec. P-H_2 was made by the U.C. Berkeley Dept. of Chemistry Low Temperature Laboratory. The source chamber was pumped by a VHS-10 10" DP backed by a Roots-blower mechanical pump combination, and a VHS-4 4" DP.

2.3 DH Product TOF measurements

DH product (m/e=3) TOF spectra were recorded as a function of LAB scattering angle at the nominal collision energies E_c = 0.53 and 1.01 eV. The highest signal intensities observed were only ≈ 2 x 10^{-3} ion counts/0.9 μsec time bin/laser

shot. Once the operating conditions had been optimized, ≈ 210 hours of actual reactive scattering data for the D + p-H_2 reaction and ≈ 120 hours of data for the D + n-H_2 reaction were acquired over a period of three months. The piezoelectric crystal in the DI pulsed-beam source degraded with time and had to be replaced after ≈ 100 million shots, however, the H_2 beam source produced in excess of 250 million shots without failure or readjustment. The performance of the excimer laser degraded significantly over the course of the measurements. Initially, the laser was able to deliver 350 mJ/pulse of unpolarized 248 nm radiation at a repetition rate of 100 Hz for up to 30 hours without cleaning of the output coupler and high reflector. By the end of the study the laser was delivering only ≈ 250 mJ/pulse, and the output coupler or the high reflector had to be cleaned alternately every 12 hours. The excimer laser lenses also required routine maintenance. After an experimental run of ≈ 80 hours, the lens transmission would decrease to ≈ 2/3 of its normal, 'clean' value. The scattering chamber had to be vented for lens cleaning.

A typical experiment began with measurement of the D-atom beam intensity. Attenuation of the D-atom beam by the H_2 beam was then measured to check the H_2 beam intensity and verify that the experimental timing was correct. The measured attenuation of the D-atom beam by the H_2 beam was typically 5% or less. Once the two beams were crossing under the desired conditions, reactive scattering data acquisition was begun. A TOF spectrum was first recorded at a reference LAB angle for 2×10^5 pulses (33.3 minutes at a data acquisition rate of 100 Hz). LAB angles of 27.5° and 32° were used as reference angles for the E_c = 1.01 eV reaction, while 40° was used as the reference angle for the E_c = 0.53 eV reaction. TOF spectra at three other LAB angles were then measured, followed by the reference angle. This cycle was then repeated until the laser gas needed changing (≈ 3 to 5 hours). Either nominal collision energy could be chosen by simply rotating the transmission polarizer, without any laser realignment required. Two background measurements

were also done routinely. The signal at m/e = 3 coming solely from the D-atom beam was measured without the H_2 beam running. This measurement was done occasionally, with typically at least one LAB angle recorded per laser gas fill. While the laser gas was being changed, the signal due to the H_2 beam alone was measured. In addition, the D-atom beam intensity was also monitored periodically.

Due to the low signal levels, the quality of the data was strongly dependent on the background count rate in the mass spectrometer at m/e = 3. With the gated detection scheme that was used, a count rate of 1.8 kHz at m/e = 3 was achieved at the beginning of an experimental run. The inherent m/e = 3 background in the detector alone gave count rates of ≈ 1.5 kHz. During a long experiment the m/e = 3 count rate would slowly rise due to the buildup of DH in the chamber.

3. Results

3.1 Reactive Scattering TOF Data

In Figures 5(a) - 5(c), representative raw TOF spectra at m/e = 3 for the reaction at E_c = 1.01 eV are shown, while in Figures 5(d) - 5(f), representative data for the E_c = 0.53 eV reaction are shown. The data are normalized to the signal observed in 2×10^5 laser shots, with the constant background subtracted. These spectra are six channel averages of the 0.15 μsec dwell-time raw data, so each point on the spectra represents the signal arriving in a 0.9 μsec TOF bin.

The raw data are contaminated by two types of modulated background. The large signal at long flight times in all the spectra is correlated with the H_2 molecular beam, and does not depend on the presence of the crossed D-atom beam. As the H_2 beam entered the scattering chamber, some collisions occurred in the beam and at the walls of the scattering chamber, causing H_2 (and isotopic impurity DH) to scatter

into the detector. This background signal generally arrived at longer flight times than the reactively scattered signal, except in the case of the slow products of the E_c = 0.53 eV reaction. To account for this background component, TOF data with only the H_2 beam running was collected for all LAB angles, and subsequently fit to allow correction of the raw reactive scattering TOF data. A linear polynomial least-squares fitting routine, (typically using a 9th-order polynomial), was used to fit the H_2 beam data at each LAB angle. Any spurious oscillations in the leading baseline of the polynomial fit were removed. Figure 6(a) shows an example of the fit to the m/e=3 H_2 beam-correlated background at a LAB angle of 27.5°. The intensity of the H_2 beam-correlated background increased considerably beyond 50°, causing a significant rise in the m/e=3 count rate, which made scattering measurements increasingly difficult at wider LAB angles.

A significant difference was observed in the raw TOF spectra for D + n-H_2 and D + p-H_2 at long flight times as shown in Figure 7. The reactive signal intensity did not differ for n-H_2 or p-H_2, but, the H_2 beam-correlated background was significantly lower in the D + p-H_2 experiment under otherwise identical operating conditions. This difference observed in the modulated background at m/e=3 from the n-H_2 and p-H_2 beam is puzzling because the beam intensities and DH impurities were found to be the same in both the p-H_2 and n-H_2 beams. A gas-dynamic effect involving more effective rotationally inelastic collisions of DH with H_2(j=2) in the p-H_2 beam leading to DH depletion by scattering out of the beam in the free-jet expansion (before skimming) is a possible explanation for this observation.[33]

The other type of modulated background in the TOF spectra was due to fast DH impurity in the D-atom beam. Exoergic H/D-atom abstraction reactions with unphotolyzed DI/HI precursor molecules generated DH with a wide distribution of velocities and internal energies.[39, 40] Due to the large velocities of the DH (up to 10^6 cm·sec^{-1}), signal from this impurity made contributions to the TOF spectra in

the same time frame as the reactively scattered DH. This signal was observed at all LAB angles even without a crossed-beam, as some of this DH scattered off of the beam-defining apertures and other surfaces into the detector. The intensity of this background signal was strongly dependent on the time delay between the firing of the DI pulsed beam and the photolysis laser. In addition, the signal was dependent on the laser power. For this reason, the magnitude of this background signal tended to vary, so measurements had to be made during every experiment. Reactions of the D-atom beam at surfaces inside the scattering chamber and the detector almost certainly contributed to this background at longer flight times. A representative TOF spectrum showing the DH from the D-atom beam at a LAB angle of 17° along with the polynomial fit used is shown in Figure 6(b). The intensity of this background decreased considerably beyond 15°, however, the shape of this background did not change noticeably at large LAB angles.

Examination of the reactive scattering TOF data showed that the DH scattered out of the H_2 beam and the fast DH present in the D-atom beam could not account for all of the modulated background, due to elastic and inelastic scattering of the DH impurity in the D-atom beam off of the H_2 beam. At LAB angles less than 15° this was a significant problem, as a fast elastic scattering peak was observed which was difficult to model or measure independently of the D + H_2 experiment. For LAB angles greater than this, test measurements done by scattering the DH and D_2 impurities present in the D-atom beam off of either a He or H_2 secondary beam, respectively, showed that the signal with the crossed beam on had a shape indistinguishable from that measured with only the D-atom beam on.[33] As an example of these tests, Figure 8 shows the magnitude of the TOF signals observed for reactively scattered D + p-H_2 → <u>DH</u> + H compared to DH + He → <u>DH</u> + He at a LAB angle of 27.5°. Some broad DH signal is observed from DH + He collisions, but the magnitude is significantly lower than that recorded in the reactive scattering of

D + H_2. The dashed-line fit to the DH + He spectrum was generated by appropriately scaling the polynomial fit to a DH TOF spectrum measured at this LAB angle with only the D-atom beam on. The fit is quite good, specifically, no significant signal was observed from DH + He scattering at this LAB angle at flight times less than 80 μsec, which is where the most significant differences between the theoretical predictions and the experiment lie. These test measurements indicated that at LAB angles greater than 15°, the shape of the fast DH background signal could be accurately accounted for using the DH spectra measured with only the D-atom beam on.

3.2 Correction of the Reactive Scattering TOF Data

The modulated background signals were stripped from the raw reactive scattering TOF spectra by simultaneously scaling the fits to the background from the H_2 and D-atom beams to the raw DH TOF spectra at flight times beyond those kinematically allowed in the D + H_2 reactive collisions. The kinematics of the D + H_2 reaction dictate that the slowest DH products from a 0.53 eV collision have a velocity of $\approx 2 \times 10^5$ cm·sec^{-1}, which corresponds to a TOF of 175 μsec. Lower energy collisions also occur, but at flight times in excess of 200 μsec, the reactive scattering signal must go to zero due to the requirement of kinetic energy to overcome the large barrier for the hydrogen exchange reaction. The TOF spectra at a given LAB angle for a given experimental run were combined before stripping the background from the data. Since the intensity of the D-atom-beam-correlated background tended to vary between experiments, the results from individual experiments were stripped individually and then added together to give the final TOF spectra shown in Figures 10 and 12.

The kinematic diagram shown in Figure 9 illustrates the relationship between the CM and LAB frames for this reaction and allows qualitative interpretation of the LAB TOF spectra. The corrected TOF spectra at 22 LAB angles for the E_c = 1.01 eV reaction are shown in Figure 10. These spectra represent the summed results of six major experimental runs for D + p-H_2. For example, the spectrum at 27.5° represents 30 hours of signal averaging. Consideration of Figure 9 shows that at a LAB angle of 27.5°, for example, four peaks might be observed in a TOF spectrum, corresponding to the forward and backward scattered DH(v=0) and DH(v=1). Examination of the TOF spectra indicate that the backward scattered DH(v=0) and DH(v=1) states are resolved, most notably from 23° to 32°. The high LAB-velocity forward-scattered signal is compressed into fewer TOF channels, though, and the resolution is not sufficient to resolve the DH(v) states in the forward direction. At the LAB angles closer to the D-atom beam (10°, 12° and 14°), a fast narrow peak corresponding to DH scattered as far forward as θ_{cm} = 20° is observed, followed by a large, broad signal due to reactive scattering and elastic scattering of DH impurity in the D-atom beam. At wide angles (Θ_{LAB} = -14° and 50°, for example), the forward/backward structure in the TOF spectra disappears as the edge of the CM recoil velocity circle is reached. The shape of the slow TOF signal in the small LAB angle data has the greatest uncertainty due to the significant background corrections which were necessary in the angular range < 20°.

Figure 11 shows a typical kinematic diagram for collisions near 0.5 eV. The corrected TOF spectra at 12 LAB angles at E_c = 0.53 eV are shown in Figure 12. In spite of the much smaller reactive cross section at this lower collision energy, the observed signal is strong. This is due to the favorable kinematics that result from the smaller CM recoil velocities of the products. DH (v=1) has a small yield at this nominal collision energy, but a weak feature attributable to this state is observed at

LAB angles less than 32°. The amount of fast, forward scattered product is much lower at this collision energy.

3.3 Laboratory Angular Distributions

The LAB angular distributions were generated by integrating the corrected TOF spectra taken for both collision energies in one long experimental run. Each corrected 2×10^5 shot TOF spectrum was integrated individually, with the intensities time-normalized to the reference angles previously mentioned. The LAB angular distributions for the E_c = 1.01 and 0.53 eV reactions are shown in Figures 13 and 14. The error bars represent 90% confidence limits on 3 to 4 data points per angle. The angular distribution broadens considerably at the higher collision energy. Evidence of the elastic scattering of DH impurity in the D-atom beam is seen in the E_c = 1.01 eV angular distribution as a sharp rise in signal at small LAB angles. At larger LAB angles the background subtraction procedure removed all of this elastic scattering signal.

4. Analysis

Accurate inversion of LAB scattering data to the CM frame is a difficult proposition. Due to the finite resolution of the crossed beams and the detection scheme, the actual collision events are described by a multitude of kinematic diagrams. Use of a single-kinematic-diagram transformation from the LAB to the CM can yield qualitative insights to the nature of the DCS, especially in cases where the kinematics of the reaction are dominated by a well defined beam.[41] The results obtained by this low-level analysis of the data have been previously presented.[14,33] The most common approach to analyzing scattering data is the forward convolution

method, wherein predicted or guessed CM angular and velocity distributions are numerically averaged over the apparatus distributions and compared to the LAB data.[42]

4.1 Monte Carlo Simulation

An importance-sampling Monte Carlo algorithm based on the treatment of the CM→LAB transformation described by Pack[43] was used for the forward convolution of the theoretical state-to-state DCS's for the D + H_2 reaction. This program, which has been previously discussed in detail[44], took into account all aspects of the experimental averaging. The velocity and angular distributions of both beams, the resolution effects associated with the finite size of the D-atom source volume, the collision volume, and the detector ionization volume were treated explicitly. The LAB signal due to each state-to-state reactive cross section ($f \leftarrow i$) was calculated in turn, giving simulated TOF and angular distributions for comparison with the experimental data. Figure 15 gives a schematic flow-chart of the course of the Monte Carlo simulation. In short, the calculated TOF signal in an MCS channel centered in time at t_n at a nominal LAB angle Ω_0 for a given DH(v,j) final state is given by the integral

$$\overline{N}_{fi}^{lab}(\Omega_0,t_n) = \int dv_1 \int dv_2 \int d\vec{r}_S \int d\vec{r}_C \int d\vec{r}_D \cdot [U(t_{n+} - t_f) - U(t_{n-} - t_f)] \cdot P_1(v_1)\cdot P_2(v_2)\cdot P_S(\vec{r}_S)\cdot P_C(\vec{r}_C)\cdot P_D(\vec{r}_D)\cdot N_{fi}^{lab}(\vec{v}_1,\vec{v}_2,\Omega) \quad (2).$$

In this equation, the vectors $\vec{r}_S$, $\vec{r}_C$, and $\vec{r}_D$ refer to points in the D-atom source, scattering volume, and detection volume, respectively. The magnitude of the reagent velocities are given by v_1 (D) and v_2 (H_2), with the velocity vectors defined

by the chosen points in the apparatus volumes. The D-atom source density function $P_S(r_S)$ was determined by the overlap of the laser beam with the free-jet DI expansion. The scattering volume density function $P_C(r_C)$ was determined by the measured angular distribution of the H_2 beam and the angular distribution of the D-atom beam as defined by the collimating apertures. The ionization volume density function $P_D(r_D)$ was assumed to be Gaussian, with a FWHM along the product flight path of 0.5 cm as determined by calibrations with H-atom photofragment spectra. The U's are Heaviside step functions, which indicate that the signal goes in channel n if the flight time is between t_{n+} and t_{n-}, which define the width of the MCS channel in the simulation. The kinetic energy and TOF for the product molecule are determined by the incident particle velocities and any energy consumed or released in the reactive process yielding the final state under consideration, f . Finally, the number-density LAB-DCS associated with the particular reagent velocities and product recoil velocity is obtained from the theoretical CM DCS using the relation

$$N_{fi}^{lab}(\vec{v}_1,\vec{v}_2,\Omega_0) = \frac{v_{rel}\cdot v_{lab}}{u_3^2\cdot|\cos\zeta|} I_{fi}^{cm}(v_{rel},\theta_{cm}) \qquad (3).$$

In this equation, v_{rel} is the magnitude of the relative velocity, which weights the kinematic diagrams by the collision frequency. v_{lab} is the detected product LAB recoil velocity, u_3 is the detected product CM velocity, and ζ is the angle between these two vectors. These factors correspond to the Jacobian for the CM→LAB transformation for discrete exit channel velocities with number-density detection.[43] The input from the theoretical calculations is the DCS for a specific DH(v,j) state as a function of scattering angle and relative velocity; $I_{fi}^{cm}(v_{rel},\theta_{cm})$.

In an ideal experiment, the DCS would need to be known at only the two nominal collision energies to allow comparison with the experimental data. In fact the D-atom velocity distribution is composed of two sharp peaks associated with the two spin-orbit states of I atom, with a broad, underlying component due to collisions in the source volume. Thus, accurate simulation of the data requires a knowledge of the energy dependence of each of the DH(v,j) differential cross sections. ZM have provided the DH(v,j) differential cross sections at 15 total energies ($E_{tot} = E_c + E_{ZPE}$, where $E_{ZPE} = 0.27$ eV is the zero point energy for H_2) ranging from 0.40 eV to 1.35 eV, while ZTSK have provided DCS calculations for H_2(j=0 and 1) reagent at five energies from 0.82 to 1.35 eV. With these high quality theoretical predictions, a legitimate comparison with the LAB data was possible. Using a bicubic-spline fitting procedure, continuous DCS surfaces as a function of total energy and CM scattering angle were produced. With these surfaces, the Monte Carlo program could look up the DCS for any collision and product recoil angle encountered in the simulation. Several of the DH product DCS surfaces used in the simulation are shown in Figure 16.[33] Simulations made using the results of ZTSK were only performed for the E_c = 1.01 eV data. The lowest collision energy at which they provided DCS predictions was 0.55 eV, so the low energy DCS predictions of ZM were used in all simulations for collisions at energies less than 0.55 eV.

To check the accuracy of the Monte Carlo simulation program and the molecular beam apparatus, a study of the elastic scattering of H + He was made. Elastic scattering of D atoms at m/e = 2 was not measurable due to the large detector background. H atoms were produced by photolysis of HI, with the apparatus geometry the same as that used in the D + H_2 experiments. The H-atom beam velocity distribution used in the simulation of the elastic scattering was produced by a Monte Carlo simulation of the H-atom beam TOF. In Figure 17, the results of the simulation of the H + He TOF spectra using a hard-sphere DCS are shown. The

good agreement indicates that both the simulation program and the scattering apparatus were in good working order.

4.2 E_c = 1.01 eV Reactive Scattering Simulation

The results of the Monte Carlo simulation of the TOF spectra at E_c = 1.01 eV using the DCS results of ZM are shown in Figure 10. The comparison of the calculated and experimental LAB angular distributions are shown in Figure 13. The LAB angular distribution is normalized by the average scaling factor for the two LAB angles, 27.5° and 32°, as these are the best known experimental intensities. The calculated and experimental TOF spectra, however, are normalized to the peak intensities in each spectrum, with the relative intensities of the TOF spectra normalized to the measured LAB angular distribution. The simulation of the LAB angular distribution does not show major differences with the experimental data, given the signal-to-noise (S/N) of the data. The statistical error in the Monte Carlo simulation is in all cases much smaller than the experimental errors, and is not indicated in the figures. The TOF spectra provide a more stringent test of the theoretical DCS's. Significant differences are observed between theory and experiment in the TOF spectra at several LAB angles. The overall fit to the LAB TOF data is quite impressive, however. In particular, the shape of the fast, forward scattered signal and the relative intensities of the forward/backward scattering in the simulation fit the experimental results very well.

The most striking differences between the calculated and experimental TOF's are seen at LAB angles from 20° to 40°. At angles within this range, significantly more signal is observed at flight times corresponding to rotationally excited DH(v,j) products at CM angles mostly in the backward hemisphere ($\theta_{cm} > 90°$). At LAB angles less than 20°, a similar difference due to an increasing amount of DH elastic scattering at the smaller LAB angles is observed. The important point, here, though,

is that the relative intensity of the differences for LAB angles greater than 20° increases at larger LAB angles, where elastic scattering of DH impurity in the D-atom beam by H_2 molecules was shown to be insignificant. The theoretical predictions of ZM and ZTSK agree with each other for D + H_2(0,0) → DH(v,j) + H, with no significant differences observed in the simulations made with either set of predictions. In Figure 18, corrected TOF spectra for the D + n-H_2 reaction are shown at several LAB angles, compared with the theoretical predictions of ZTSK, assuming 75% H_2(j=1) and 25% H_2(j=0) reagent. These TOF spectra also show the same type of systematic discrepancies between theory and experiment observed in the D + p-H_2 data.

One feature that is evident in all of the E_c = 1.01 eV TOF spectra is a long tail in the data, extending out to flight times of ≈ 200 μsec. This signal is due to the presence of slower D atoms in the beam. At LAB angles beyond 40°, in particular, this slow component in the reactive signal becomes significant, since the signal from the E_c = 0.53 eV reaction peaks at larger LAB angles where the signal from 1.01 eV collisions is decreasing. The effect of the D-atom beam velocity distribution on the TOF data is dependent upon the DH(v,j) final state under consideration. Collision energy distributions weighted by the theoretical DCS were generated to illustrate this effect. In Figure 19, these distributions are compared to an unweighted collision energy distribution. As the figure shows, low j DH(v=0) product states have a significantly higher reactive cross section at the lower collision energies, accentuating the contribution from the reactions of the slow D atoms. For higher DH(v,j) states, the energetic threshold for reaction acts as an energy selector, and only the faster D atoms contribute. In the simulation, the few collisions that occurred with E_c > 1.1 eV were treated as having the same DCS as 1.1 eV collisions.

Attempts to fit the data by simply altering the relative magnitude of the integral cross sections for various DH(v,j) states were unsuccessful. Both the LAB

angular distribution and the TOF spectra were sensitive to changes in the peak of the rotational state distributions by ± 1 quanta. The differences between the simulation and the TOF spectra were not remedied by these changes, however. Increasing the DH(v=1) integral cross sections filled in some of the signal 'missing' in the simulations using the theoretical predictions. This reduced the quality of the fit for the slower, backward scattered DH(v=1) in the well-resolved spectra at Θ_{LAB} = 27.5°, 30° and 32°. Thus, it was concluded that changes in the state-to-state DCS's were necessary to fit the LAB data.

4.2.1 Best-Fit DCS at E_c = 0.98 eV

The differences between theory and experiment were fit using the Monte Carlo simulation program iteratively. This involved modifying the appropriate DH(v,j) DCS's and rerunning the simulation. The effect of the modifications was indicated by comparison with the experimental TOF and angular distributions. The TOF spectra were used as the most important criteria in the iterative fitting process, since they are much more sensitive to changes in the DCS and the S/N ratios for these spectra are typically higher than for the LAB angular distribution. The LAB angular distribution was very useful for ruling out certain changes in the DCS, however. For making a qualitative assessment of the necessary changes, the DCS was only modified at the point closest to the nominal collision energy at which theoretical predictions were available. Both ZM and ZTSK provided predictions at a total energy of E_{tot} = 1.25 eV, which corresponds to a collision energy of E_c = 0.98 eV, so further references to the comparison with the theoretical predictions will refer to this energy which is 0.03 eV below the nominal E_c, but within the FWHM of the E_c distribution. Both sets of theoretical predictions also included E_{tot} = 1.09 and E_{tot} = 1.35 eV, so changes made at E_{tot} = 1.25 eV influenced the DCS from E_{tot} = 1.09 to 1.35

eV when the spline-fit to the DCS was done in the Monte Carlo simulation. Since significant differences between theory and experiment were observed at angles beyond those where DH(v=1) and DH(v=2) made significant contributions, it was clear that the DH(v=0) differential cross sections needed to be modified. The approach taken was that DH(v=0,j) DCS's were modified first, with DH(v=1) and DH(v=2) DCS's modified only when necessary.

The DH(v,j) states responsible for the differences between theory and experiment may be determined by examination of the kinematic diagram for the E_c = 0.98 eV D + H_2 collisions. As an example, Figure 9 shows that with the detector at Θ_{LAB} = 27.5° the DH(v=0,j=10) circle is cut at both $\theta_{cm} \approx 95°$ (TOF ≈ 50 μsec) and $\theta_{cm} \approx$ 165° (TOF ≈ 75 μsec), while the DH (v=0,j=11) state is cut tangent to the CM-recoil-velocity circle at $\theta_{cm} \approx$ 120-140° (TOF ≈ 55 - 65 μsec). DH(v=1,j=5-7) products also contribute to the TOF signal in this range, so resolution of the DH(v,j) states was not possible with a non-state-selective detector. Although there is a significant broadening of the LAB data due to the various apparatus functions, this is the approach which was taken to identify the specific DH(v,j) DCS's which needed modification to account for the differences between theory and experiment.

The best-fits to the TOF spectra are shown in Figure 20, while Figure 21 shows the fit to the LAB angular distribution. The experimental TOF spectra are fit much better by the simulation with the best-fit DCS. The fit to the LAB angular distribution was not very sensitive to these changes, however. In the TOF spectra, the differences between simulation and experiment for the rotationally excited DH(v,j) products that arrive in the middle of the TOF spectra at LAB angles greater than 20° are removed with the modified DCS. The DH(v=2) integral cross section was also increased by a factor of three at E_{tot} = 1.25 and 1.35 eV in order to fit a weak feature attributable to DH(v=2) in the TOF spectra at LAB angles from 20° to 25°.

In Figure 22, the best-fit DCS results at E_{tot} = 1.25 eV are shown together with the predictions of ZM. The largest deviations between theory and experiment are observed for DH(v,j) final states from (v=0 , j=3) to (v=0 , j=11). Significant deviations were also observed for (v=0 , j=12) and (v=1, j= 0-8). The DCS curves for a given DH(v) state are plotted on the same relative scale to provide an idea of the significance of each state to the overall dynamics of the reaction. The higher DH(v,j) states are detected with greater sensitivity in a crossed-molecular-beams experiment due to the concentration of products in a smaller laboratory angular and velocity range caused by the smaller CM recoil velocities. For this reason, the changes in these DCS's, while small on a relative scale, were important for obtaining the best-fit.

The best-fit curves show that the higher DH(v,j) DCS's are generally broadened in the backward hemisphere ($\theta_{cm} > 90°$). More forward scattering, at CM angles as small as $\theta_{cm} = 60°$, was also required for several states, most notably DH(v=0,j=5 to 11). The best-fit DH(v=1,j) DCS's were in all cases more backward-peaked than the theoretical predictions. Due to the number of DH(v,j) states involved and the lack of rotational-state resolution in the experiment, these best-fit state-to-state differential cross sections cannot be said to be unique. The trends shown in the relative magnitude and CM angular range of the corrections to the theoretical DCS are accurate representations of the significance of the differences observed between the theoretical predictions and the LAB data. Changes in the shape of these curves on the order of ± 10 % led to a decrease in the overall quality of the fit.

4.2.2 Integral Cross Sections at E_c = 0.98 eV

Integration of the best-fit DCS curves yields the DH(v,j) rotational distributions shown in Figure 23, with the values given in Table 2. The relative integral cross sections for each vibrational-rotational state are obtained from the DCS by integration over CM scattering angle θ;

$$\sigma = 2\pi \cdot \int_0^{\pi} \sigma(\theta)\sin\theta d\theta \qquad (4).$$

The integral cross sections are much less sensitive to the differences between theory and experiment than the DCS. For DH(v=0) product , <j> = 6.7 for the best-fit DCS, while ZM's result[3] is <j> = 6.3 and ZTSK's result[4] is <j> = 6.2. Thus, the experimental result shows slightly more rotational excitation. Once the best-fit DCS was found, the easiest way to illustrate the sensitivity of the LAB data to the DCS was to alter the integral cross sections, keeping the shapes of the best-fit DCS's constant. Two arbitrary rotational distributions ('Cold' and 'Hot'), shown in Figure 23 and given in Tables 2 and 3 were used, which shifted the peak of the best-fit DH(v,j) rotational distributions by ± 1 quantum. As the TOF spectra at Θ_{LAB} = 27.5° and 32° shown in Figure 24 indicate, using these alternate rotational distributions noticeably degraded the fit to the data. The cold rotational distribution (<j> = 6.2, peak j = 6) showed too much backward-scattered DH(v=0) and DH(v=1) in the TOF spectra. The fit to the angular distribution (shown in Figure 21) was actually a little better than the best-fit DCS, however. The hot rotational distribution (<j> = 7.1, peak j = 8) caused the vibrational resolution for the DH(v=1) and DH(v=0) to wash out significantly in the 27.5° spectrum. In addition, the hot rotational distribution

had a significantly poorer fit to the angular distribution than the best-fit DCS. For DH(v=1,j) products the agreement between the experimental and theoretical integral cross sections was better, with the experimental result <j> = 3.4, ZM's result <j> = 3.2 and ZTSK's result <j> = 3.1.

As shown in Table 4, the experimental DH(v=1)/DH(v=0) branching ratio is 0.11, while the theoretical calculations predict DH(v=1)/DH(v=0) = 0.13.[3] This difference is probably not significant, however, due to the stated bias in the fitting procedure towards the DH(v=0,j) states. The DH(v=2,j) integral cross section three times higher than predicted was needed to fit the TOF data at LAB angles of 20° to 25°, at the peak of the DH(v=2) angular distribution in the theoretical simulation. The nominal collision energy is very close to the DH(v=2) energetic threshold, so rather than modifying the DCS at E_{tot} = 1.25 eV, the integral cross section was increased at both E_{tot} = 1.25 eV and 1.35 eV, since the higher energy collisions which occur are responsible for most of the DH(v=2) product. The difference in the electron-impact ionization cross section for DH(v=2) should not be significantly larger than that for DH(v=0) and DH(v=1) in view of the large H_2^+/H^+ ratio in the electron-impact ionization of the H_2 molecule[45] and the fact that the exciation energy in DH(v=2) is only a small fraction of the bond dissociation energy. In the case of vibrational excitation of the parent molecule (DH), fragmentation to daughter ions often becomes more important, which would actually decrease the detection efficiency for DH(v=2). However, there is no detailed data available on the relative electron-impact cross sections and fragmentation ratios for individual DH(v) states.

The most significant possible source of error in these measurements is the correction of the TOF data for the measured modulated background signals. However, the detailed test measurements on the background sources that were performed have allowed correction of the data with the true functional form of the

modulated background. Possible systematic errors arising from this part of the data processing will not be considered further. The ambiguities involved in generating the best-fit state-to-state DCS's from the rotationally unresolved TOF data are difficult to quantify. Significant changes in the magnitudes of the best-fit DH(v,j) DCS's cannot fit the data, but it would be difficult to express this in a compact form given the number of states involved.

4.3 E_c = 0.53 eV Reactive Scattering Simulation

The results of the Monte Carlo simulation with the predictions of ZM at the nominal collision energy of E_c = 0.53 eV are shown in Figure 12, with the comparison of the LAB angular distributions shown in Figure 14. The fit to the LAB angular distribution is good, given the S/N ratio of the experimental data. In the case of the TOF spectra, however, once again significant differences between the simulation and the experimental data are observed. The data at all LAB angles less than 45° tend to show more signal at small CM velocities, near the 'middle' of the TOF signals, than the theoretical predictions suggest. The forward/backward scattering intensities show good agreement, as do the shape of the forward scattered rising edge of the signal and the backward scattered falling edge. TOF data for the D + n-H_2 reaction at several LAB angles are shown in Figure 25. The simulations of these spectra show differences with the TOF spectra that are similar to those observed in the D + p-H_2 experiment, although the differences are larger in magnitude for the D + n-H_2 experiment at the lower collision energy.

The effect of the D-atom velocity distribution on the TOF spectra was observed to a greater extent in the nominal E_c = 0.53 eV spectra shown in Figure 12. At $\Theta_{LAB} < 32°$, two fast, forward scattered peaks were observed. The Monte Carlo simulation showed that the fastest of the two peaks is due to forward-scattered DH

formed by collisions at energies near E_c = 1.01 eV resulting from the contamination of fast D atoms present in the D-atom beam. Figure 26 shows cross-section-weighted collision energy distributions for several of the DH product states in this lower energy experiment. The reactive collisions occurring for the excited DH(v,j) products are significantly skewed to the higher collision energies which occur in the experiment, decreasing the validity of the assumption that the differences between theory and experiment can be removed by modifying the DCS only at the nominal experimental collision energy.

4.3.1 Best-Fit DCS at E_c = 0.51 eV

Iterative use of the Monte Carlo simulation program allowed the best-fit DCS for the DH(v,j) states at the lower nominal collision energy to be determined as described above. The changes in the theoretical DCS's of ZM were made at E_{tot} = 0.78 eV (E_c = 0.51 eV), which was the closest point to the nominal collision energy in the theoretical calculations (the next nearest points in ZM's calculations were at E_{tot} = 0.75 and 0.85 eV). In Figure 27, the best fits to the TOF spectra for the D + p-H_2 reaction are shown. Figure 28 shows the best fit to the LAB angular distribution. The differences between the theoretical simulation and the TOF spectra seen in Figure 12 are largely removed by the modified DCS, and the best-fit LAB angular distribution also fits the experimental data well. The remaining differences between theory and experiment are due to the strong energy dependence of the reactive cross sections for the higher j DH(v,j) products. Although these differences could be fit by more modification of the DCS and the integral cross sections for high-j DH(v,j) products at only 0.51 eV, this would not be realistic given the cross-section weighted collision energy distributions shown in Figure 26, so further efforts to fit these differences were not made. In Figure 29, the best-fit DCS curves at E_c = 0.51 eV are

plotted together with the theoretical results of ZM. The largest changes in the DCS were made for the product DH (v=0, j= 4 - 7) states in the backward hemisphere ($\theta_{cm} > 90°$). The changes made are not largest at $\theta_{cm} = 180°$, however, indicating that at this lower energy, more sideways scattering is occurring than the calculations of ZM indicate.

4.3.2 Integral Cross Sections at $E_c = 0.51$ eV

The relative DH(v,j) integral cross sections obtained by integration of the best-fit DCS obtained at $E_c = 0.51$ eV are shown in Figure 30 and listed in Table 5. Once again, the experimental result shows more rotational excitation than the theoretical predictions. For the experimental rotational distribution, $\langle j \rangle = 3.6$, while ZM's results indicated $\langle j \rangle = 3.0$. The TOF spectrum shown in Figure 31 at $\Theta_{LAB} = 32°$ illustrates the sensitivity of this data to a change in the integral cross section, using a rotational distribution with a peak shifted one quantum higher (see Figure 30 and Table 5). As the spectrum shows, the hotter rotational distribution gave a broader forward-scattered peak that was inconsistent with the data.

4.4 DH Product CM Velocity-Flux Contour Maps

Cartesian CM velocity-flux contour maps were generated from the theoretical and experimental results to graphically illustrate the general trends observed in this study. Contours of the quantity $I(u)/u^2$ plotted in CM-velocity space[42] are shown for $E_c = 0.98$ eV in Figure 32 and $E_c = 0.51$ eV in Figure 33, giving an overall picture of the observed dynamics. These maps were made using the DCS's for all the DH(v,j) states at the nominal collision energies only, so they do not show the broadening effects of the D-atom velocity distribution, or any other experimental

averaging which would be present in a single-kinematic diagram 'direct-inversion' contour map. The good qualitative agreement between experiment and the theoretical predictions is seen in the contour plots; at E_c = 0.98 eV, both theory and experiment agree that the peak of the CM-DCS is ≈ 125°, although the peak from the experimental best-fit DCS is considerably broader. The E_c = 0.51 eV results show the DCS to be strongly backward-peaked, again in agreement with the theoretical predictions. However, at both energies, the experiment shows the DCS to be more broadly distributed in both the backward and forward hemispheres. Since these plots are weighted by $1/u^2$, they exaggerate the contributions from the smaller u DH products. For example, intensity is observed within the DH(v=2) product circle in Figure 32(a), even though DH(v=2) only accounted for 0.5 % of the DH product.

5. Discussion

5.1 Comparison with other Experimental Results

The early work of Fite and coworkers[8] and Kwei and Lo[9] were 'primitive' molecular beam experiments by modern standards, characterized by broad collision energy distributions and no product velocity distribution measurements. The results of these experiments at mean collision energies of 0.48 and 0.70 eV showed that the molecular products of the reaction were strongly backward-scattered. This result is in good agreement with the present results at 0.53 eV. Goetting, Mayne and Toennies[10] performed the first experiment in which the DH-product TOF spectra were measured at several LAB angles. Deconvolution of their experimental data was hampered by an extremely broad D-atom beam velocity distribution. The data showed that the DCS for the D + H_2 reaction was peaked at a CM angle of ≈ 90° at the mean collision energy of E_c = 1.5 eV, in good agreement with QCT calculations by

Toennies and coworkers.[20] These results show more forward scattering than the present results at E_c = 1.01 eV, which is not surprising considering the higher mean collision energy.

The work of Buntin, Giese and Gentry produced vibrational state-resolved TOF spectra for the D + n-H_2 reaction similar to the present study.[13] However, TOF spectra at only single LAB angles were measured at collision energies of 0.85, 0.95 and 1.05 eV, and at two LAB angles at 1.20 eV. The experiments of Buntin, *et. al.*, used rotatable beam sources, with variable intersection angle, to change the collision energy. For this reason, the kinematics are different from the present study, so a direct comparison of the TOF spectra is not possible. Rotational distributions were extracted from the data of Buntin, *et. al.* using a Monte Carlo simulation to generate DH(v,j) final state TOF signal-shapes coupled with a least squares fitting routine which adjusted the intensity of each DH(v,j) state to achieve a best-fit to the data. The collision energy dependence of the DH(v,j) reactive cross sections was treated using the total integral cross section from QCT studies, an approximation which is no longer necessary in light of the calculations of ZM and ZTSK. This treatment was also complicated by the fact that a background subtraction of arbitrary functional form was done on the data, since no information concerning the background TOF signals in their spectra was available.[13] The rotational distributions for backward-scattered products extracted from the 0.95 eV data, in particular, are not in good agreement with ZM's predictions[3].

Two studies of the DH(v,j) product-state distribution in the D + H_2 reaction have been reported. Valentini's group[30] measured PSD's for DH(v=0,j) and DH(v=1,j) at collision energies of 0.67 and 0.79 eV using CARS spectroscopy on the DH products. These energies lie between the two nominal collision energies studied in the present experiments, and due to the strong energy dependence of the DH(v,j) cross sections it is difficult to make any direct comparisons of the experiments. The

measured PSD's showed more DH(v=0,j<4) than predicted by ZM, while the measured DH(v =1,j) distributions showed more rotational excitation than ZM's results.[3] The measured DH(v=1) cross section was observed to decrease as the collision energy was raised from 0.69 to 0.78 eV. This was interpreted as being due to a Feshbach resonance producing DH(v=1) at the lower collision energy. This behavior was not observed in the theoretical calculations.

Recent REMPI measurements in Zare's laboratory[31] on the reaction D + H_2 (v=1,j=1) → DH(v=1,j) + H has also yielded measurements for the D + H_2(v=0) → DH(v=1,j) + H PSD at a nominal collision energy of E_c = 1.05 eV. Their experimental PSD for DH(v=1,j) compares very well with both the results of ZM and ZTSK. A direct comparison of the DH(v=1,j) state distributions found by integrating the DH(v,j) DCS's in our experiment with this direct measurement of the PSD also shows excellent agreement given the uncertainties associated with the two experiments.

5.3 Implications for the H_3 Potential Energy Surface

Two points must be kept in mind regarding the significance of the comparison of the present experimental results with the theoretical predictions. First, the grid of total energies at which theoretical predictions were available was sparser at the higher energies. If the state-to-state DCS's do not vary smoothly between the calculated points, the simulation of the experimental data will be sensitive to the density of the energy grid of the theoretical predictions. As the calculations become more efficient, or faster computers become available, any questions concerning the effects of the energy-grid of the theoretical predictions will be answered. Second, in the D + p-H_2 scattering experiment, 20 to 30 percent of the H_2 reagent was in j = 2, while theoretical predictions are only available for H_2(j=0)

and H_2(j=1). The fact that the simulation of the D + n-H_2 reaction with ZTSK's H_2(j=0) and H_2(j=1) DCS predictions does not fit the experimental results much better than the D + p-H_2(j=0) predictions indicates that mere inclusion of more reactant rotor states cannot likely explain the observed discrepancies between theory and experiment.

At E_c = 0.53 eV, the experimental results indicate that DH(v=0, j = 3-7) DCS's peak farther away from direct backward scattering, as the contour maps in Figure 33 show. The implications of these results for the H_3 PES seem to suggest that partial waves with larger angular momenta contribute to the reaction at this energy. The classical picture corresponding to this result is that larger impact parameters lead to reaction, resulting in higher product rotational excitation. A 'softer' bending potential for the H_3 complex near E_{tot} = 0.78 eV could be responsible for allowing collisions of this sort to lead to reaction. Due to the collision energy dependence of the reactive cross sections, some of the differences between the predictions of ZM and the best-fit DCS at E_c = 0.51 eV should be distributed over the DCS's for higher energy collisions. The qualitative result that more sideways scattering is occurring at lower collision energies than predicted remains unaffected by these considerations, however.

At the higher collision energy, E_c = 1.01 eV, the experimental results once again show more product rotational excitation, with broadening of the DH(v=0,j) DCS's, mostly in the backward hemisphere. As the contour maps in Figure 32 show, however, a significant enhancement of the forward scattered DH was also observed. The best-fit DH(v=1,j) DCS's were seen to be more sharply backward peaked than the DH(v=0,j) states, which is not unreasonable, since typically smaller impact parameter collisions result in vibrational excitation, leading to backward scattering in the CM. Once again, the bending potential and the effect it has on D-H_2 as the reactants approach and on DH-H as the products recoil is likely to be responsible for

the differences observed between the theoretical and experimental DCS's for rotationally excited DH. In this case, the influence of the bending potential may be different in the entrance and exit channels. A softer bending potential at low interaction energies could allow collisions with larger orbital angular momenta to lead to the transition state for the reaction, while a change in the curvature of the bending potential which becomes stiffer at higher energies, could limit the extent to which D-H-H may bend, resulting in more backward scattering as well as higher product rotational excitation. The observation of more DH(v=2) product in the experiment may also be due to a minor deficiency in the PES. Changing the PES from LSTH to DMBE does not resolve this discrepancy, however, as the results of ZM and ZTSK show.[3,4] These experimental results show that further studies of the H_3 PES, especially in the region of bent configurations at higher energies, are warranted due to the discrepancies between the predicted and measured DCS's.

While extensive theoretical studies of the effect of the bending potential on state-to-state DCS's have yet to be done, some information on the effect on product-state distributions is available. Blais, Truhlar and Garrett[46] examined the H + D_2 product-state distributions produced by QCT calculations on both the LSTH PES[1] and a modified PES which was identical to the LSTH surface for collinear geometries, with a softer bending potential. More rotational excitation was observed on the modified surface, but the mean DH product CM scattering angle did not change significantly. More recently, a 3-D quantum scattering study of the PES sensitivity of the PSD's for the H + H_2 reaction has been performed.[47] This work compared the energy dependence of the H_2(v=1,j=1,3) cross sections obtained on the LSTH and DMBE *ab initio* surfaces. These surfaces differ somewhat at the collinear saddle point, with more significant differences for bent geometries, with the DMBE surface having the softer bending potential. The energy dependence of the reactive cross sections was not observed to change significantly, but the calculated cross

sections were somewhat higher on the DMBE surface, due to the lower barrier height. For the D + H_2 reaction, the differences between the DCS predictions of ZM and ZTSK show the small effect that changing PES's from the LSTH to DMBE surfaces has on the DCS's. ZTSK's results show clearly that more significant differences result from including reactant H_2(j=1) in the calculations than changing the PES between these two nearly identical surfaces.[4] These two surfaces are based on almost the same 'chemically accurate' data points, with collinear H_3 configurations near the reaction threshold given greater weight in the fitting procedure than higher energy, non-collinear configurations, since the ab initio calculations were of higher quality for the collinear configurations.[3,4] The differences observed between theory and this experiment at the level of state-to-state differential cross sections shows that perhaps regions of H_3 configuration space that play an important role in the detailed dynamics of the hydrogen exchange reaction remain to be probed in greater detail.

6. Conclusions

The results presented in this paper constitute the most complete high-resolution DCS measurements to date for the fundamental elementary reaction D + $H_2 \rightarrow$ DH + H. This work also marks the first direct comparison of extensive DCS measurements with fully converged 3-D quantum scattering calculations performed on the accurate *ab initio* LSTH and DMBE PES's, the best known for any chemical reaction. The LAB data show a level of overall agreement with the theoretical predictions of ZM and ZTSK that indicates that the theoretical understanding of this reaction and the PES which governs it is good over the entire experimentally accessible energy range. At the level of DH(v,j) integral cross sections the differences between the theoretical predictions and the experimental results are minor. The

more sensitive comparison of DCS's, however, shows significant differences between the theoretical and best-fit DCS's for rotationally excited DH(v,j) product states at both collision energies, indicating that the high-energy bending potential of the PES may need to be reexamined in greater detail. Future theoretical studies of the sensitivity of the DH(v,j) DCS's to the PES and the calculation of new *ab initio* PES's with emphasis on the quality of the H_3 bending potential should answer some of the questions raised by these differential cross section measurements.

Further improvements of both the sensitivity and resolution of these experiments, which used non-state-selective mass spectrometric detection of reaction products, will be a difficult proposition. The next generation of DCS measurements for this elementary reaction will require rotational-state resolution to make a more critical comparison at the level of angular distributions of each vibrational-rotational state with the accurate chemical dynamics calculations which are now available. Sensitive laser-based, state-selective detection techniques hold the most promise for the advances required to achieve this goal. The high-resolution H-atom TOF technique demonstrated by Welge and coworkers has already shown rotational state resolution for high product rotational states in the H + D_2 reaction.[48]

This experiment has provided one of the most critical experimental tests of the H_3 PES to date, and has found that for some regions of this surface further *ab initio* investigations of the H_3 potential energy appear to be necessary. Of course, without the recent advances in quantum scattering calculations, the interpretation of these results would have been considerably more difficult. With the timely confluence of theoretical predictive power and detailed dynamics experiments that is now occurring, we can look forward to a completely quantitative knowledge of how chemical reactions occur, not only for the simplest reaction, but also for heavier and more complex systems.

Acknowledgments

We are indebted to Dr. John Zhang and Prof. William Miller for their close collaboration in the calculation of the differential cross sections for the D + H_2 reaction for comparison with these experimental results, and many discussions concerning our respective results. Profs. Donald Truhlar and Donald Kouri were very helpful in sending a tape of their DCS predictions prior to publication. Drs. Bob Walker and Russ Pack provided the basic Monte Carlo simulation code which was adapted to the simulation of this experiment, and we thank them for all of their help. Dr. Gary Robinson participated in early, unsuccessful attempts at studying this reaction. AT&T Bell Laboratories is also acknowledged for providing a Lambda Physik EMG 103 MSC excimer laser for use in the early experiments. This work was supported by the Director, Office of Basic Energy Sciences, Chemical Sciences Division of the U.S. Department of Energy under contract No. DE-AC03-76SF00098.

[1] B. Liu, J. Chem. Phys., **58**, 1925 (1973); P. Siegbahn and B. Liu, J. Chem. Phys., **68**, 2457 (1978); D.G. Truhlar and C.J. Horowitz, J. Chem. Phys., **68**, 2466 (1978); *ibid.*, **71**, 1514E (1979).

[2] A.J.C. Varandas, F.B. Brown, C.A. Mead, D.G. Truhlar and N.C. Blais, J. Chem. Phys., **86**, 6258 (1987).

[3] J.Z.H. Zhang and W.H. Miller, J. Chem. Phys., **91**, 1528 (1989).

[4] M. Zhao, D.G. Truhlar, D.W. Schwenke, and D.J. Kouri, J. Phys. Chem., submitted.

[5] T. Dreier and J. Wolfrum, Int. J. Chem. Kin., **18**, 919 (1986).

[6] E.E. Marinero, C.T. Rettner and R.N. Zare, J. Chem. Phys., **80**, 4146 (1984).

[7] D.P. Gerrity and J.J. Valentini, J. Chem. Phys., **81**, 1290 (1984).

[8] J. Geddes, H.F. Krause, and W.L. Fite, J. Chem. Phys., **42**, 3296 (1972); *ibid.*, **56**, 3298 (1972); *ibid.*, **59**, 566E (1972).

[9] G.H. Kwei, V.W.S. Lo, and E.A. Entemann, J. Chem. Phys., **59**, 3421 (1973); G.H. Kwei and V.W.S. Lo, J. Chem. Phys., **72**, 6265 (1980).

[10] R. Goetting, H.R. Mayne and J.P. Toennies, J. Chem. Phys., **80**, 2230 (1984); *ibid.* **85**, 6396 (1986).

[11] R. Goetting, J.P. Toennies and M. Vodegel, Int. J. Chem. Kin., **18**, 949 (1986); R. Goetting, V. Herrero, J.P. Toennies and M. Vodegel, Chem. Phys. Lett., **137**, 524 (1987).

[12] For a review of recent experimental and theoretical work on the hydrogen exchange reaction see J.J. Valentini and D.L. Phillips, in Advances in Gas Phase Photochemistry and Kinetics, Vol. 2: Bimolecular Collisions, M.N.R. Ashfold and J.E. Baggot, Eds., Royal Society of Chemistry, London, 1989, p. 1.

[13] S.A. Buntin, C.F. Giese, and W.R. Gentry, J. Chem. Phys., **87**, 1443 (1987); S.A. Buntin, Ph.D. Thesis, University of Minnesota, (1987).

[14]R.E. Continetti, B.A. Balko and Y.T. Lee, paper presented at the International Symposium on Near-Future Chemistry in Nuclear Energy Field, Ibarako-Ken, Japan, Feb. 15-16, 1989, to be published in proceedings (UC-LBL report LBL-26762).

[15]F. London, Z. Elektrochem., **35**, 552 (1929).

[16]H. Eyring and M. Polanyi, Z. Physik. Chem. **B12**, 279, (1931).

[17]D.G. Truhlar and R.E. Wyatt, Adv. Chem. Phys., **36**, 141 (1977).

[18]B. Liu, J. Chem. Phys., **80**, 581 (1984).

[19]D.M. Ceperley and B.J. Alder, J. Chem. Phys., **81**, 5833 (1984). ; R.N. Barnett, P.J. Reynolds and W.A. Lester, Jr., J. Chem. Phys., **82**, 2700 (1985).

[20]H.R. Mayne, J. Chem. Phys., **73**, 217 (1980) ; G.D. Barg, H.R. Mayne and J.P. Toennies, J. Chem. Phys., **74**, 1017 (1981) ; H.R. Mayne and J.P. Toennies, J. Chem. Phys., **75**, 1794 (1981); N. Sathyamurthy and J.P. Toennies, Chem. Phys. Lett., **143**, 323 (1988).

[21]N.C. Blais and D.G. Truhlar, J. Chem. Phys., **88**, 5457 (1988).

[22]F.J. Aoiz, V.J. Herrero and V. Saez, Chem. Phys. Lett., **161**, 270 (1989).

[23]P. Brumer and M. Karplus, J. Chem. Phys., **54**, 4955 (1971).

[24]K.T. Tang and B.H. Choi, J. Chem. Phys., **62**, 3642 (1975); N. Abu Salbi, D.J. Kouri, Y. Shima and M. Baer, J. Chem. Phys., **82**, 2650 (1985); B.M.D.D. Jansen op de Haar and G.G. Balint-Kurti, J. Chem. Phys., **90**, 888 (1989).

[25]G.C. Schatz and A. Kuppermann, J. Chem. Phys., **65**, 4642 (1975); *ibid.*, **65**, 4668 (1975).

[26]J.Z.H. Zhang and W.H. Miller, Chem. Phys. Lett., **153**, 465 (1988).

[27]D.E. Manolopoulos and R.E. Wyatt, Chem. Phys. Lett., **159**, 123 (1989).

[28]a)S. Datz and E.H. Taylor, J. Chem. Phys., **39**, 1896 (1963).

b) W.L. Fite and R.T. Brackmann, in Atomic Collision Processes, ed. by M.R.C. McDowell, North Holland, Amsterdam (1964), pp. 955-963.

[29]D.L. Phillips, H.B. Levene and J.J. Valentini, J. Chem. Phys., **90**, 1600 (1988).

[30]D.A.V. Kliner and R.N. Zare, J. Chem. Phys., **92**, 2107 (1990); D.A.V. Kliner , K.-D. Rinnen and R.N. Zare, Chem. Phys. Lett, In Press.

[31]J.-C. Nieh and J.J. Valentini, Phys. Rev. Lett., **60**, 519 (1988); J.-C. Nieh and J.J. Valentini, J. Chem. Phys., **92**, 1083 (1990).

32 Y.T. Lee, J.D. McDonald, P.R. LeBreton and D.R. Herschbach, Rev. Sci. Inst., **40**, 1402 (1968).

[33]R.E. Continetti, Ph.D. Thesis, Univ. of Calif., Berkeley, (1989).

[34] a). N.F. Daly, Rev. Sci. Inst., **31**, 264 (1960).

b). H.M. Gibbs and E.D. Commins, Rev. Sci. Inst., **37**, 1385 (1966).

[35]D. Proch and T. Trickl, Rev. Sci. Inst., **60**, 713 (1989).

[36]G.N.A. Van Veen, K.A. Mohamed, T. Baller and A.E. DeVries, Chem. Phys., **80**, 113 (1983).

[37]J.H. Ling and K.R. Wilson, J. Chem. Phys., **65**, 881 (1976).

[38]J.E. Pollard, D.J. Trevor, Y.T. Lee and D.A. Shirley, J. Chem. Phys., **77**, 4818 (1982).

39 P.M. Aker, G. Germann and J.J. Valentini, J. Chem. Phys., **90**, 4795 (1989).

40 D.A.V. Kliner, K.-D. Rinnen and R.N. Zare, J. Chem. Phys., **90**, 4625 (1989).

41 R. Wolfgang and R.J. Cross, Jr., J. Phys. Chem., **73**, 743 (1969).

42 E.A. Entemann, Ph.D. Thesis, Harvard University (1967).

43 R. T. Pack, J. Chem. Phys., **81**, 1841 (1984).

44 The Monte Carlo program is an enhanced version of a code originally obtained from Dr. R.B. Walker, Los Alamos National Lab. See reference 33.

[45]Eight Peak Index of Mass Spectra, Mass Spectrometry Data Centre, Royal Society of Chemistry, Nottingham, UK, Vol. 1, pt. 1, p. 1 (1983).

46 N.C. Blais, D.G. Truhlar and B.C. Garrett, J. Chem. Phys., **82**, 2300 (1985).

[47]S.M. Auerbach, J.Z.H. Zhang and W.H. Miller, Trans. Farad. Soc., In Press.

[48]K.A. Welge, XII International Symposium on Molecular Beams, Abstracts of Invited Talks and Contributed Papers (May29-June 2, 1989, Perugia, Italy),p. I.10.

Table 1: Beam Velocity and Collision Energy Parameters

V_D[a] (cm/s)	ΔV_D[b]	V_{H2}[c] (cm/s)	$\Delta V/V$	E_c[d] (eV)	ΔE_c
1.38×10^6	$+0.01 \times 10^6$ -0.04×10^6	2.82×10^5	0.11	1.01	+ 0.04 - 0.06
9.77×10^5	$+0.08 \times 10^5$ -0.20×10^5	2.82×10^5	0.11	0.53	+0.024 -0.048

a; These are the LAB velocities corresponding to the peak in the D-atom beam number density distribution. Note that these velocities are ≈ 1.5% higher than expected in the single-collision photodissociation of DI at 248 nm due to preferential attenuation of slower D atoms and other collisional effects in the beam source.

b; FWHM spread of the D-atom beam about the peak velocity.

c; Peak p-H_2 beam velocity at a stagnation pressure of 1200 torr measured with a single-shot TOF chopper wheel. The n-H_2 beam velocity distribution was characterized by a peak of 2.77×10^5 cm/sec, with $\Delta V/V = 0.12$. This resulted in a negligible difference in collision energy in the two experiments (<< 1%).

d; Nominal collision energies for the experiments, with uncertainties ΔE given as the FWHM about the peak collision energy. See Figures 19 and 26 for a more complete picture of the collision energy distribution in these experiments.

Table 2: Relative DH(v=0,j) Total Cross Sections at E_{tot} = 1.25 eV

DH(v,j)	Best Fit	ZM	Cold	Hot
0,0	0.05	0.06	0.07	0.05
0,1	0.13	0.18	0.17	0.12
0,2	0.24	0.34	0.32	0.24
0,3	0.33	0.43	0.47	0.31
0,4	0.48	0.55	0.66	0.42
0,5	0.68	0.74	0.85	0.57
0,6	0.88	0.91	1.00	0.82
0,7	1.00	1.00	0.96	0.99
0,8	0.84	0.95	0.78	1.00
0,9	0.69	0.74	0.56	0.94
0,10	0.51	0.40	0.40	0.76
0,11	0.32	0.14	0.22	0.45
0,12	0.05	0.03	0.04	0.07
<j>	6.7	6.3	6.2	7.1

Table 2. Relative DH(v=0,j) integral cross sections in arbitrary units for the D + H_2 reaction at a total energy of 1.25 eV, (E_c = 0.98 eV). The theoretical predictions at this energy were modified to fit the experimental results at a nominal E_c = 1.01 eV. The best-fit integral cross sections are given in the first column, with the theoretical integral cross sections of ZM given in the second column. Two arbitrary rotational distributions used in the sensitivity tests of the data are shown as 'Cold' and 'Hot'.

Table 3; Relative DH(v=1,j) Total Cross Sections at E_{tot} = 1.25 eV

DH(v,j)	Best Fit	ZM	Cold	Hot
1,0	0.24	0.21	0.46	0.16
1,1	0.60	0.59	0.76	0.42
1,2	0.85	0.84	1.00	0.60
1,3	1.00	1.00	0.87	0.77
1,4	0.97	0.87	0.64	1.00
1,5	0.65	0.61	0.48	0.85
1,6	0.37	0.34	0.29	0.51
1,7	0.21	0.14	0.17	0.30
1,8	0.12	0.03	0.01	0.20
1,9	<0.01	<0.01	<0.01	<0.01
1,10	<0.01	<0.01	<0.01	<0.01
<j>	3.4	3.2	2.9	3.9

Table 3. Integral cross sections for DH(v=1,j) at E_{tot} = 1.25 eV; see Table 2 caption.

Table 4. Relative DH(v) Total Cross Sections at E_{tot} =1.25 eV

DH(v)	Best Fit	ZM
0	1.0	1.0
1	0.11	0.13
2	.005	0.002

Table 4. Relative DH(v) cross sections at E_{tot} = 1.25 eV compared with the results of ZM.

Table 5. Relative DH(v=0,j) Total Cross Sections at E_{tot} = 0.78 eV

DH(v,j)	Best Fit	ZM	Hot
0,0	0.26	0.26	0.14
0,1	0.67	0.71	0.44
0,2	0.94	0.96	0.49
0,3	0.94	1.00	0.70
0,4	1.00	0.79	0.89
0,5	0.78	0.51	1.00
0,6	0.71	0.24	0.95
0,7	0.37	0.09	0.66
0,8	<0.01	0.02	0.19
0,9	<0.01	<0.01	<0.01
<j>	3.6	3.0	4.4

Table 5. Integral cross sections for DH(v=0,j) at E_{tot} = 0.78 eV, (E_c = 0.51 eV) used to fit the low collision energy data at a nominal E_c = 0.53 eV. The arbitrary rotational distribution marked 'Hot' was used in the sensitivity tests of the data.

Figure Captions

Figure 1. Energetics of the collinear D + $H_2 \rightarrow$ DH + H reaction, showing the collision energies studied in this experiment and the accessible DH vibrational states. The abscissa shows the total energy for the system ($E_{tot} = E_c + E_{ZPE}$).

Figure 2. Schematic view of the experimental geometry. The output of an excimer laser , 1, was polarized with a transmission polarizer, 2. The laser beam then entered the molecular beam machine, crossing a pulsed beam of DI, 3. The DI/laser interaction occurred in a differential pumping chamber, with cryo-panels, 4, assisting in the evacuation. The recoiling D atoms were collimated, forming the D-atom beam, 6, which crossed the H_2 molecular beam, 8, produced in a separate differential pumping chamber by the pulsed valve, 7. DH products, 10, scattered into the mass-spectrometric detector, and were ionized in the electron-impact ionizer, 9.

Figure 3. Schematic diagram of the data acquisition scheme. The chopper wheel was synchronously spun. A photodiode mounted on the chopper assembly produced a clock pulse upon which the rest of the experimental timing was based. This pulse was sent to DDL 1, a digital delay generator which then triggered the DI pulsed beam. After a suitable delay the H_2 beam was triggered by DDL 2. The laser was triggered last, by DDL 3. The DI/H_2/laser delays had to be set to ensure that DI, H_2 and the opening on the chopper wheel were all synchronized to allow the D atoms to fly from the photolysis source, react with H_2, and the reactively scattered DH product to enter the detector before

the chopper closed. A synchronization pulse from the laser triggered the multichannel scaler, MCS, for acquisition of the TOF data.

Figure 4. (a) D-atom TOF with the solid curve fit generated by Monte Carlo simulation program. The **E** vector of the excimer-laser light was parallel to the direction of detection, giving the nominal collision energy of 0.53 eV, (upper frame).

(b) D-atom TOF with **E** perpendicular to the direction of detection, giving the nominal collision energy of 1.01 eV, (lower frame).

Figure 5. Typical raw TOF spectra (m/e = 3) for the E_c = 1.01 eV (first column) and 0.53 eV (second column) D + H_2 reaction. The LAB angles are marked on the spectra. The curves fit to the data represent the modulated background contributions to the signal: —— ; total modulated background: ····· ; D-atom-beam modulated background: - - - - - - ; H_2-beam modulated background.

Figure 6 (a). Representative TOF spectrum showing the polynomial fit to the m/e = 3 DH background produced by a p-H_2 beam at a LAB angle of 27.5°.

(b). Representative TOF spectrum at a LAB angle of 17° showing the fit to the m/e = 3 background produced by DH in the D-atom beam without a crossed beam on. The polynomial fit is shown as the solid line. The scaling between these two figures is arbitrary.

Figure 7. Raw TOF spectra (m/e = 3) for the reaction D + n-H_2 → DH + H at E_c = 1.01 eV (open circles) compared with the reaction D + p-H_2 → DH + H at a LAB angle 27.5° (solid curve). The reactive scattering signal was not

measurably different, but a significant difference was observed in the large peak at long times-of-flight which was produced by the H_2 beam alone.

Figure 8. TOF spectra at m/e = 3, measured for D + p-H_2 → DH + H reactive scattering at E_c = 1.01 eV (solid curve) and DH + He → DH + He (solid points). The dashed curve fit to the DH + He TOF spectrum was generated using the DH signal measured with only the D-atom beam running.

Figure 9. Kinematic diagram for the D + H_2 → DH + H reaction at E_c = 0.98 eV, showing the relationship between the CM and LAB reference frames. The concentric circles centered at the origin of the CM frame represents the maximum CM recoil velocities for DH products in v = 0 , 1 and 2. The CM recoil velocities for DH(v=0,j=10 and 11) products are also shown. This kinematic diagram was used for the comparison of the nominal E_c = 1.01 eV data with the theoretical predictions of ZM and ZTSK at E_c = 0.98 eV.

Figure 10. Corrected TOF spectra at m/e = 3 for the D + p-H_2 → DH + H reaction at E_c = 1.01 eV. The LAB scattering angles are indicated on the spectra. The solid line fit to the spectra shows the results of the Monte Carlo simulation of the data with the theoretical results of ZM. The contributions from DH(v=0) are shown as ····· ; DH(v=1) - - - - - . At LAB angles from 20° to 25°, a small contribution from DH(v=2), which appears as a solid curve, is seen near 65 μsec. At LAB angles from 20° to 40°, the simulation shows less signal in the 50 to 80 μsec range than the data.

Figure 11. Kinematic diagram for the D + H_2 → DH + H reaction at E_c = 0.51 eV, used for comparison of the theoretical predictions of ZM with the nominal E_c

= 0.53 eV data. CM product recoil velocities for DH(v=0,j=0), DH(v=1,j=0) and DH(v=0, j=6 and 7) are shown.

Figure 12. Corrected TOF spectra at m/e = 3 for the D + p-H_2 → DH + H reaction at E_c = 0.53 eV. See Figure 10 caption for definition of the curves fit to the data. Significant differences between the simulation and the LAB data are seen for LAB angles from 23° to 47.5° in the 60 to 110 μsec flight-time range.

Figure 13. LAB angular distribution at E_c = 1.01 eV generated by integrating the corrected TOF's. The solid line shows the results of the Monte Carlo simulation of the experiment using the theoretical predictions summed over vibrational states. The contributions from the DH vibrational states are shown as; DH(v=0) - - - - -; DH(v=1) - - - -; DH(v=2) – – – –.

Figure 14. LAB angular distribution at E_c = 0.53 eV generated by integrating the corrected TOF's. The contributions from the DH vibrational states are shown as; DH(v=0) - - - - -; DH(v=1) - - - - -.

Figure 15. Schematic flowchart of the Monte Carlo CM→LAB transformation simulation program. In the Monte Carlo iteration cycle any finite apparatus viewing volume effects are explicitly checked by noting if the chosen trajectories can pass through the appropriate source or detector defining apertures. The calculation is done for a given D + H_2(v,j) → DH(v,j) + H reaction, then either repeated, with results summed over j to give the DH(v) results, or output for examination of specific DH(v,j) final state TOF and LAB angular distribution results.

Figure 16. DCS surfaces in CM-angle total energy space for selected DH(v,j) product states generated by a 2-D spline fit of the predictions of ZM at 15 total energies from 0.4 to 1.35 eV for the D + H_2(0,0) reaction (CM DCS in units of $2\pi a_0^{2)}$.

Figure 17. Monte Carlo simulation of H + He → $\underline{H}$ + He (m/e = 1) at LAB angles of 10° and 15°. The open points represent the LAB TOF data and the solid curve shows the results of the simulation. At 10°, some underlying broad signal due to H_2 impurity in the H-atom beam is seen.

Figure 18. Corrected TOF spectra for the E_c = 1.01 eV D + n-H_2 reaction at several LAB angles. This simulation was done using the H_2(j=0 and 1) results of ZTSK. The curves fit to the data have same meaning as in Figure 10.

Figure 19. Collision energy distribution generated by the Monte Carlo program. (a) unweighted $P(E_c)$, with the D-atom velocity distribution corresponding to E_c = 1.01 eV. (b) $P(E_c)$ weighted by $\sigma(E_c)$ for DH (v=0, j=0) product. (c) $P(E_c)$ weighted by $\sigma(E_c)$ for DH(v=0,j=7) product. (d) $P(E_c)$ weighted by $\sigma(E_c)$ for DH(v=1,j=0) product. (e) $P(E_c)$ weighted by $\sigma(E_c)$ for DH(v=1,j=5) product. (f) $P(E_c)$ weighted by $\sigma(E_c)$ for DH(v=2,j=0) product.

Figure 20. Best fit to the TOF spectra for D + p-H_2 at E_c = 1.01 eV. Curves fit to the data have same meaning as in Figure 10.

Figure 21. Best fit to the LAB angular distribution for D + p-H_2 at E_c = 1.01 eV shown as the solid curve fit to the data. The - - - - - curve shows the fit

with the 'Cold' rotational distribution, (see Table 3-1). The - - - - curve shows the fit with the 'Hot' rotational distribution.

Figure 22. Best-fit CM DCS's at E_{tot} = 1.25 eV. The solid curves show the predictions of ZM, while the dashed curves show the DCS which gave the best fit to the experimental data. The set of curves for DH(v=0) and DH(v=1) are normalized separately.

Figure 23. Best-fit DH(v,j) integral cross sections at E_c = 0.98 eV, compared with the results of ZM. The normalization of the curves is arbitrary. The upper frame shows the DH(v=0,j) cross sections and the lower frame shows the DH(v=1,j) cross sections. Solid curve with open circles are the results of ZM. The dashed line with squares are the best fit results. The – – – – curve represents the 'Hot' distribution; the - - - - - curve represents the 'Cold' rotational distribution.

Figure 24. TOF spectra at Θ_{LAB} = 27.5° and 32° for E_c = 1.01 eV. The simulation using the best fit DCS is shown as the solid line; the simulation with the 'Cold' distribution is given by the - - - - curve , the simulation with the 'Hot' distribution is given by the – · – · – curve.

Figure 25. Corrected TOF spectra for the E_c = 0.53 eV D + n-H_2 reaction at several LAB angles. Curves fit to the data using the H_2(j=0) results of ZM have the same meaning as in Figure 10. Simulations using the H_2(j=0 and 1) results of ZTSK did not significantly improve the fit to the data.

Figure 26. Collision energy distribution generated by the Monte Carlo program. (a) unweighted $P(E_c)$, with the D-atom velocity distribution corresponding to $E_c = 0.53$ eV. (b) $P(E_c)$ weighted by $\sigma(E_c)$ for DH (v=0, j=0) product. (c) $P(E_c)$ weighted by $\sigma(E_c)$ for DH(v=0,j=7) product. (d) $P(E_c)$ weighted by $\sigma(E_c)$ for DH(v=1,j=0) product.

Figure 27. Best fit to the TOF spectra for D + p-H_2 at $E_c = 0.53$ eV. Curves fit to the data have same meaning as in Figure 10.

Figure 28. Best fit to the LAB angular distribution for D + p-H_2 at $E_c = 0.53$ eV. The solid line shows the best-fit DCS simulation, while the dashed line shows the simulation with the 'Hot' rotational distribution.

Figure 29. Best-fit CM differential cross sections at $E_{tot} = 0.78$ eV. The solid curves show the predictions of ZM, while the dashed curves show the best-fit to the experimental data.

Figure 30. Best-fit DH(v=0,j) integral cross sections at $E_c = 0.51$ eV, compared with the results of ZM. The solid curve with open circles represents the results of ZM, the dashed curve with squares is the best-fit DCS, and the – – – – curve is the 'Hot' rotational distribution.

Figure 31. TOF spectrum at $\Theta_{LAB} = 32°$ for $E_c = 0.53$ eV, showing results of the simulation using the best-fit DCS, shown as the solid line, the results of ZM are given by the - - - - curve , and the 'Hot' distribution is given by the – · – · – curve.

Figure 3-32 (a). Cartesian CM velocity-flux contour map using the best-fit DCS at E_c = 0.98 eV. The incident D atom and H_2 molecule velocity vectors in the CM are shown, as well as the possible CM recoil velocities for DH(v=0,1 and 2). Significantly increased backward scattering of internally excited DH product is shown, as well as more forward scattering, mostly in DH(v=0), when compared with the theoretical results in (b).

(b). Cartesian CM velocity-flux contour map using the theoretical DCS of ZM.

Figure 3-33 (a). Cartesian CM velocity-flux contour map using the best-fit DCS at E_c = 0.51 eV. More rotationally excited DH is observed in the backward hemisphere compared to the theoretical DCS in (b).

(b). Cartesian CM velocity-flux contour map using the theoretical DCS of ZM.

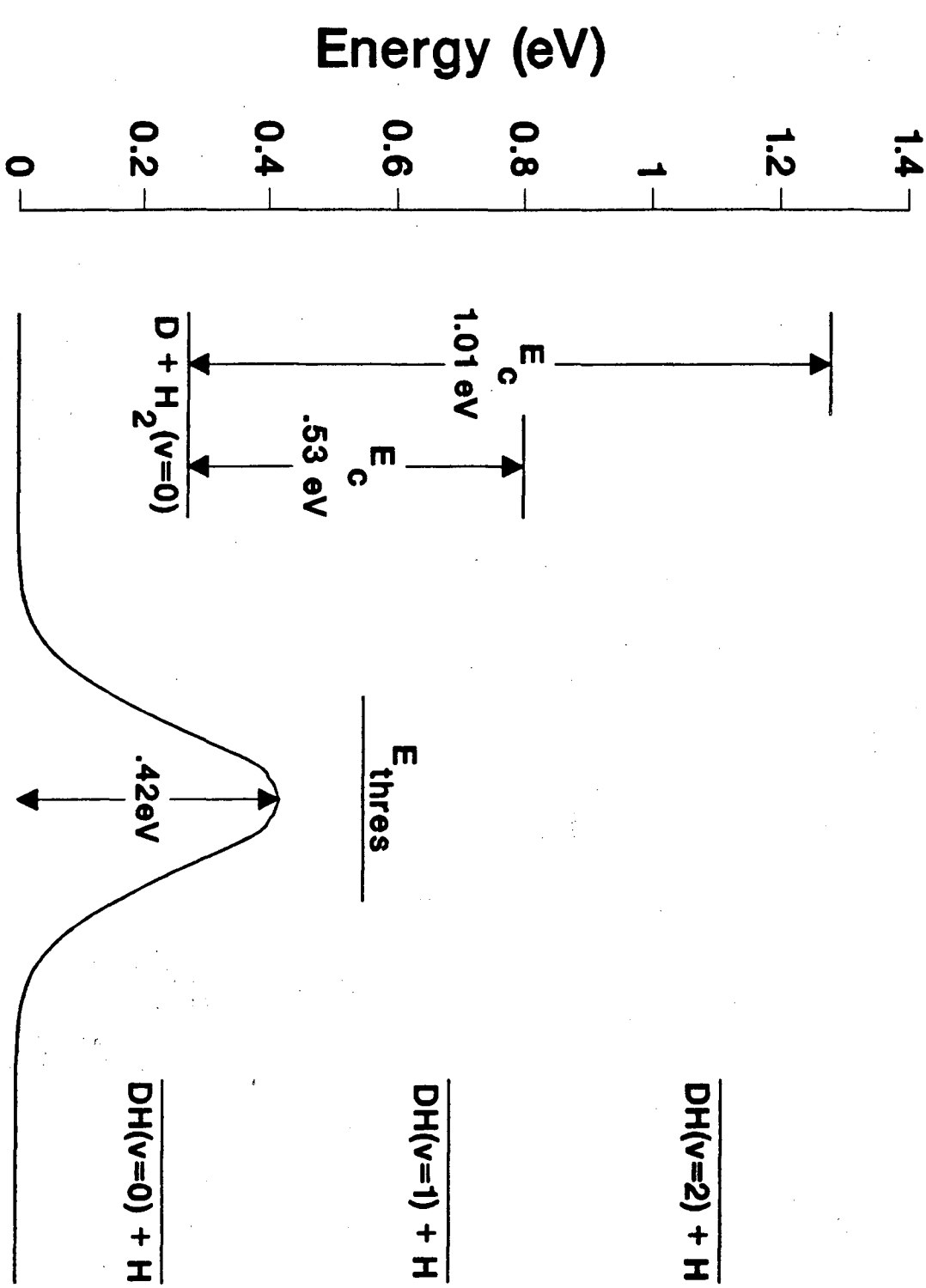
Energy (eV)
0
0.2
0.4
0.6
0.8
1
1.2
1.4
D + H2 (v=0)
1.01 eV
Ec
.53 eV
Ec
Ethres
.42eV
DH(v=0) + H
DH(v=1) + H
DH(v=2) + H

Figure 1

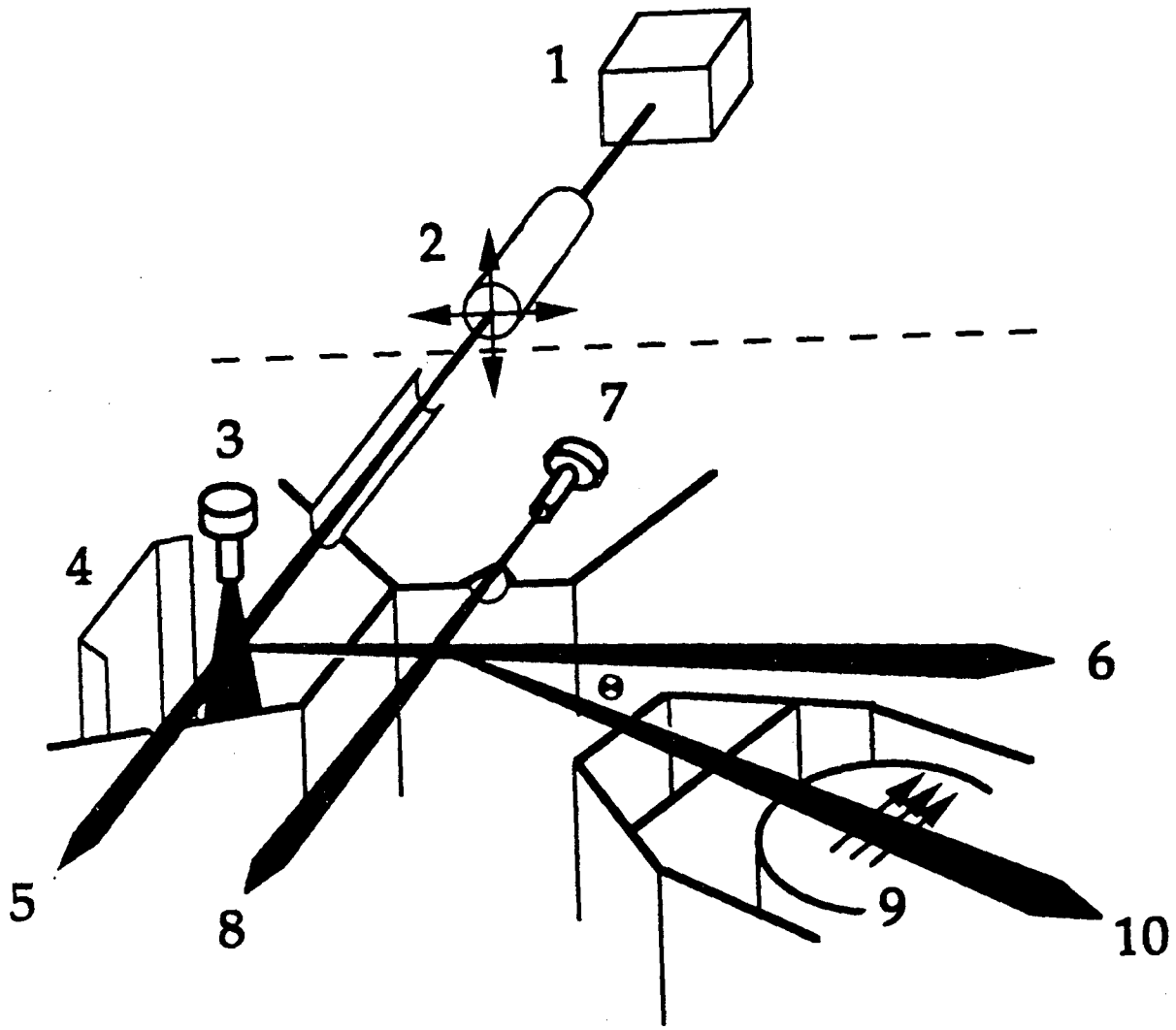

XBL 8911-4202

Figure 2

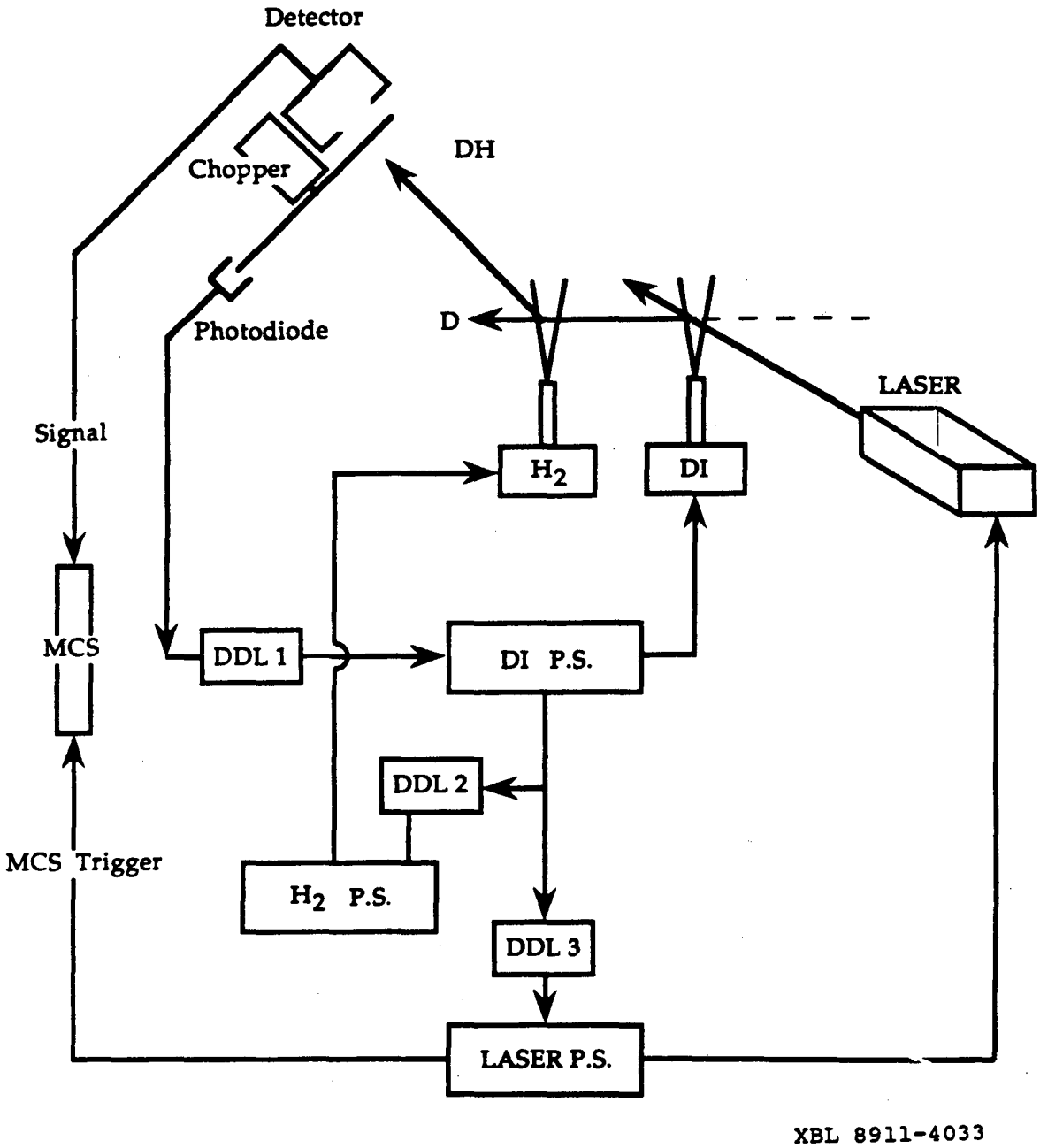
Detector
Chopper
DH
Photodiode
D
LASER
Signal
H_2
DI
MCS
DDL 1
DI P.S.
DDL 2
MCS Trigger
H_2 P.S.
DDL 3
LASER P.S.
XBL 8911-4033

Figure 3

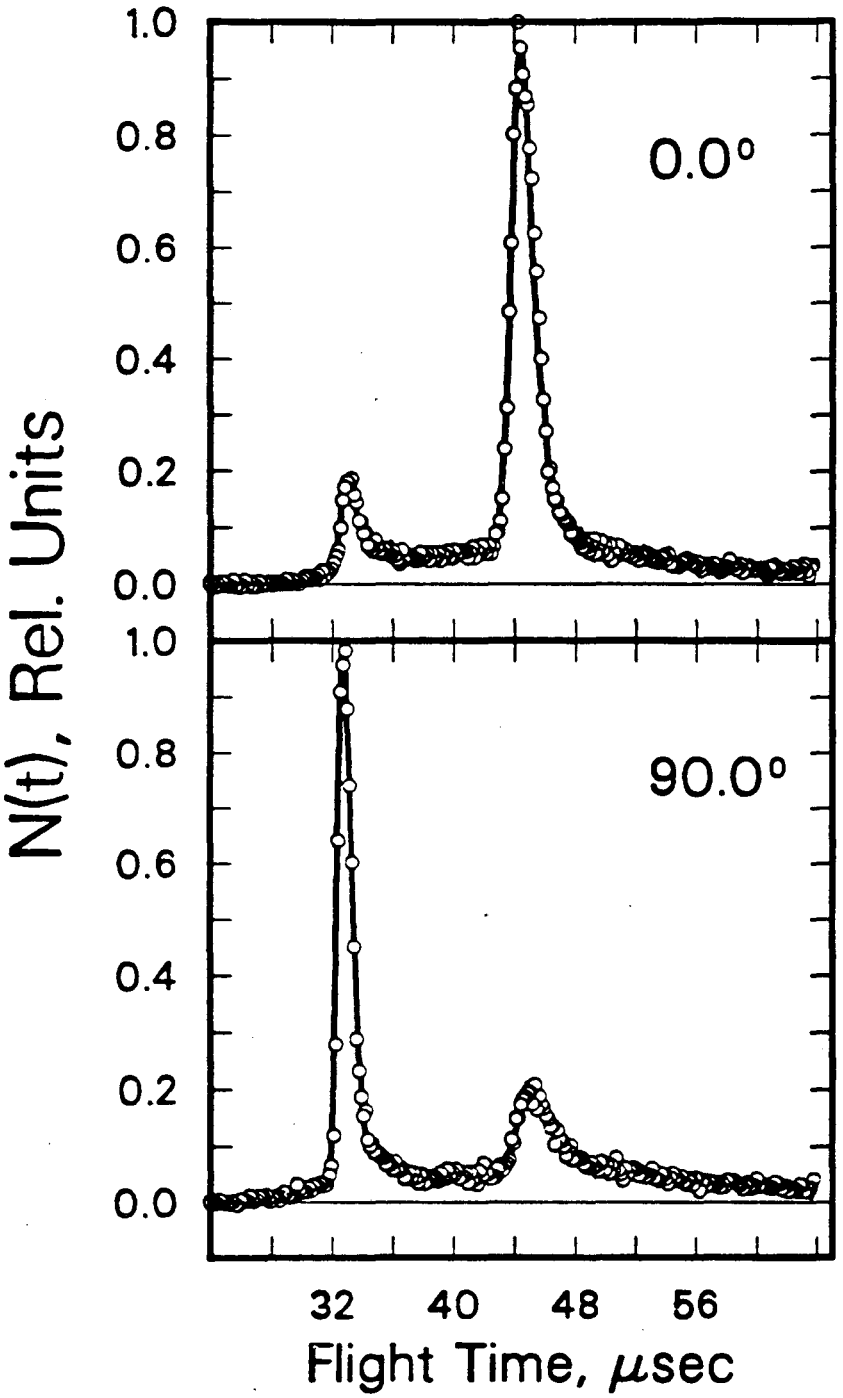
1.0
0.8
0.6
0.4
0.2
0.0
0.0°
90.0°
N(t), Rel. Units
32
40
48
56
Flight Time, μsec
XBL 904-1397

Figure 4

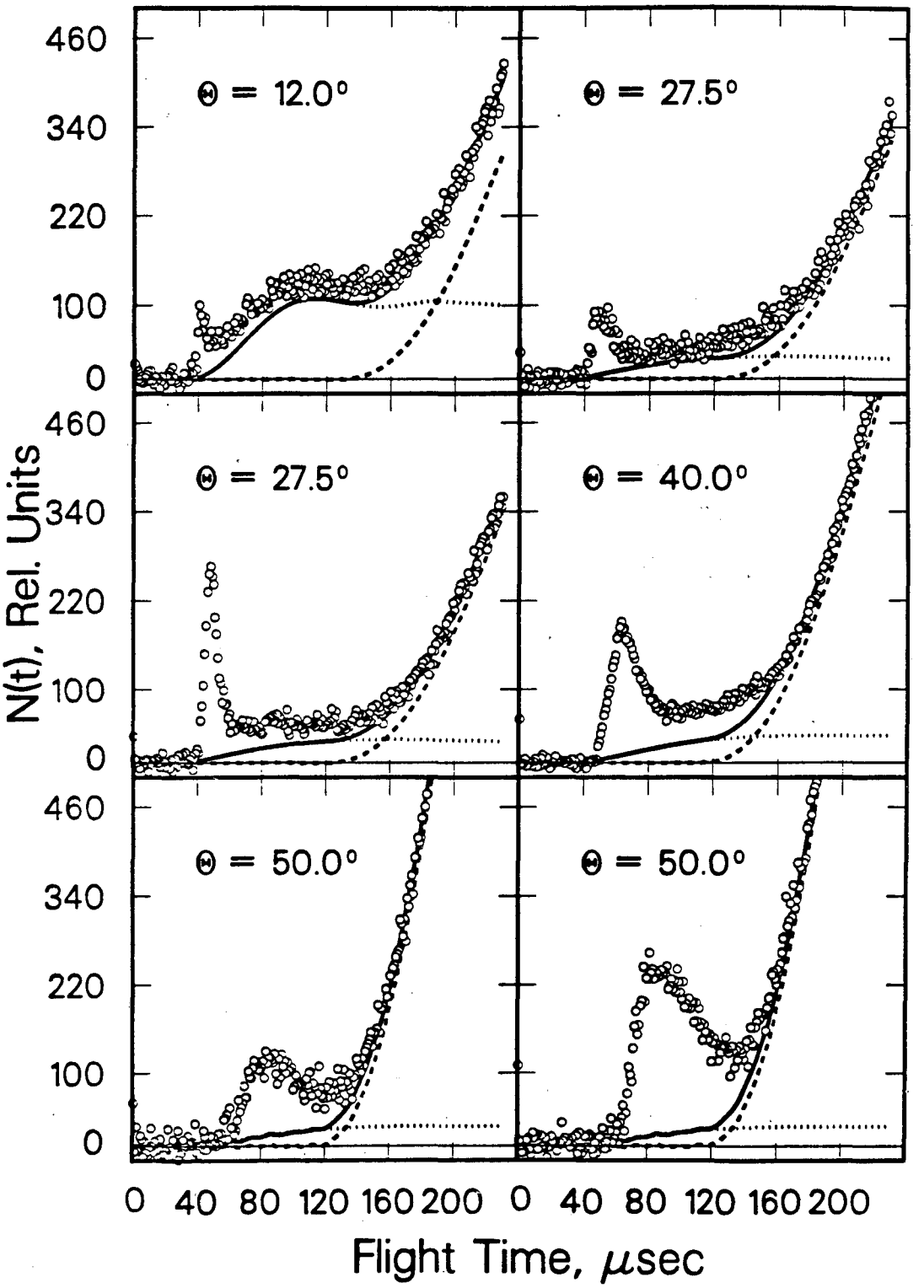

XBL 904-1372

Figure 5

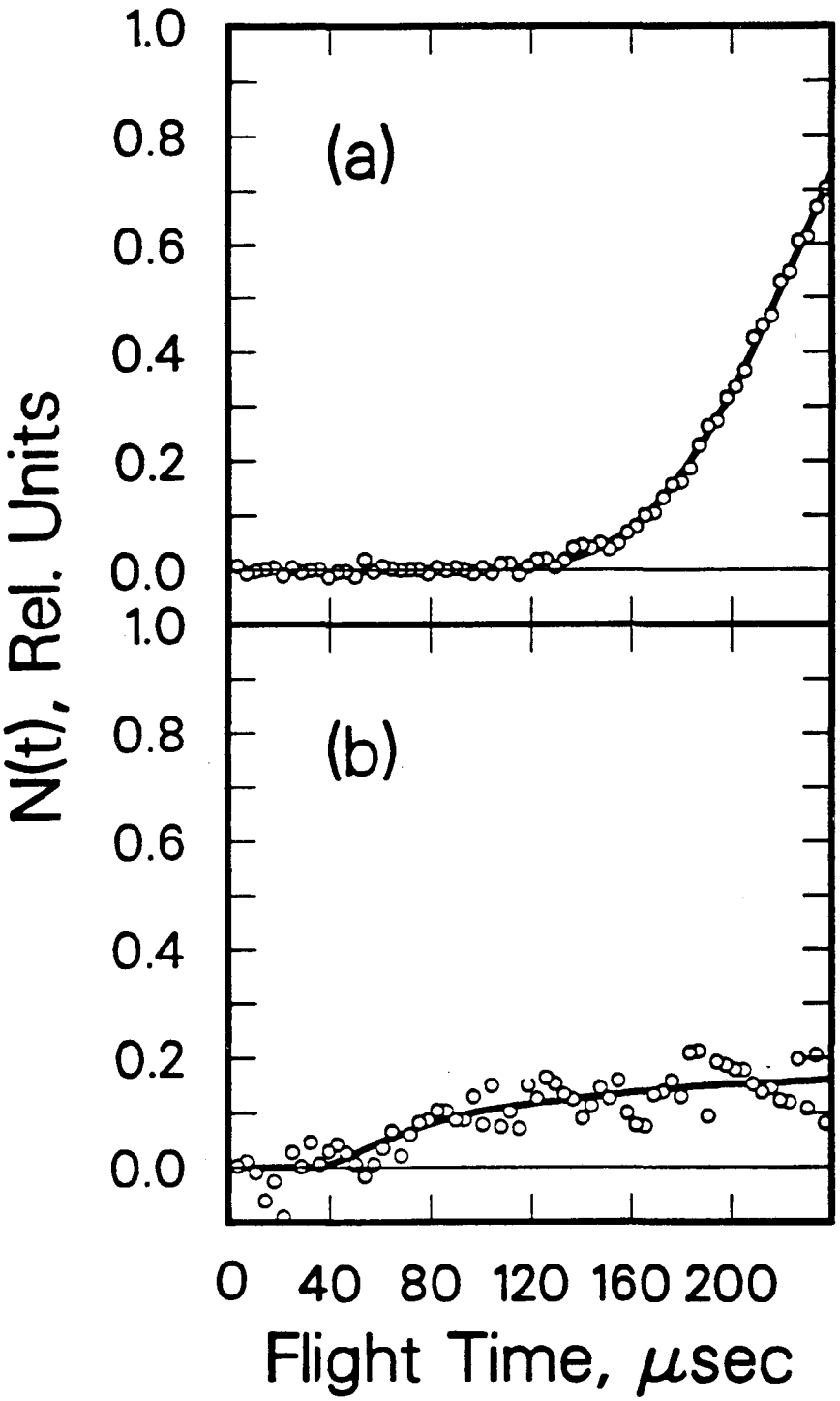
1.0
0.8
0.6
0.4
0.2
0.0
(a)
1.0
0.8
0.6
0.4
0.2
0.0
(b)
N(t), Rel. Units
0 40 80 120 160 200
Flight Time, μsec
XBL 904-1396

Figure 6

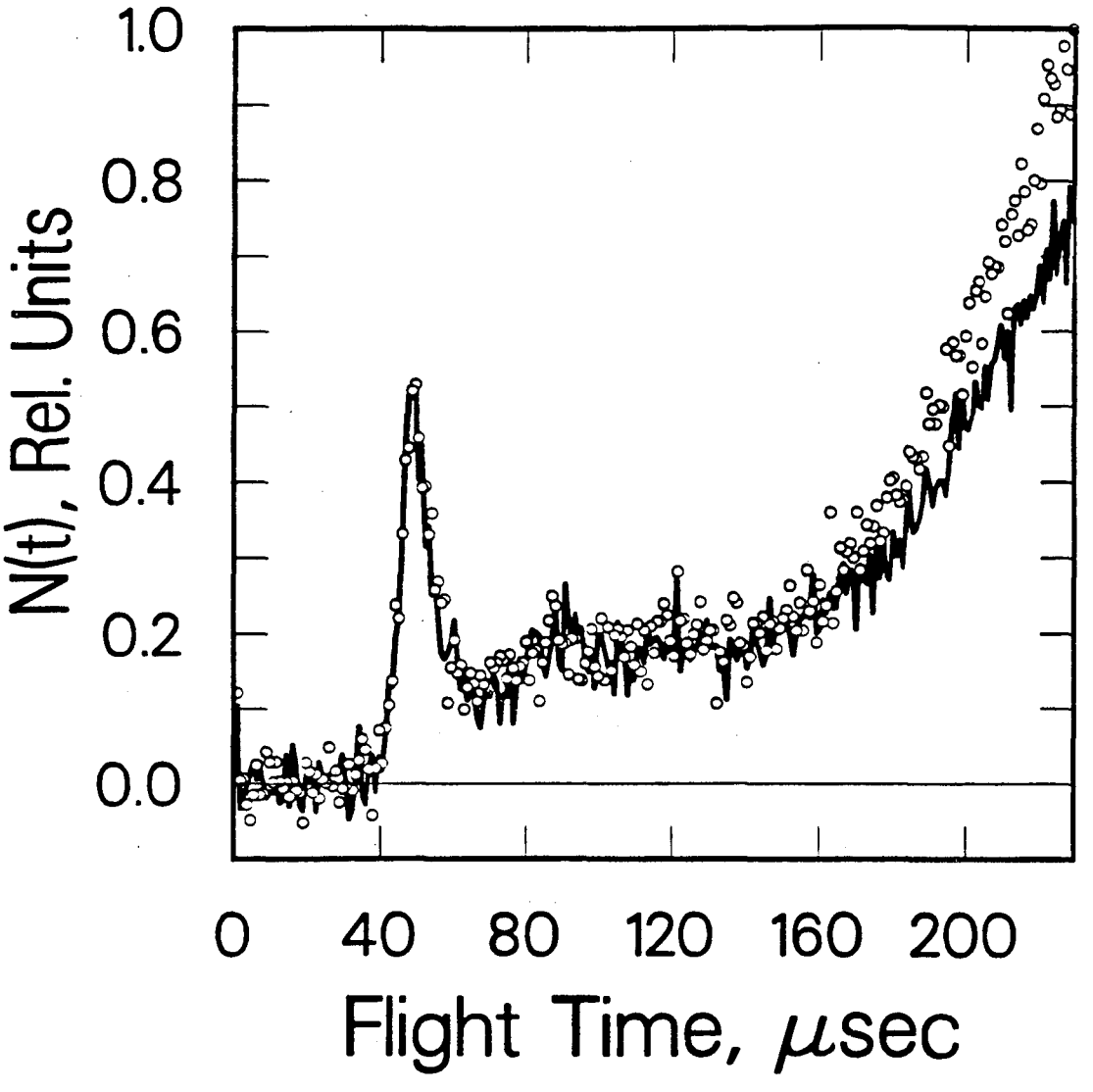

XBL 904-1373

Figure 7

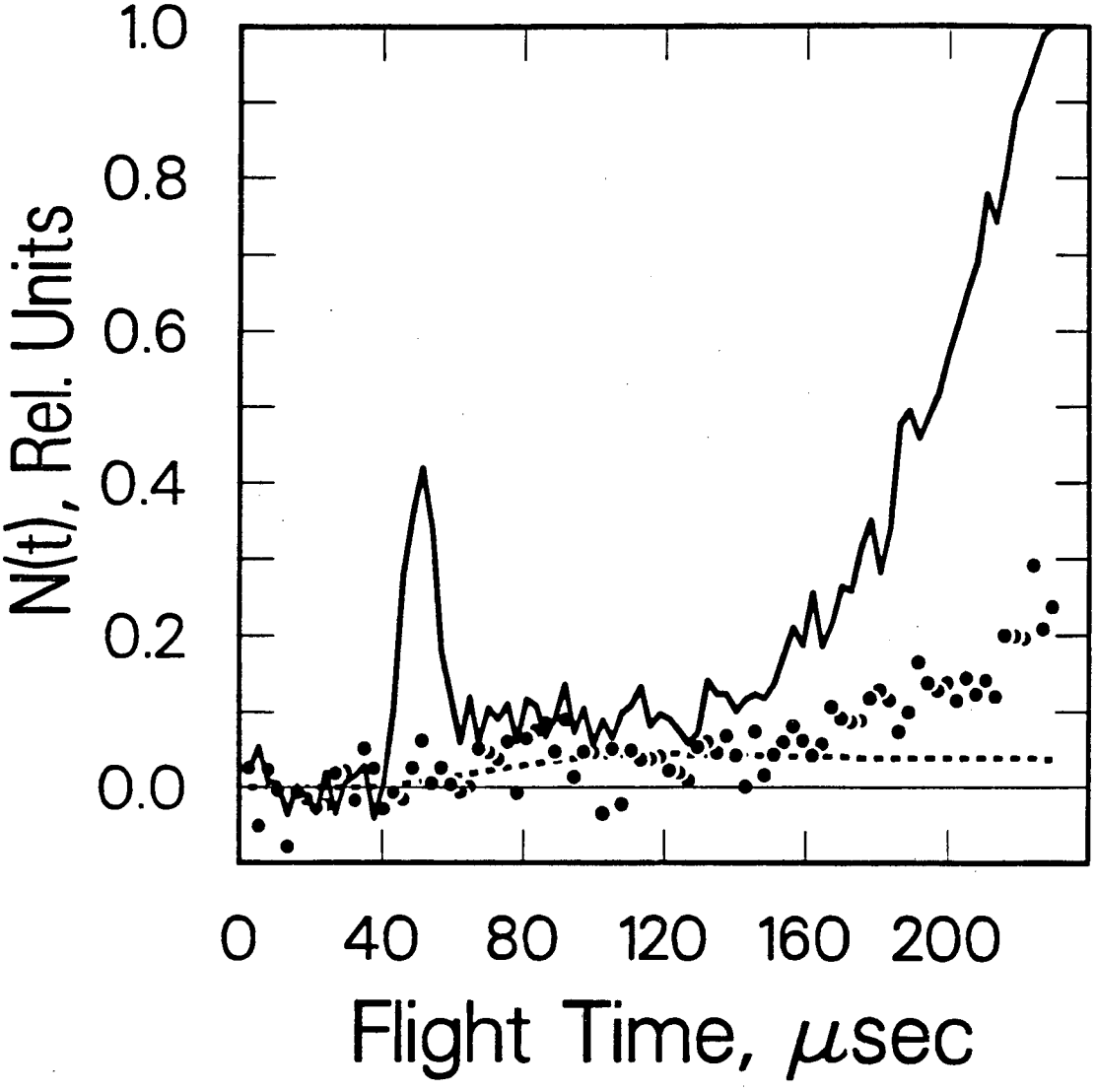
1.0
0.8
0.6
0.4
0.2
0.0
N(t), Rel. Units
0
40
80
120
160
200
Flight Time, μsec
XBL 904-1374

Figure 8

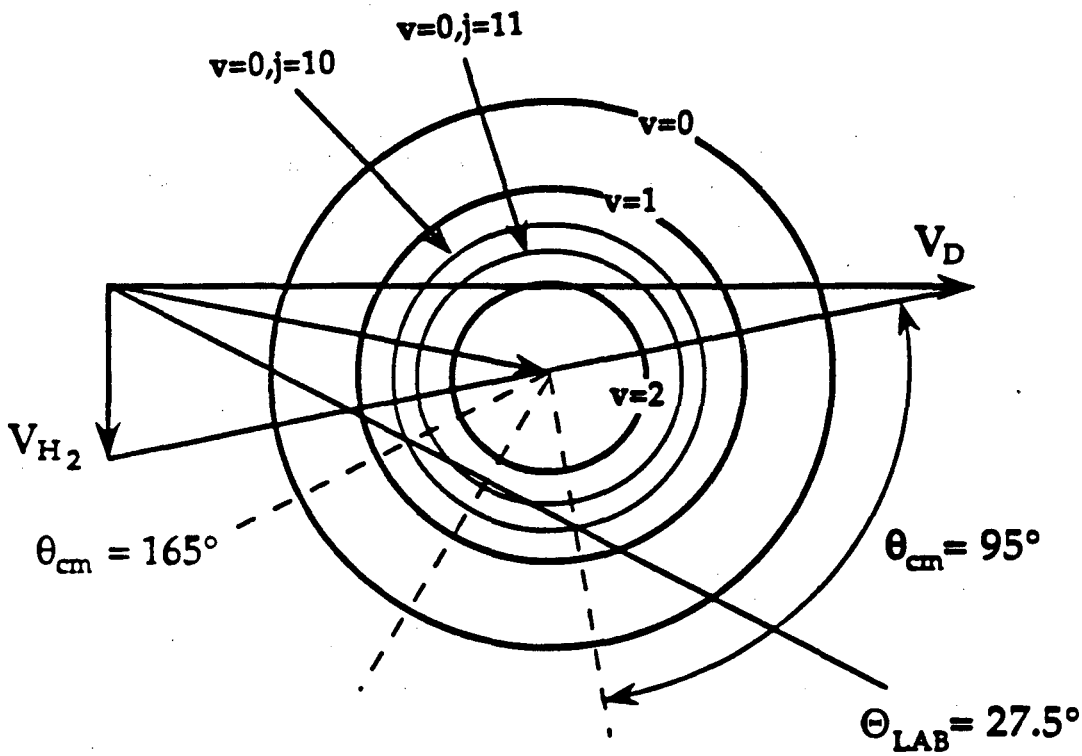
v=0,j=11
v=0,j=10
v=0
v=1
v=2
V_D
V_{H_2}
θ_{cm} = 165°
θ_{cm}= 95°
Θ_{LAB}= 27.5°
XBL 904-1398

Figure 9

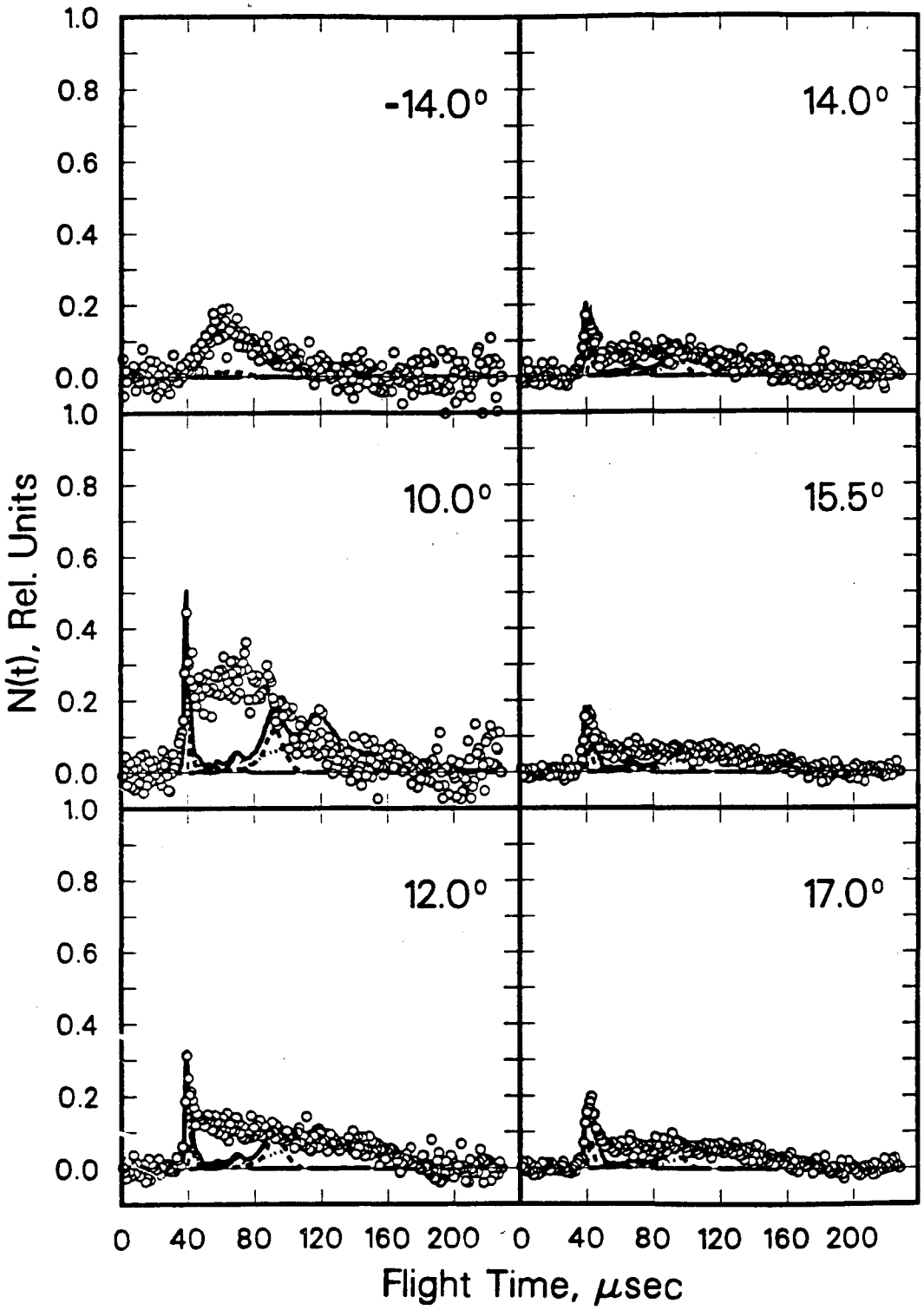
-14.0°
14.0°
10.0°
15.5°
12.0°
17.0°
N(t), Rel. Units
Flight Time, μsec
0 40 80 120 160 200
1.0
0.8
0.6
0.4
0.2
0.0
XBL 904-1375

Figure 10a

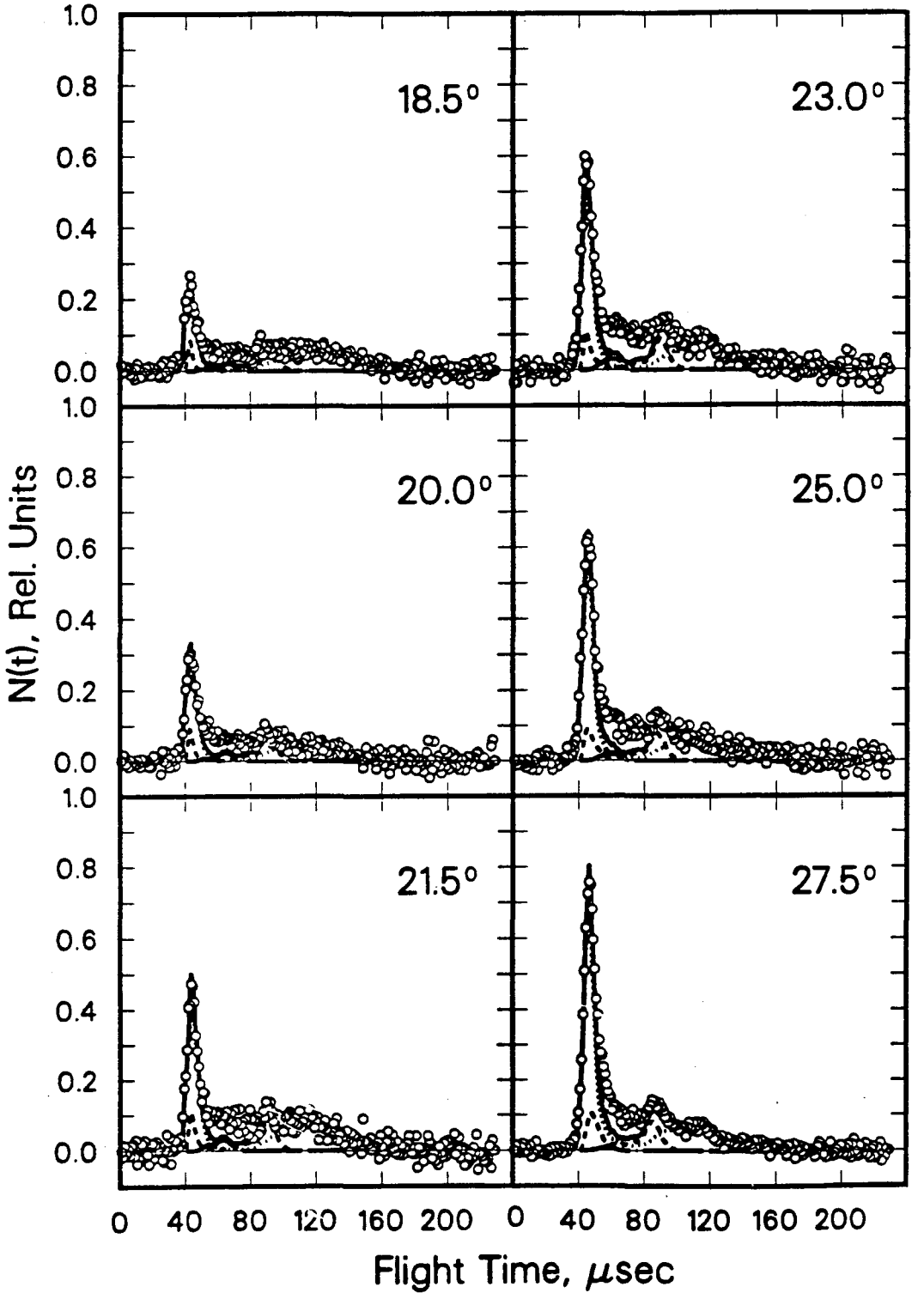
18.5°
23.0°
20.0°
25.0°
21.5°
27.5°
N(t), Rel. Units
1.0
0.8
0.6
0.4
0.2
0.0
0
40
80
120
160
200
Flight Time, μsec
XBL 904-1376

Figure 10b

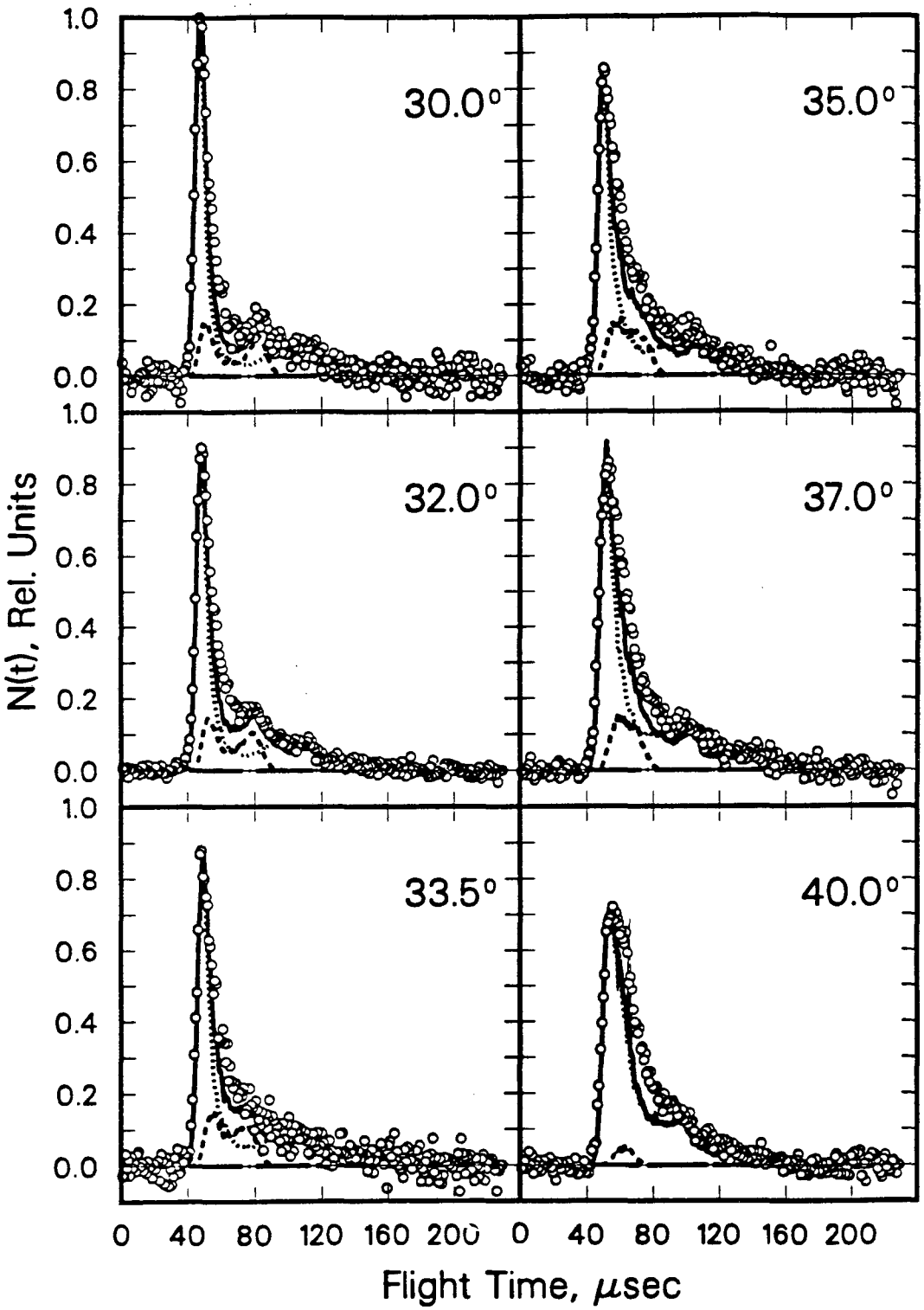
30.0°
35.0°
32.0°
37.0°
33.5°
40.0°
N(t), Rel. Units
Flight Time, μsec
0 40 80 120 160 200
XBL 904-1377

Figure 10c

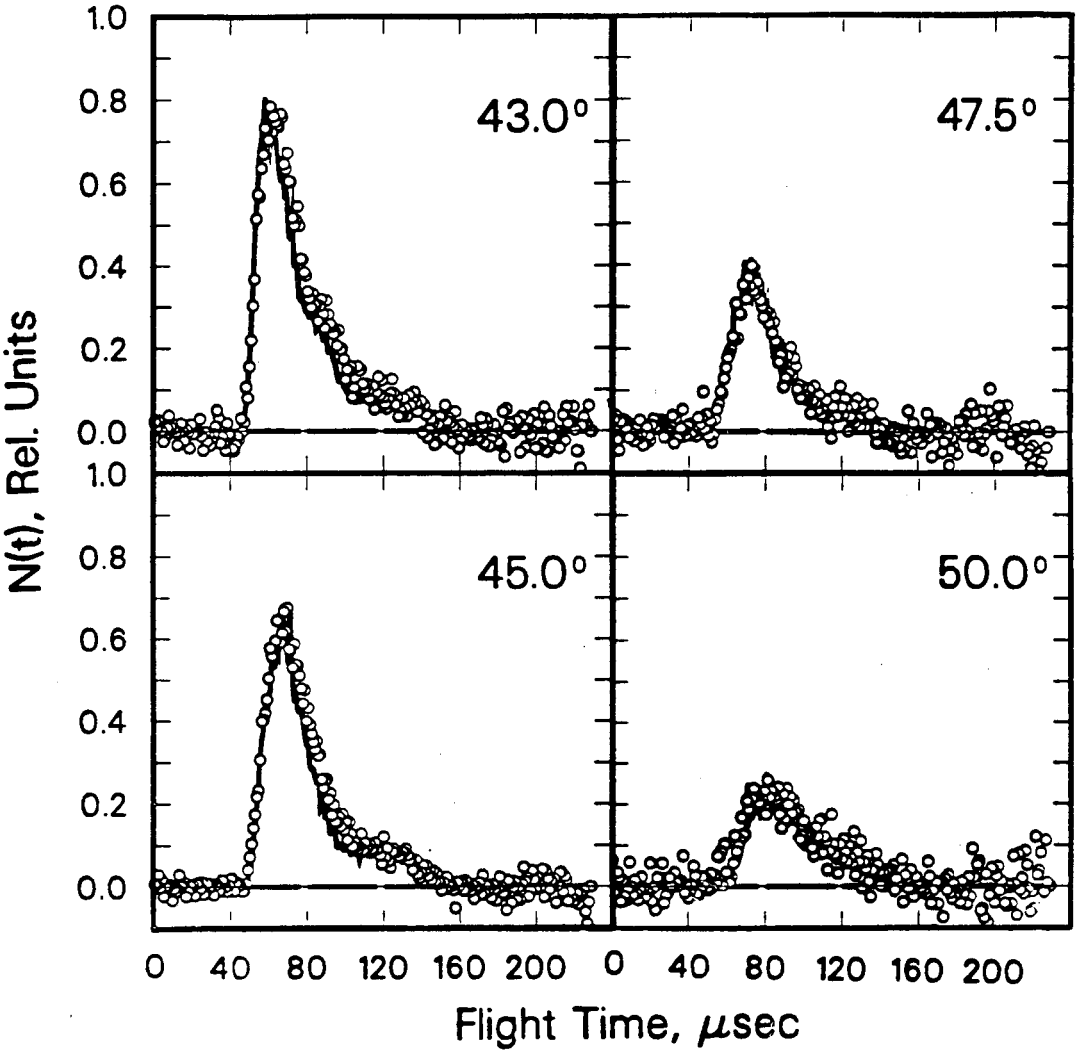
43.0°
47.5°
45.0°
50.0°
N(t), Rel. Units
1.0
0.8
0.6
0.4
0.2
0.0
0
40
80
120
160
200
Flight Time, μsec
XBL 904-1385

Figure 10d

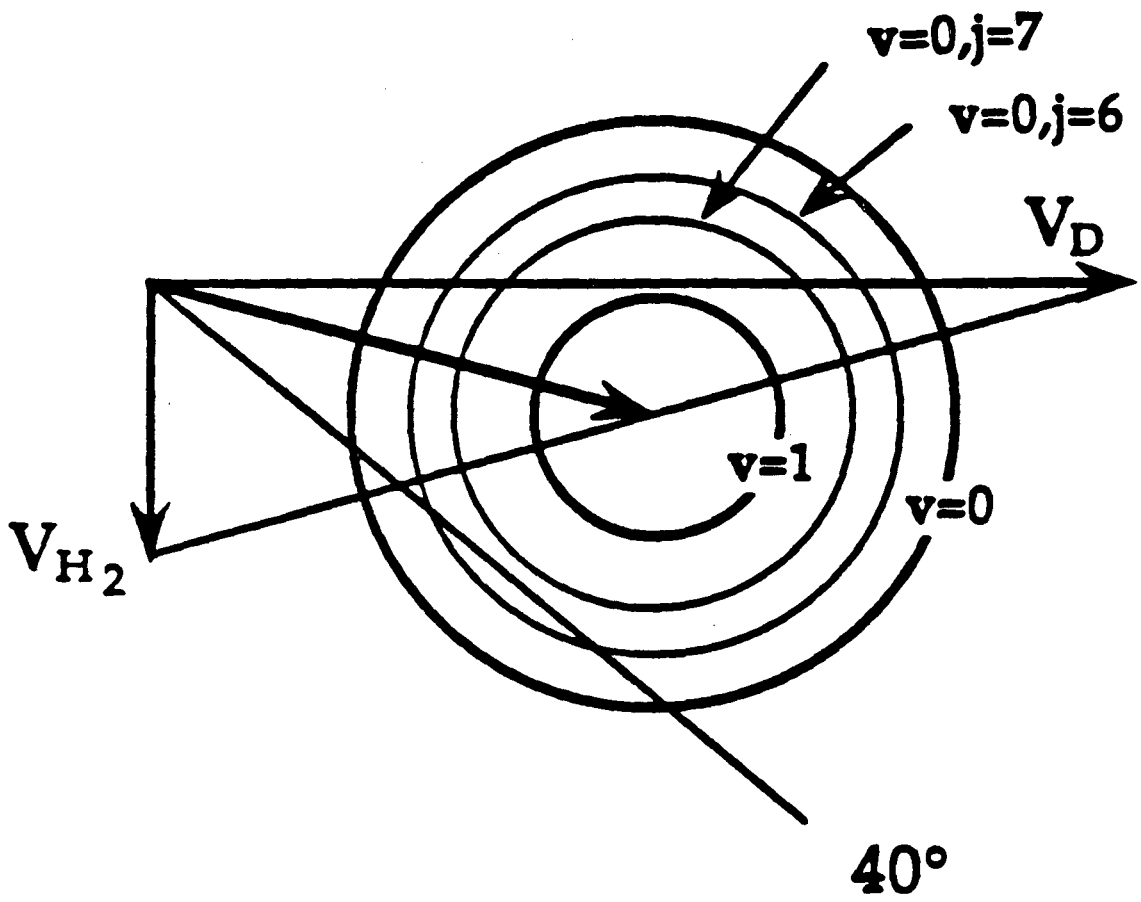

XBL 904-1399

Figure 11

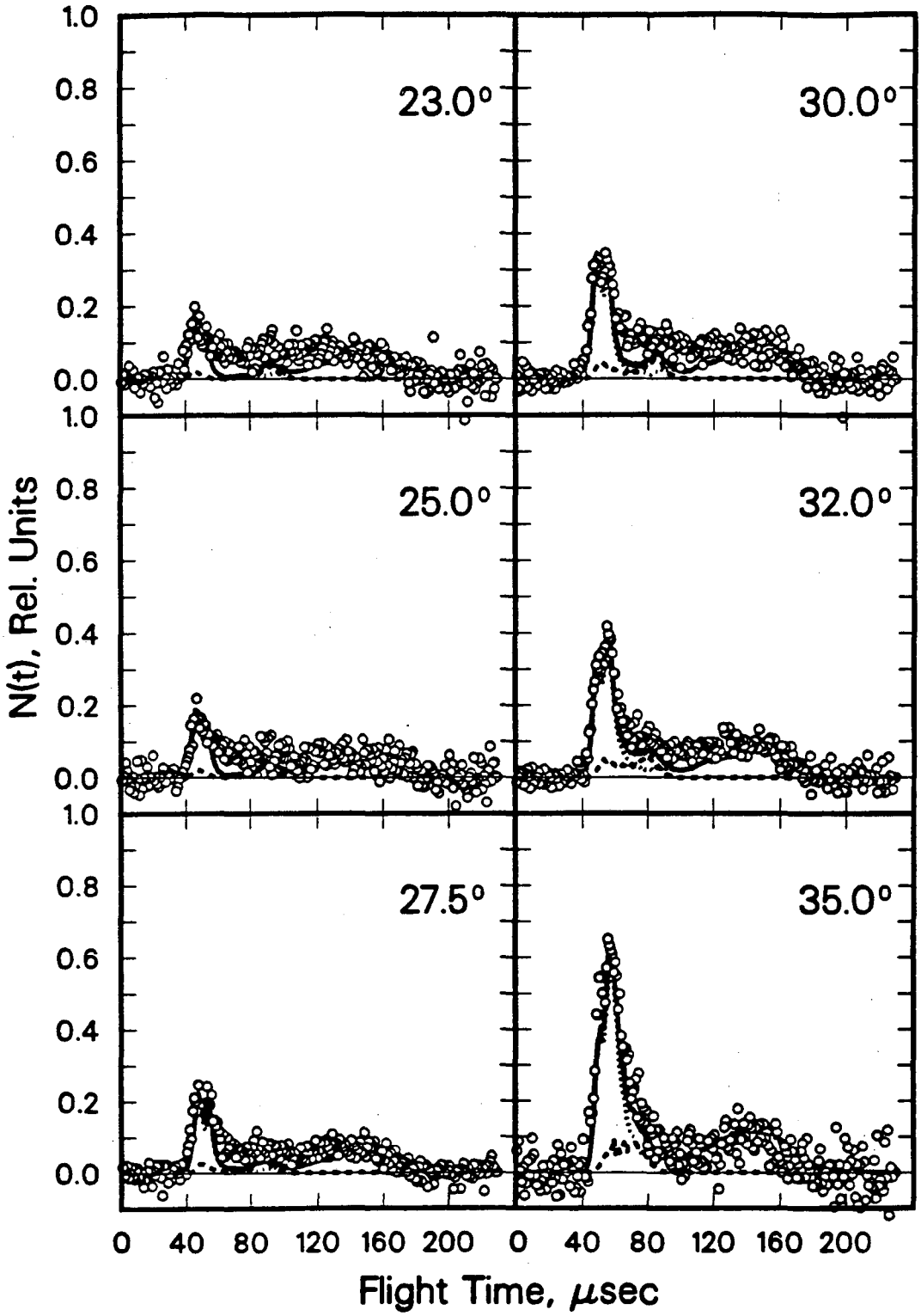

Figure 12a XBL 904-1379

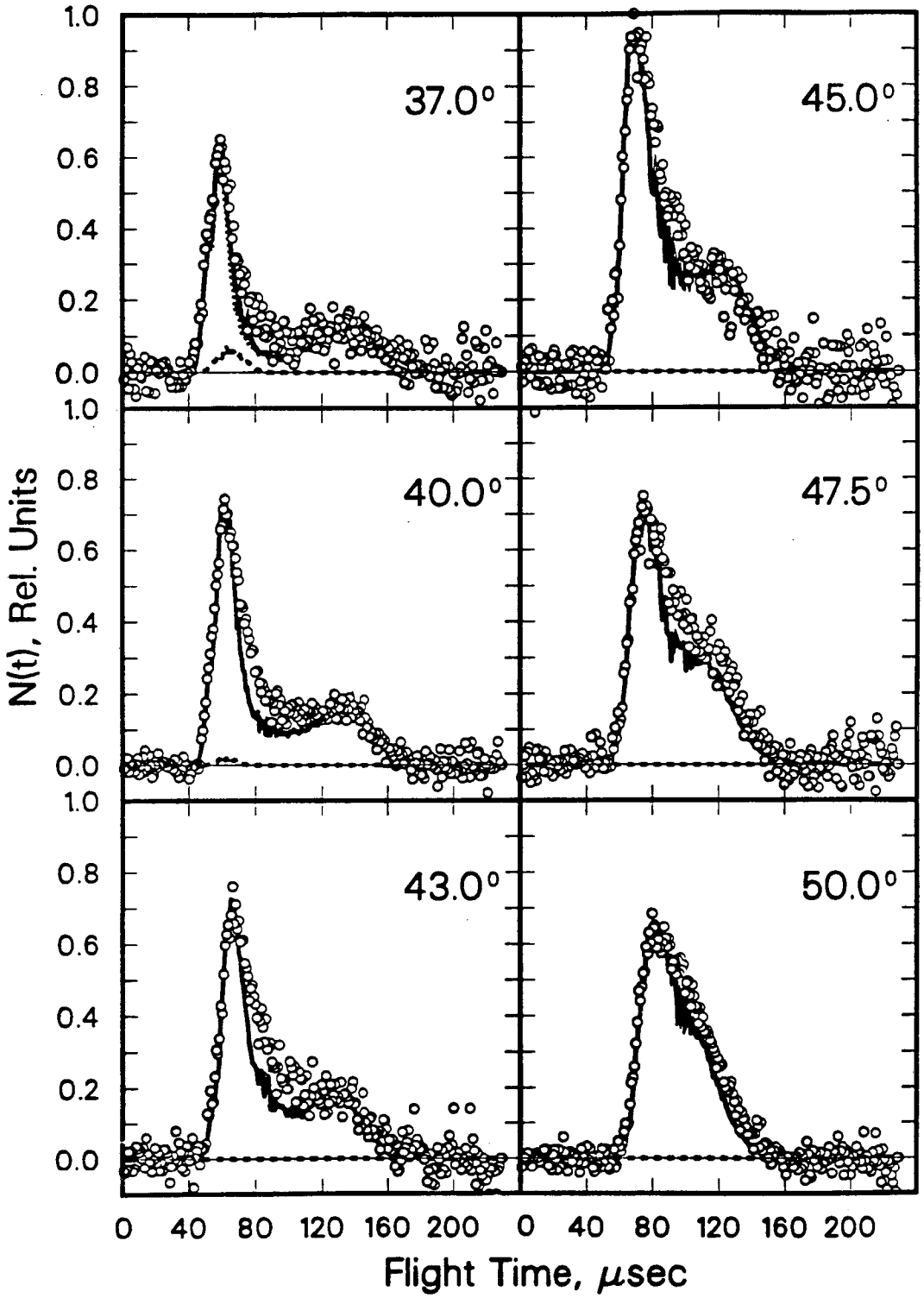
37.0°
45.0°
40.0°
47.5°
43.0°
50.0°
N(t), Rel. Units
1.0
0.8
0.6
0.4
0.2
0.0
0 40 80 120 160 200
Flight Time, μsec
XBL 904-1380

Figure 12b

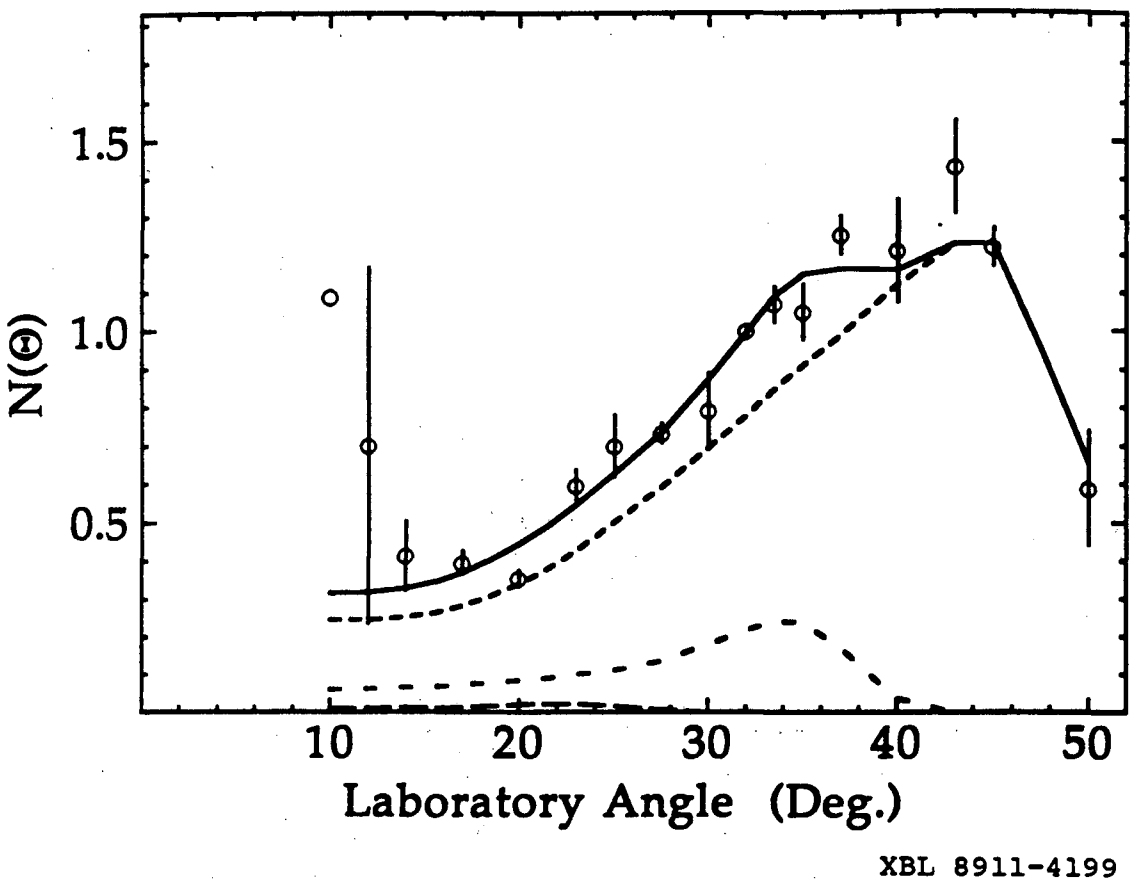

Figure 13

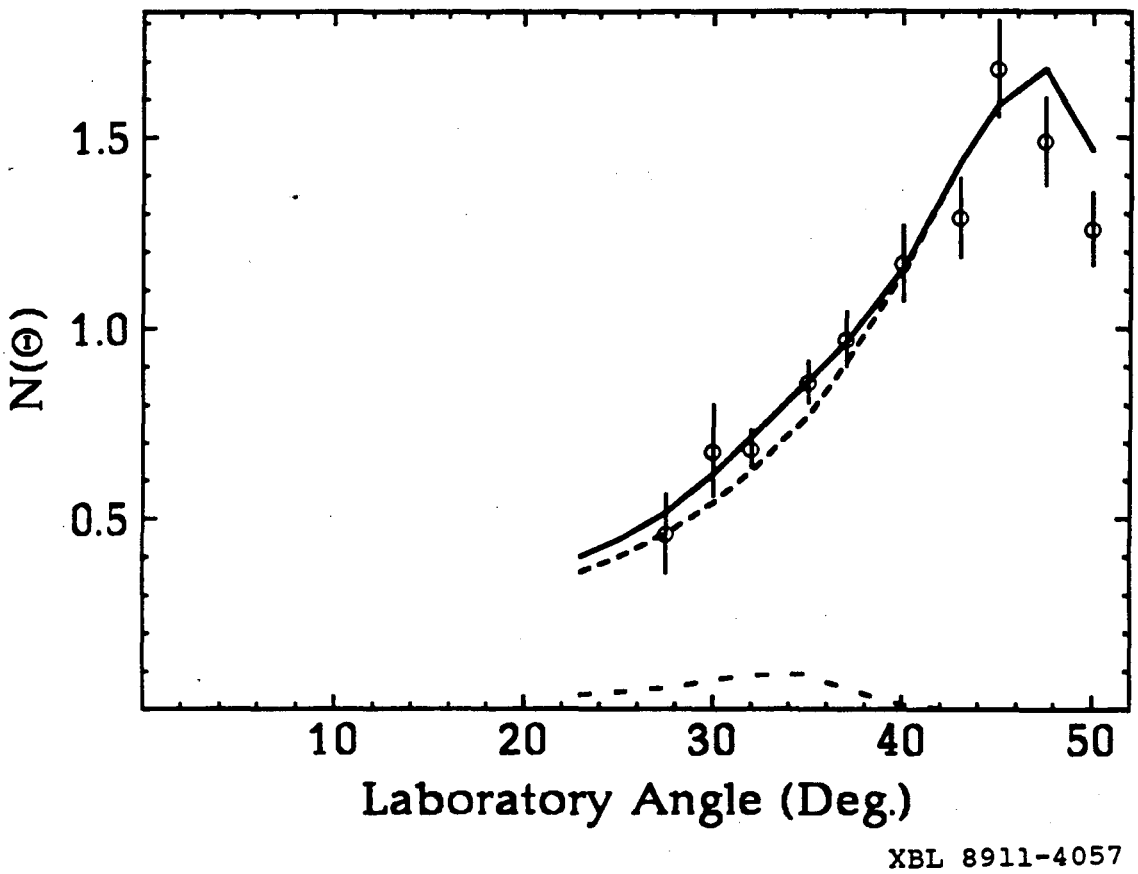

Figure 14

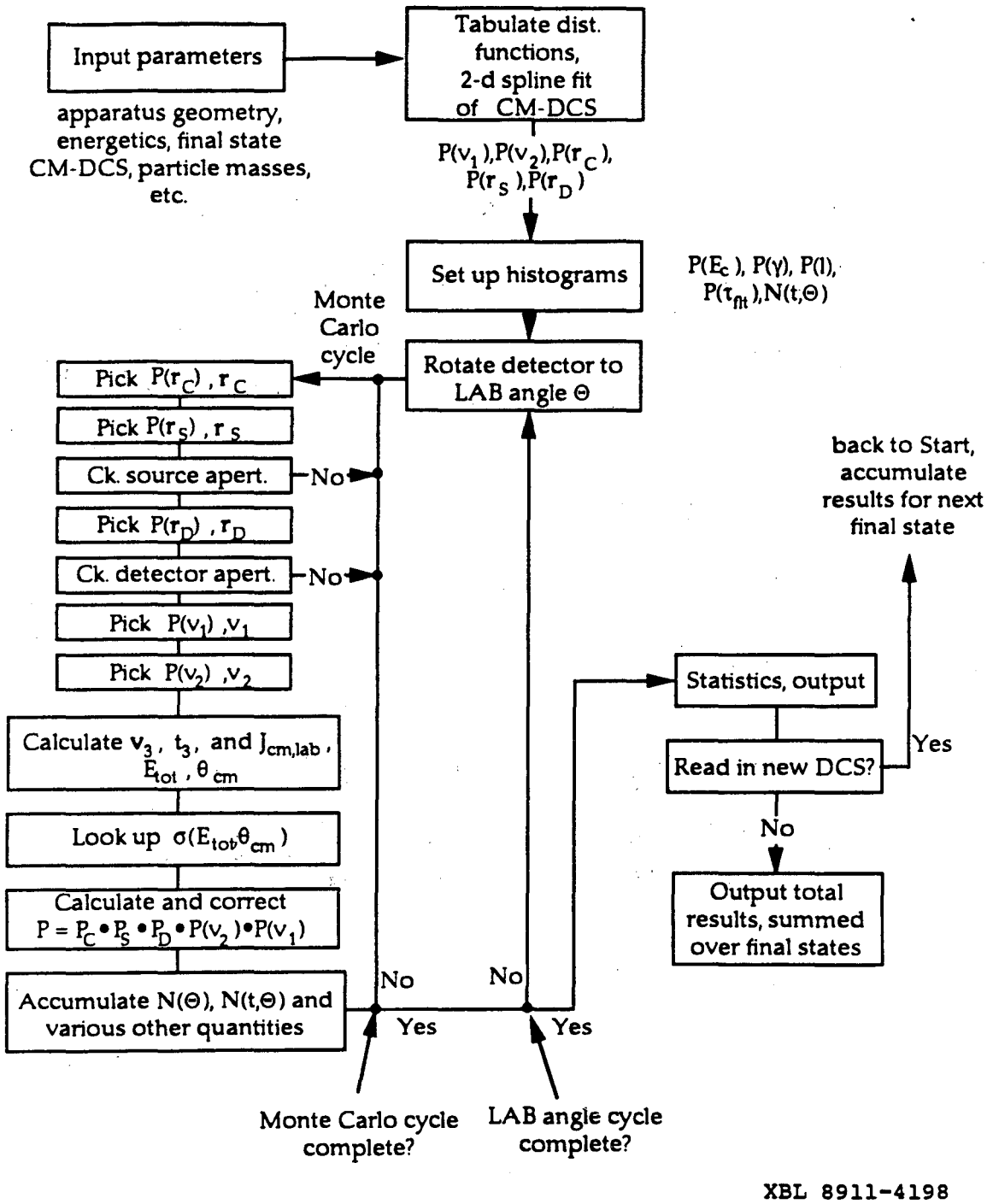
Input parameters
apparatus geometry, energetics, final state CM-DCS, particle masses, etc.
Tabulate dist. functions, 2-d spline fit of CM-DCS
P(v1),P(v2),P(rC), P(rS),P(rD)
Set up histograms
P(Ec), P(γ), P(l), P(τfit),N(t,Θ)
Monte Carlo cycle
Rotate detector to LAB angle Θ
Pick P(rC) , rC
Pick P(rS) , rS
Ck. source apert.
No
Pick P(rD) , rD
Ck. detector apert.
No
Pick P(v1) ,v1
Pick P(v2) ,v2
Calculate v3 , t3 , and Jcm,lab , Etot , θcm
Look up σ(Etot,θcm)
Calculate and correct P = PC • PS • PD • P(v2) • P(v1)
Accumulate N(Θ), N(t,Θ) and various other quantities
No
Yes
No
Yes
Monte Carlo cycle complete?
LAB angle cycle complete?
Statistics, output
Read in new DCS?
Yes
No
Output total results, summed over final states
back to Start, accumulate results for next final state
XBL 8911-4198

Figure 15

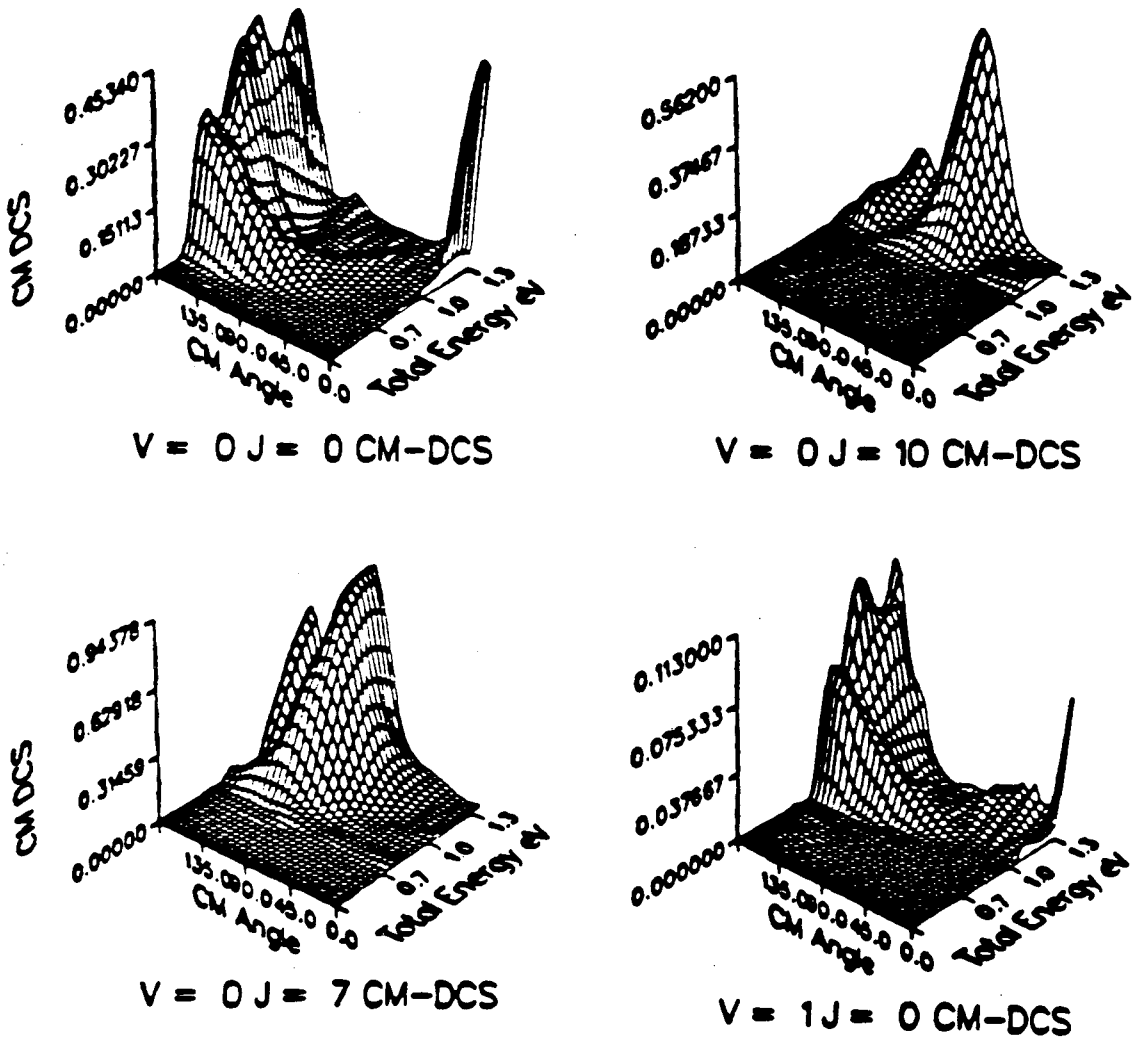
CM DCS
0.45340
0.30227
0.15113
0.00000
135.090.045.0 0.0
CM Angle
0.7 1.0 1.3
Total Energy eV
V = 0 J = 0 CM-DCS
0.56200
0.37467
0.18733
0.00000
V = 0 J = 10 CM-DCS
0.94578
0.62918
0.31459
0.00000
V = 0 J = 7 CM-DCS
0.113000
0.075333
0.037667
0.000000
V = 1 J = 0 CM-DCS
XBL 304-1400

Figure 16

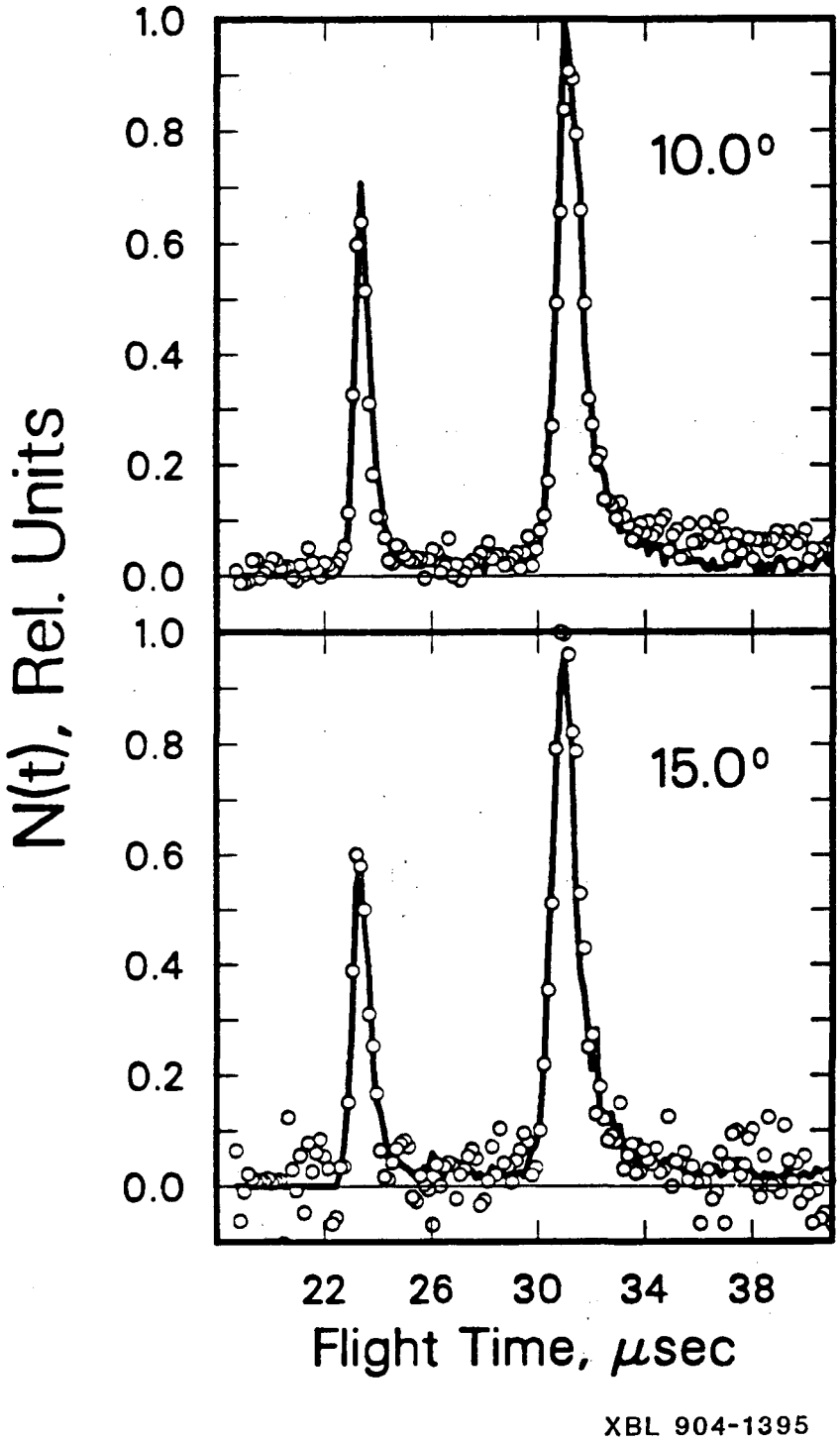
1.0
0.8
0.6
0.4
0.2
0.0
10.0°
1.0
0.8
0.6
0.4
0.2
0.0
15.0°
N(t), Rel. Units
22
26
30
34
38
Flight Time, μsec
XBL 904-1395

Figure 17

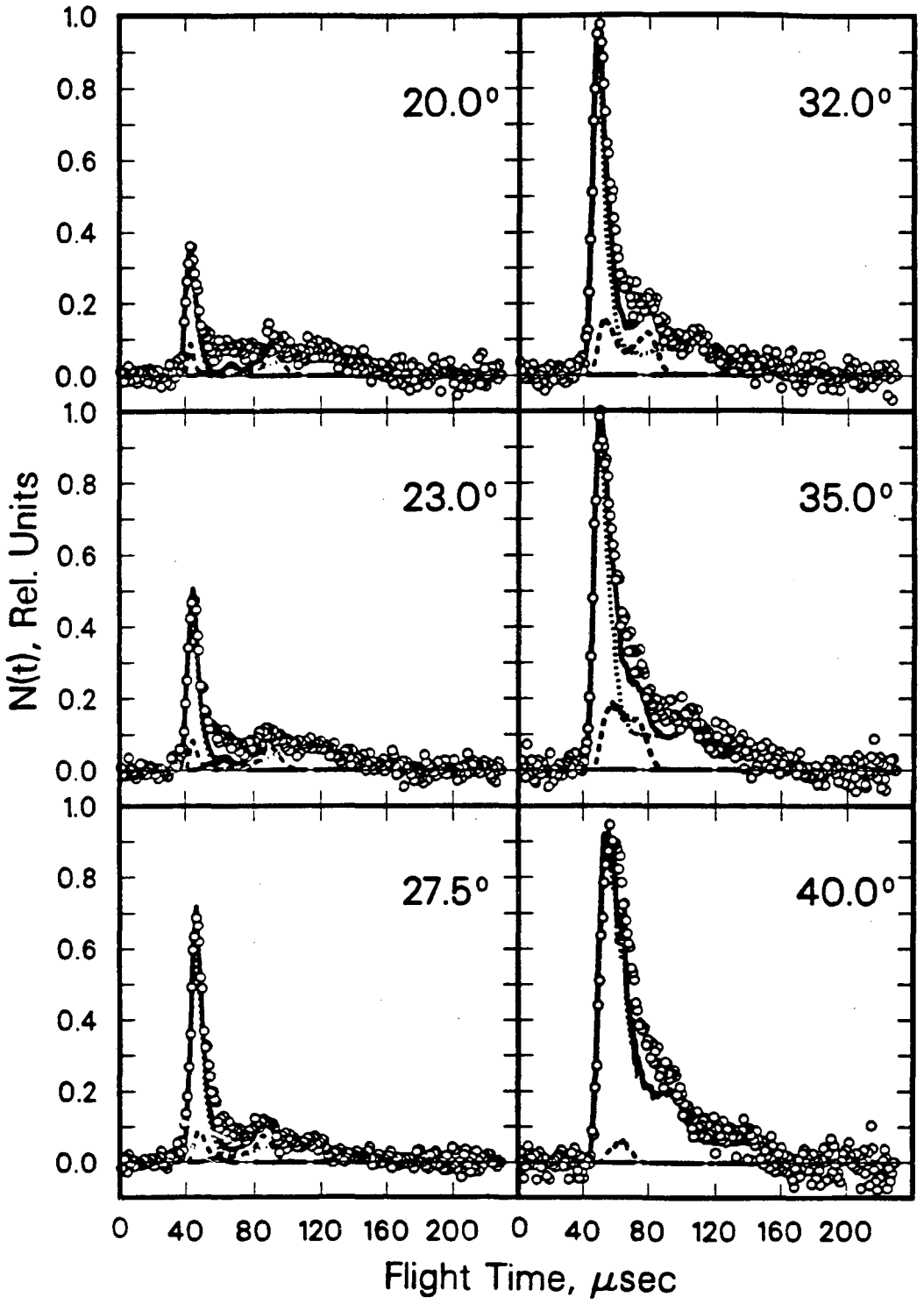
20.0°
32.0°
23.0°
35.0°
27.5°
40.0°
N(t), Rel. Units
Flight Time, μsec
0
40
80
120
160
200
0.0
0.2
0.4
0.6
0.8
1.0
XBL 904-1381

Figure 18

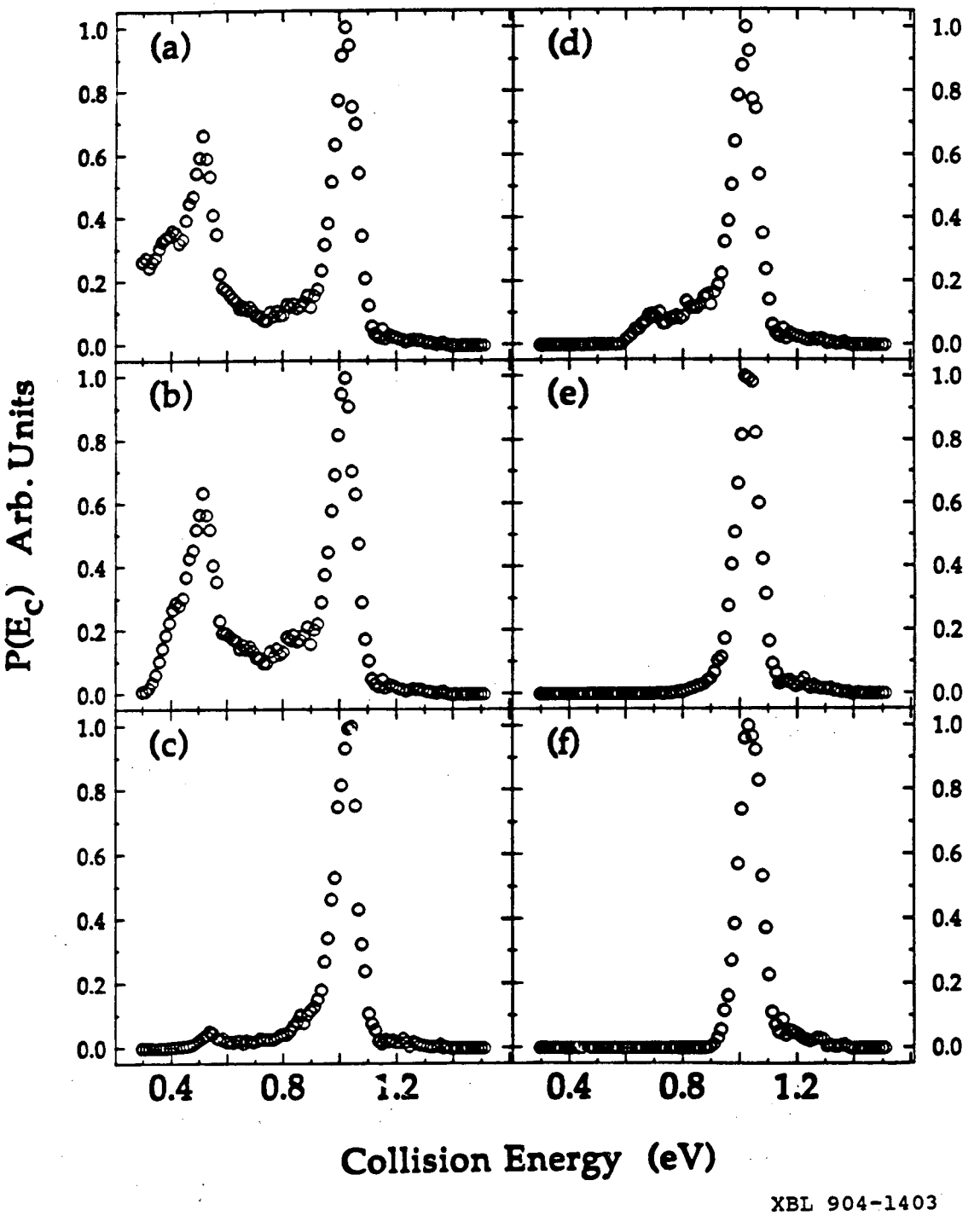
(a)
(b)
(c)
(d)
(e)
(f)
1.0
0.8
0.6
0.4
0.2
0.0
0.4
0.8
1.2
P(E_C) Arb. Units
Collision Energy (eV)
XBL 904-1403

Figure 19

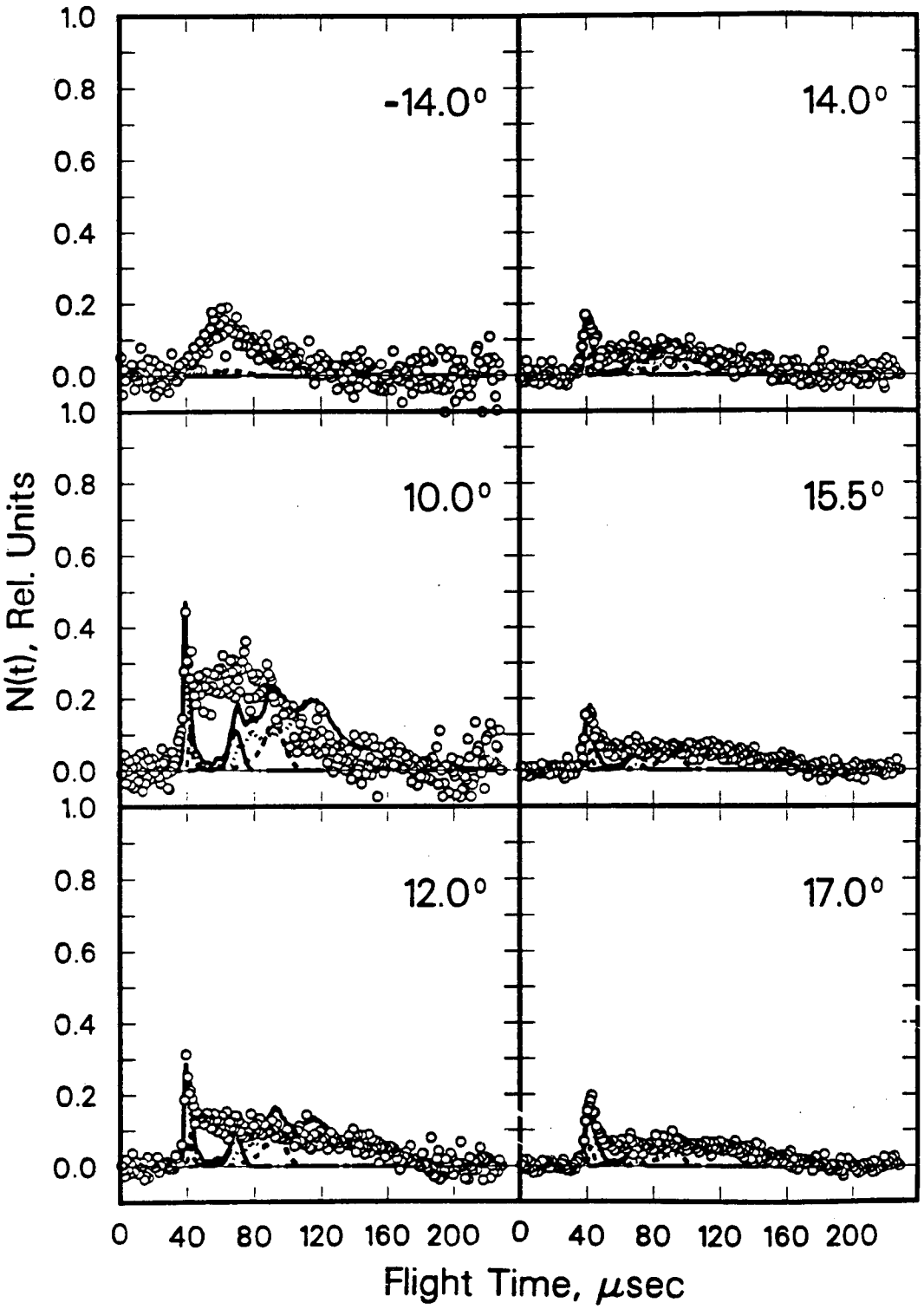
-14.0°
14.0°
10.0°
15.5°
12.0°
17.0°
N(t), Rel. Units
1.0
0.8
0.6
0.4
0.2
0.0
0
40
80
120
160
200
Flight Time, μsec
XBL 904-1382

Figure 20a

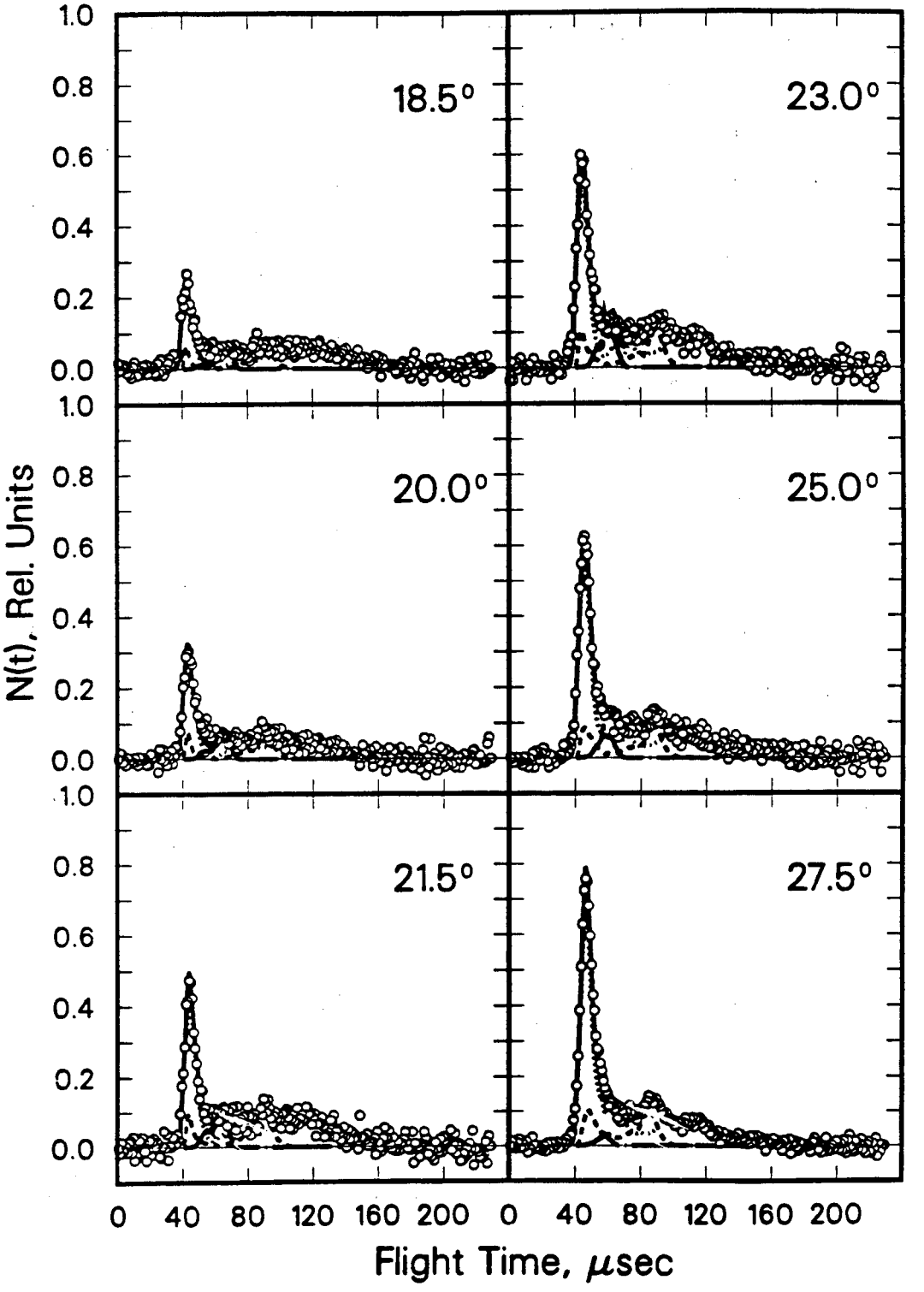
18.5°
23.0°
20.0°
25.0°
21.5°
27.5°
N(t), Rel. Units
Flight Time, μsec
0 40 80 120 160 200
0.0 0.2 0.4 0.6 0.8 1.0
XBL 904-1383

Figure 20b

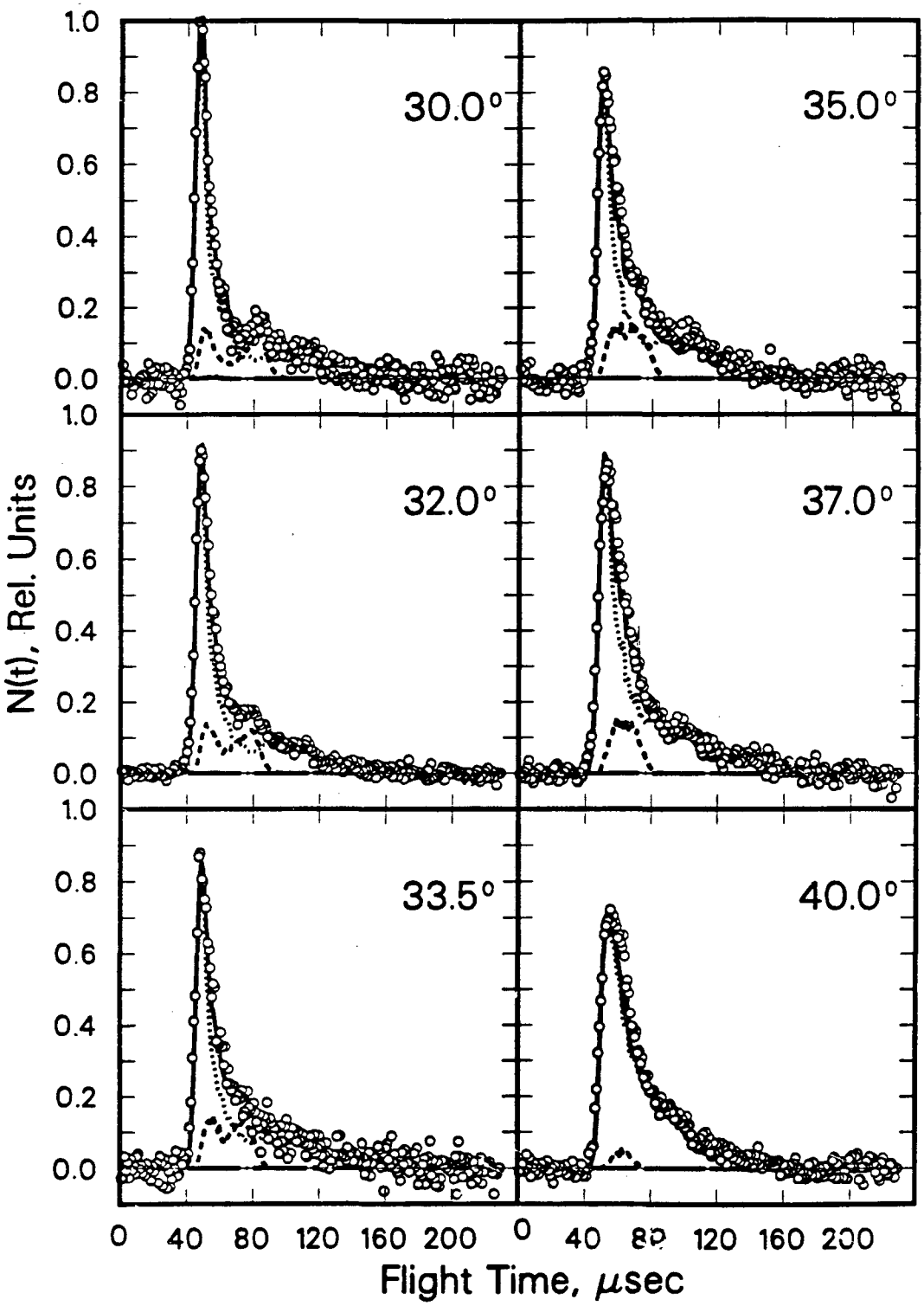
30.0°
35.0°
32.0°
37.0°
33.5°
40.0°
N(t), Rel. Units
Flight Time, μsec
0
40
80
120
160
200
XBL 904-1384

Figure 20c

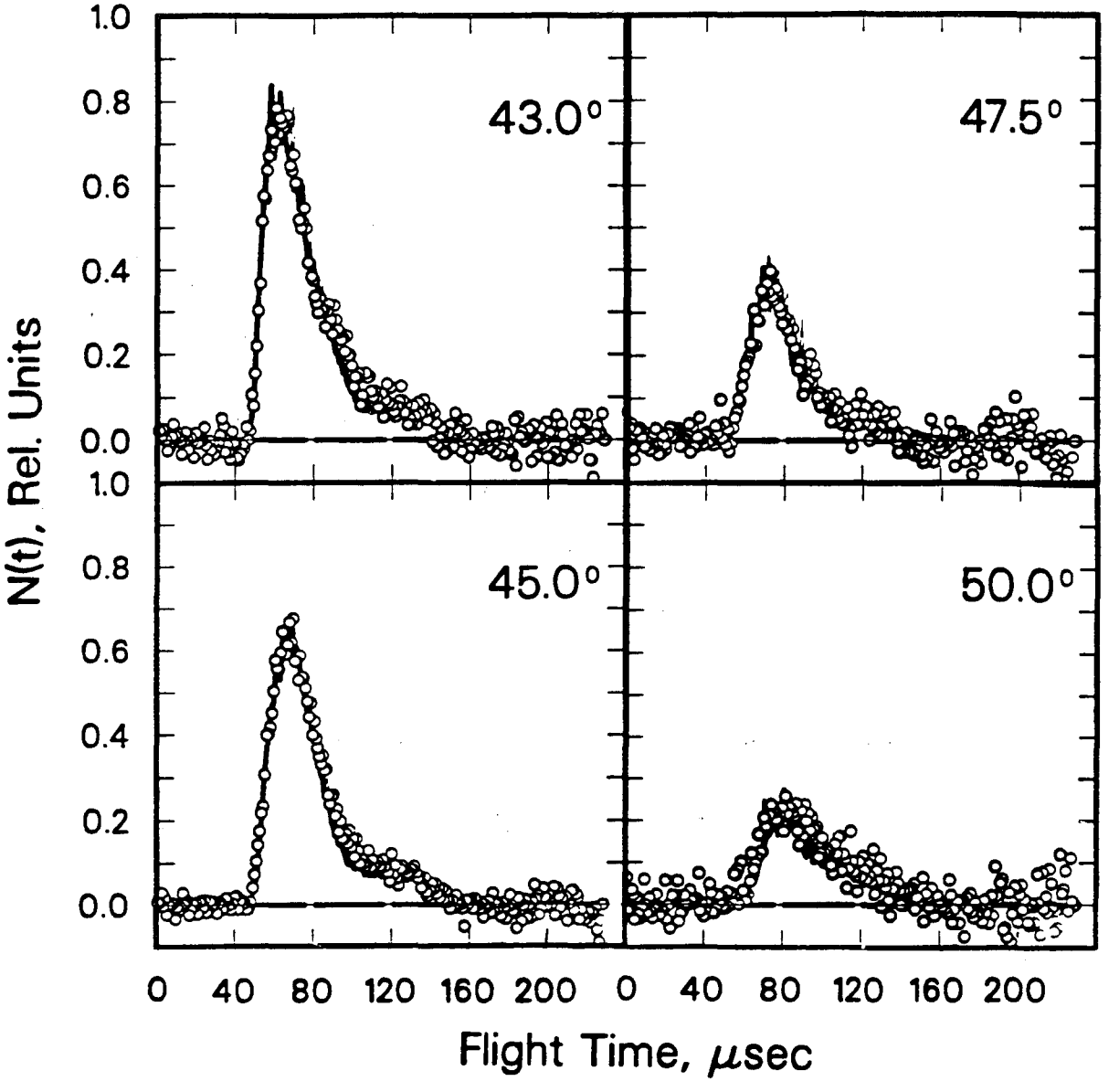

XBL 904-1378

Figure 20d

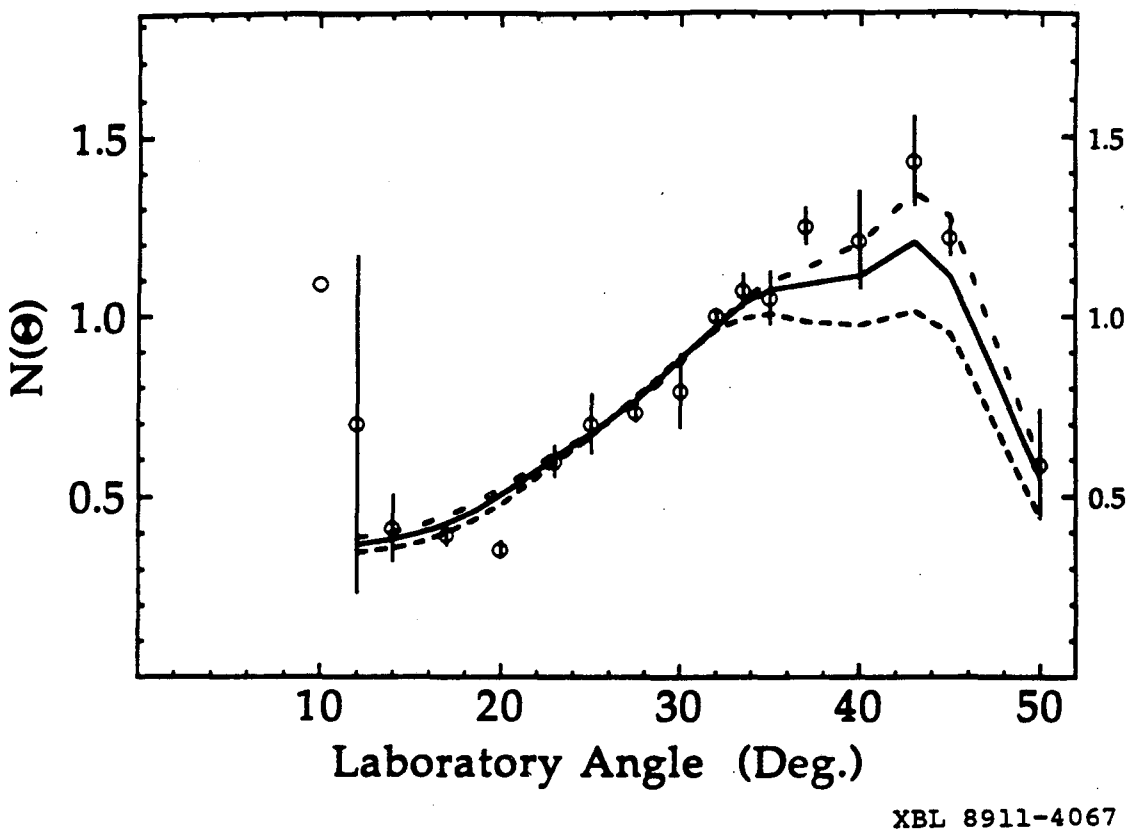

Figure 21

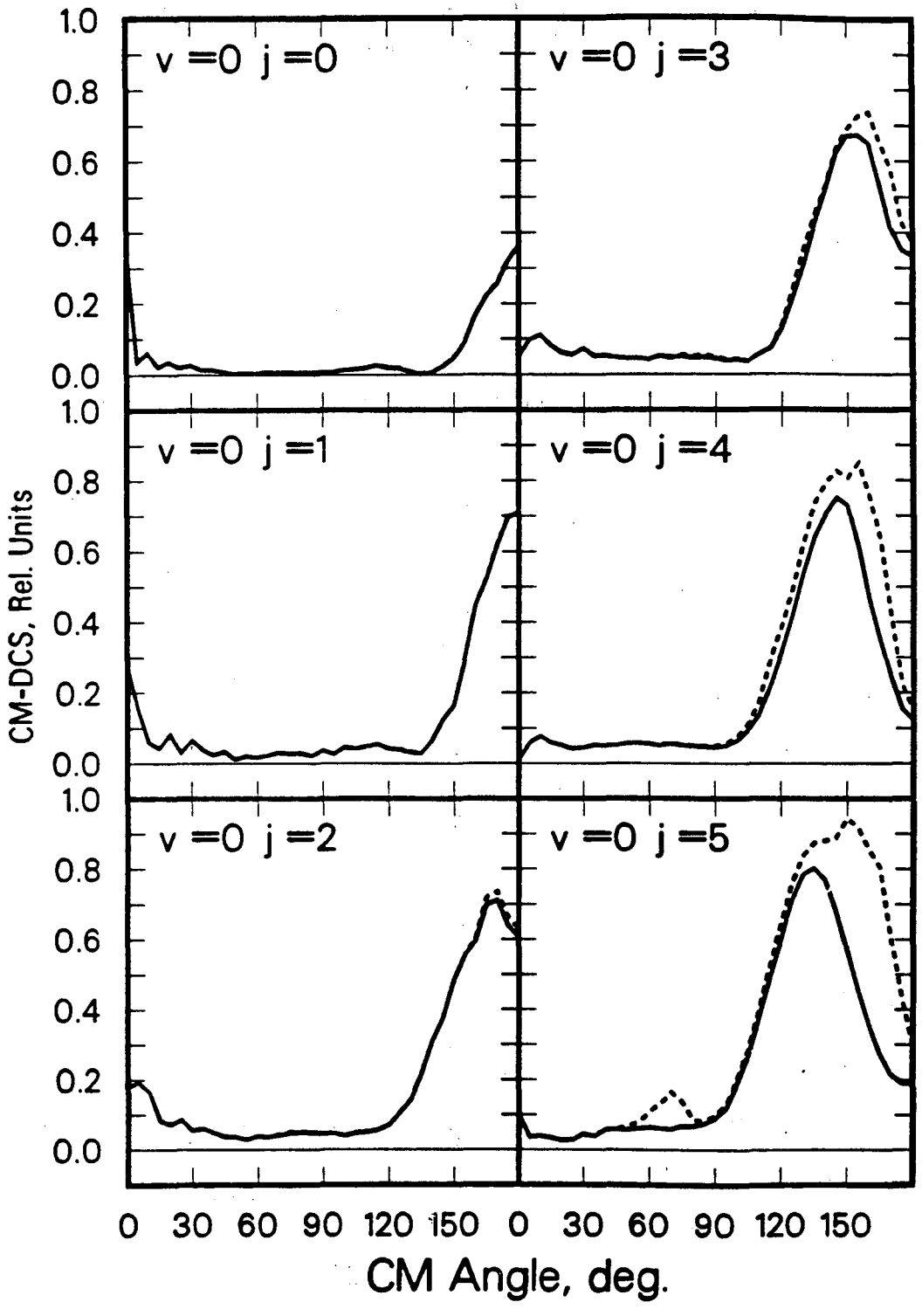

XBL 904-1386

Figure 22a

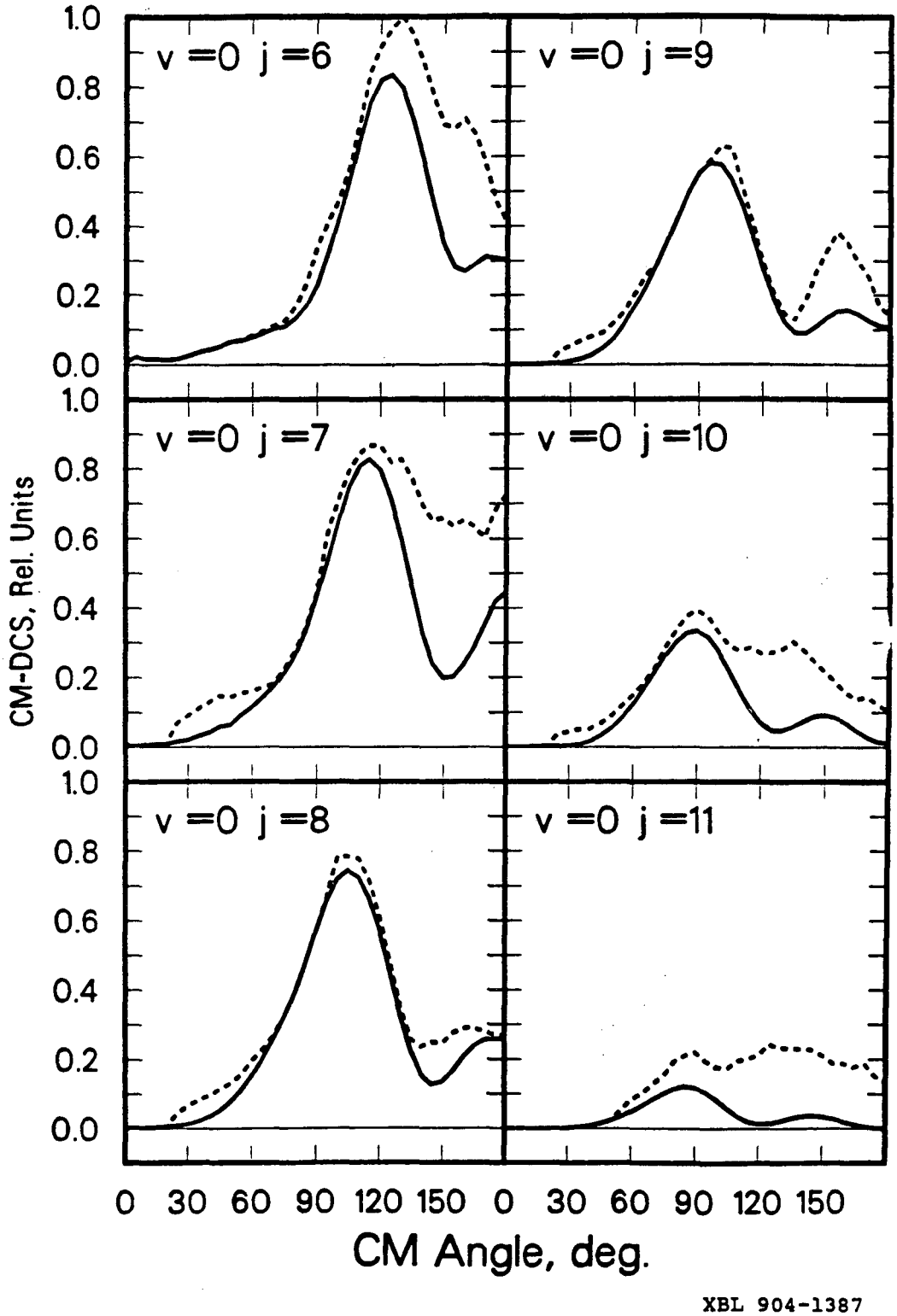
v =0 j =6
v =0 j =9
v =0 j =7
v =0 j =10
v =0 j =8
v =0 j =11
1.0
0.8
0.6
0.4
0.2
0.0
CM-DCS, Rel. Units
0 30 60 90 120 150 0 30 60 90 120 150
CM Angle, deg.
XBL 904-1387

Figure 22b

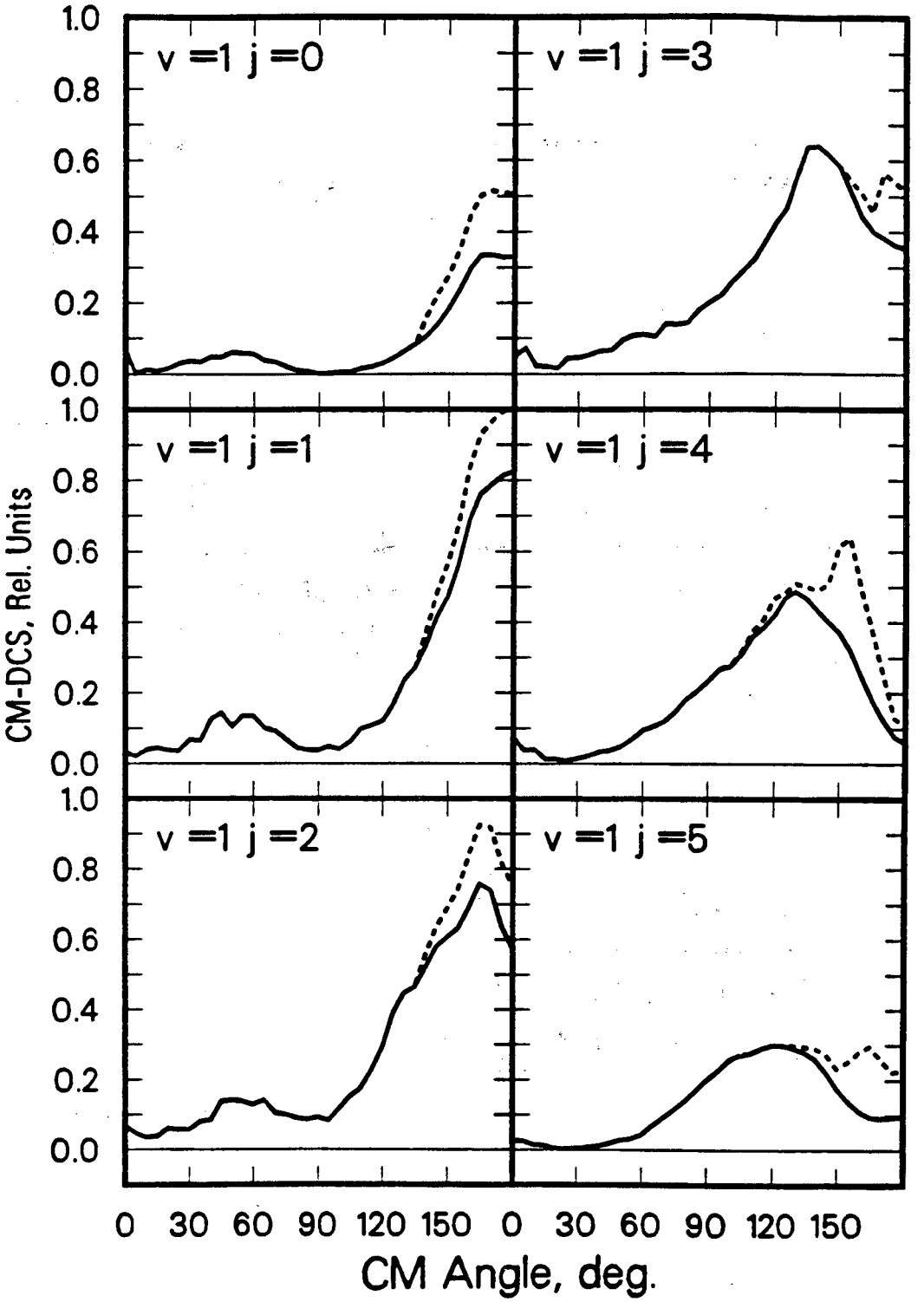
v =1 j =0
v =1 j =3
v =1 j =1
v =1 j =4
v =1 j =2
v =1 j =5
1.0
0.8
0.6
0.4
0.2
0.0
CM-DCS, Rel. Units
0 30 60 90 120 150 0 30 60 90 120 150
CM Angle, deg.
XBL 904-1388

Figure 22c

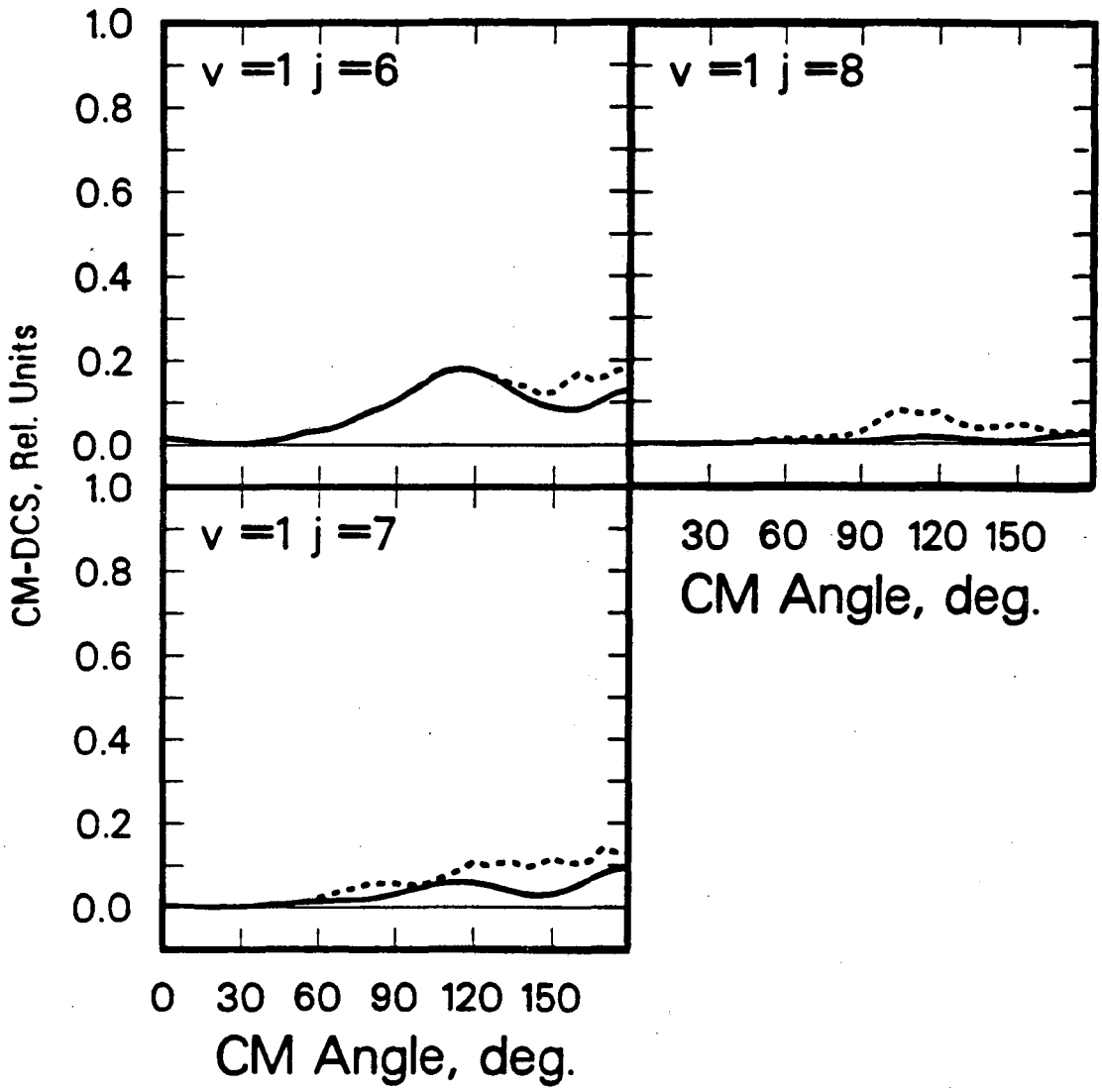

XBL 904-1389

Figure 22d

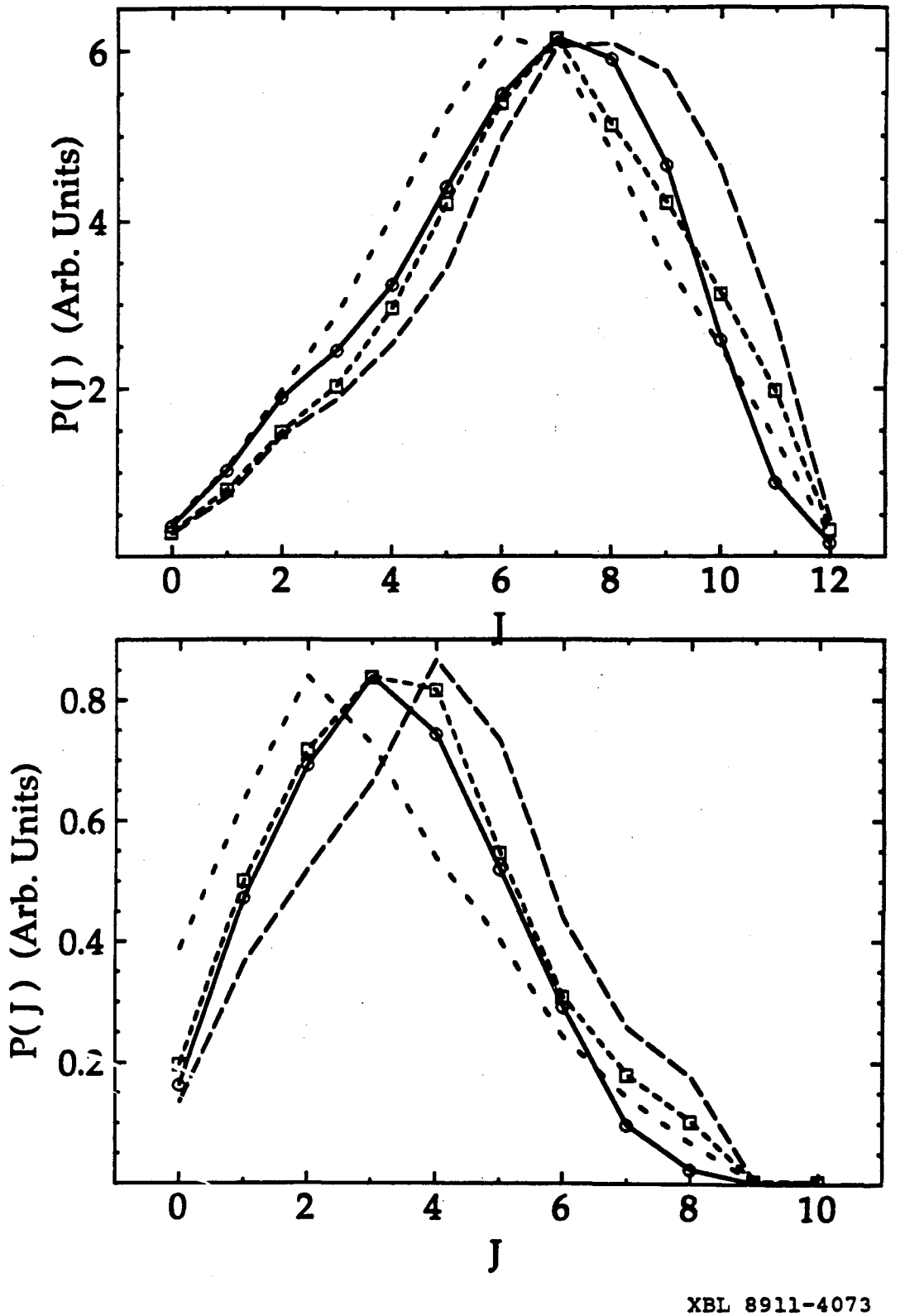

Figure 23

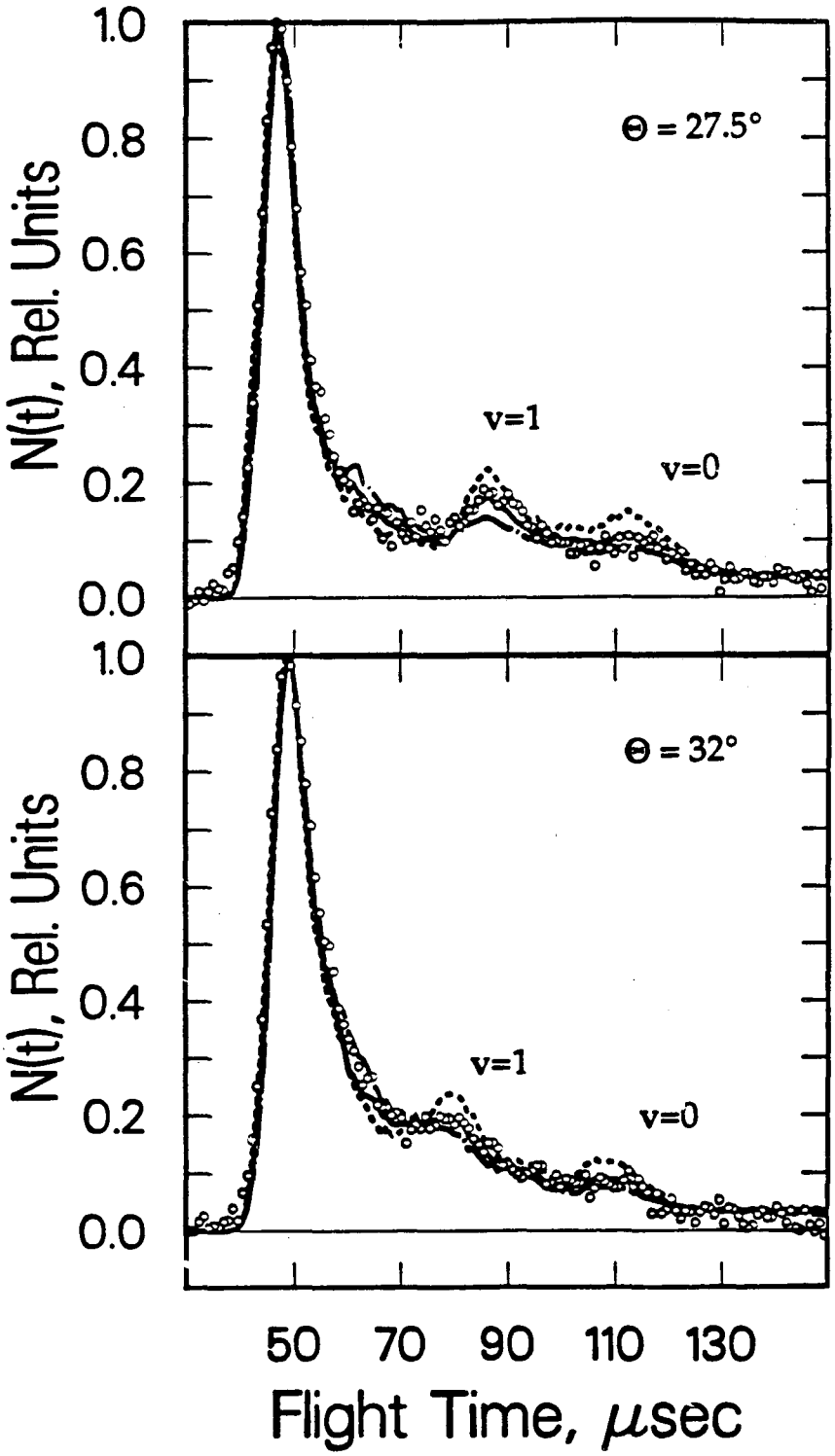
1.0
0.8
0.6
0.4
0.2
0.0
N(t), Rel. Units
Θ = 27.5°
v=1
v=0
Θ = 32°
50 70 90 110 130
Flight Time, μsec
XBL 904-1401

Figure 24

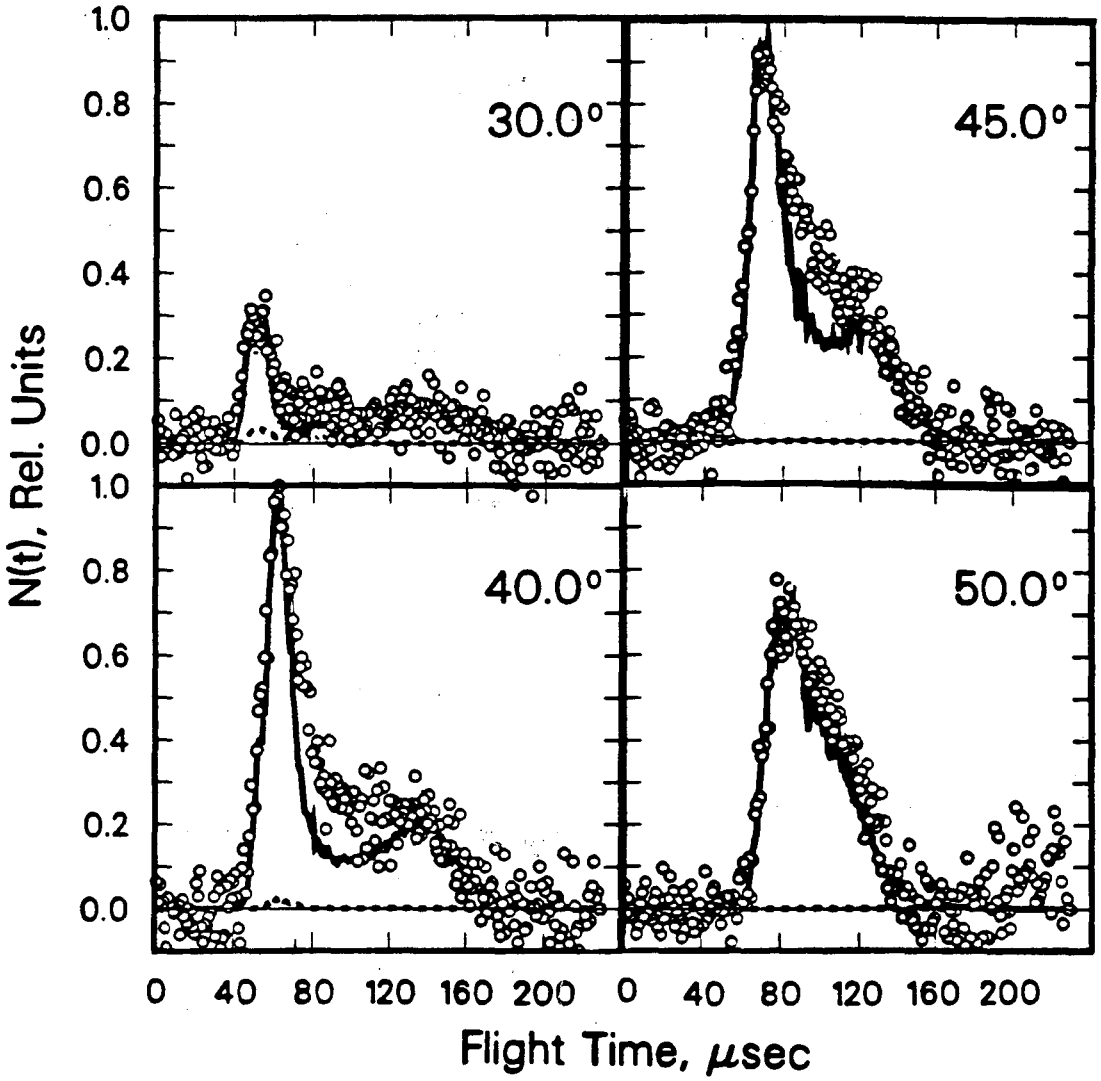
30.0°
45.0°
40.0°
50.0°
N(t), Rel. Units
1.0
0.8
0.6
0.4
0.2
0.0
0 40 80 120 160 200
Flight Time, μsec
XBL 904-1390

Figure 25

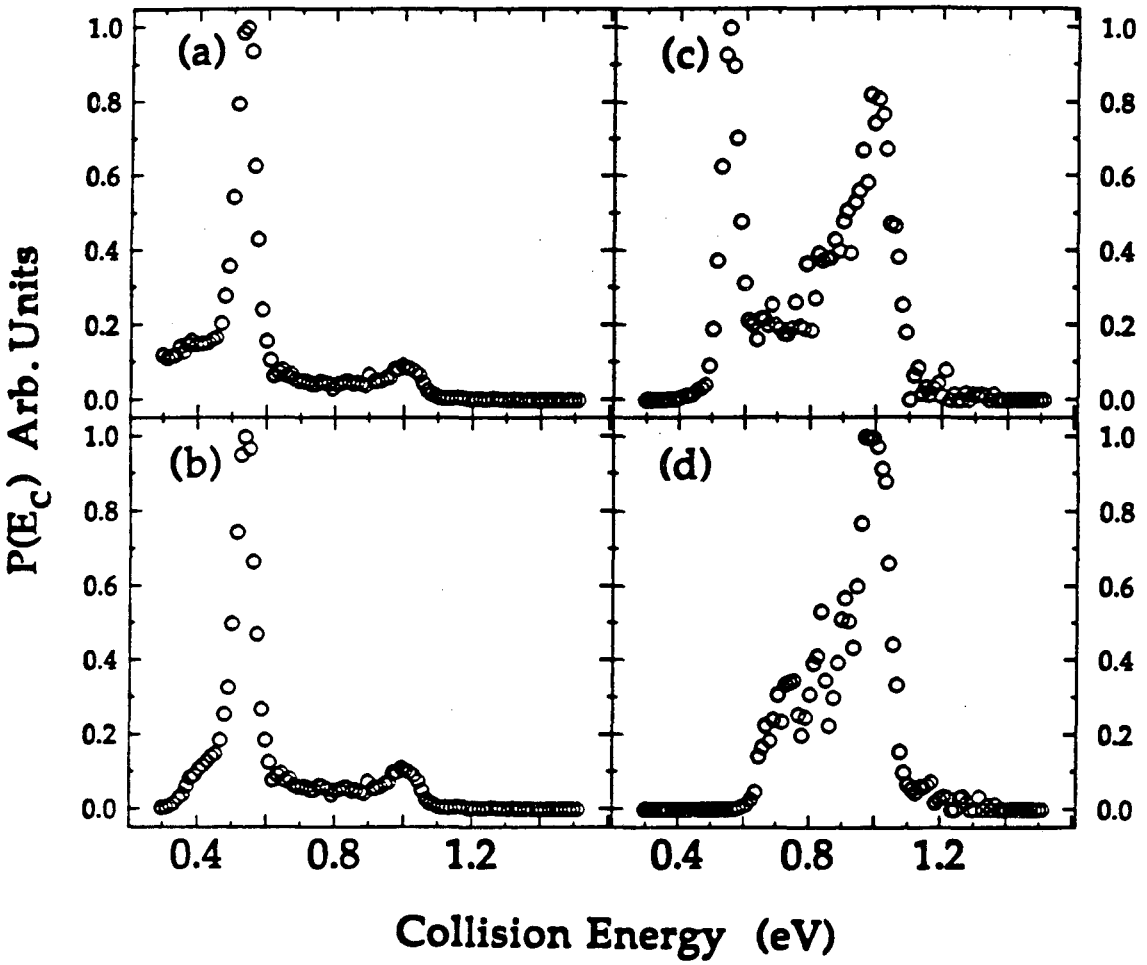
(a)
(c)
(b)
(d)
1.0
0.8
0.6
0.4
0.2
0.0
0.4
0.8
1.2
P(E_C) Arb. Units
Collision Energy (eV)
XBL 904-1404

Figure 26

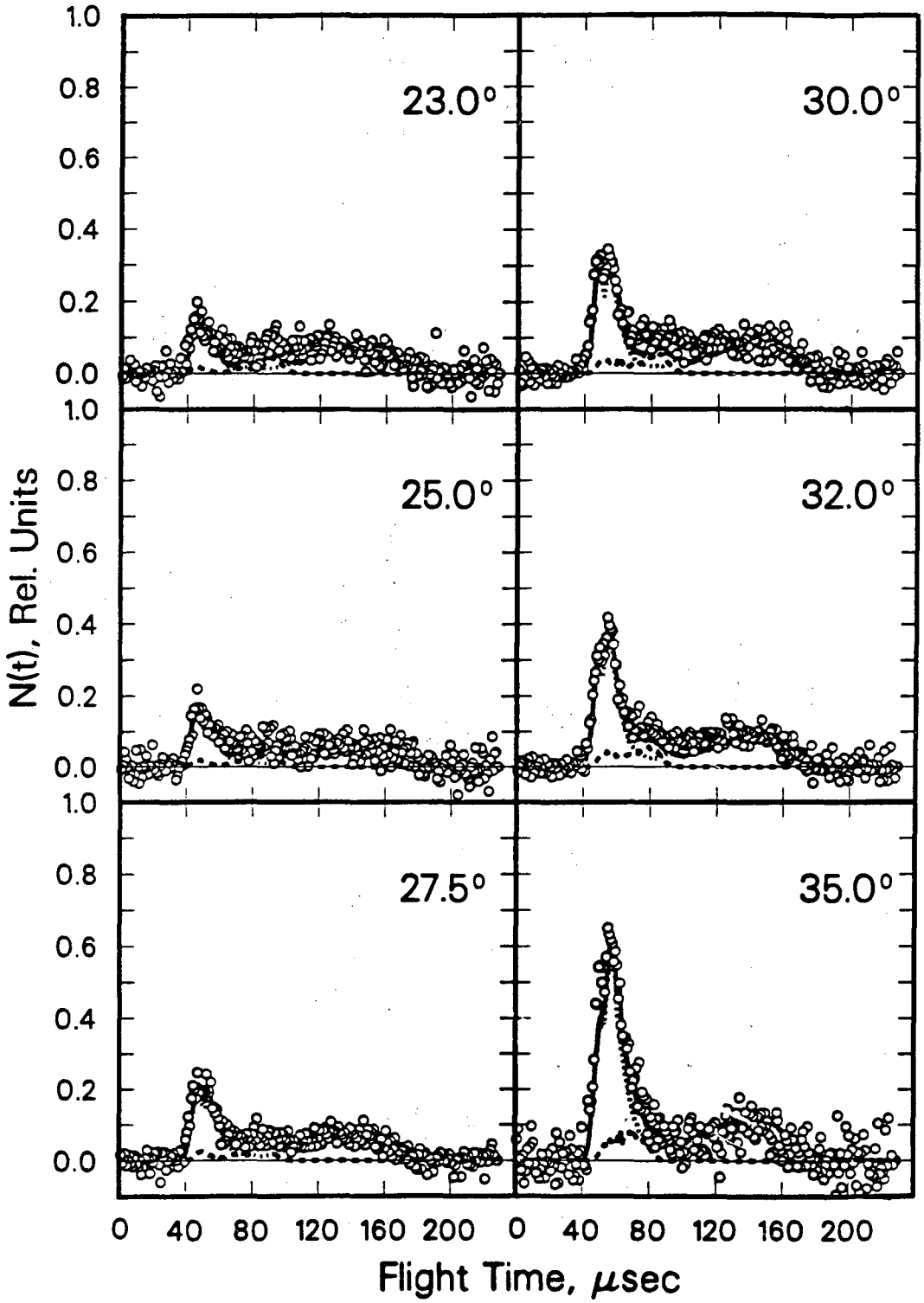
23.0°
30.0°
25.0°
32.0°
27.5°
35.0°
N(t), Rel. Units
Flight Time, μsec
0
40
80
120
160
200
0.0
0.2
0.4
0.6
0.8
1.0
XBL 904-1379

Figure 27a

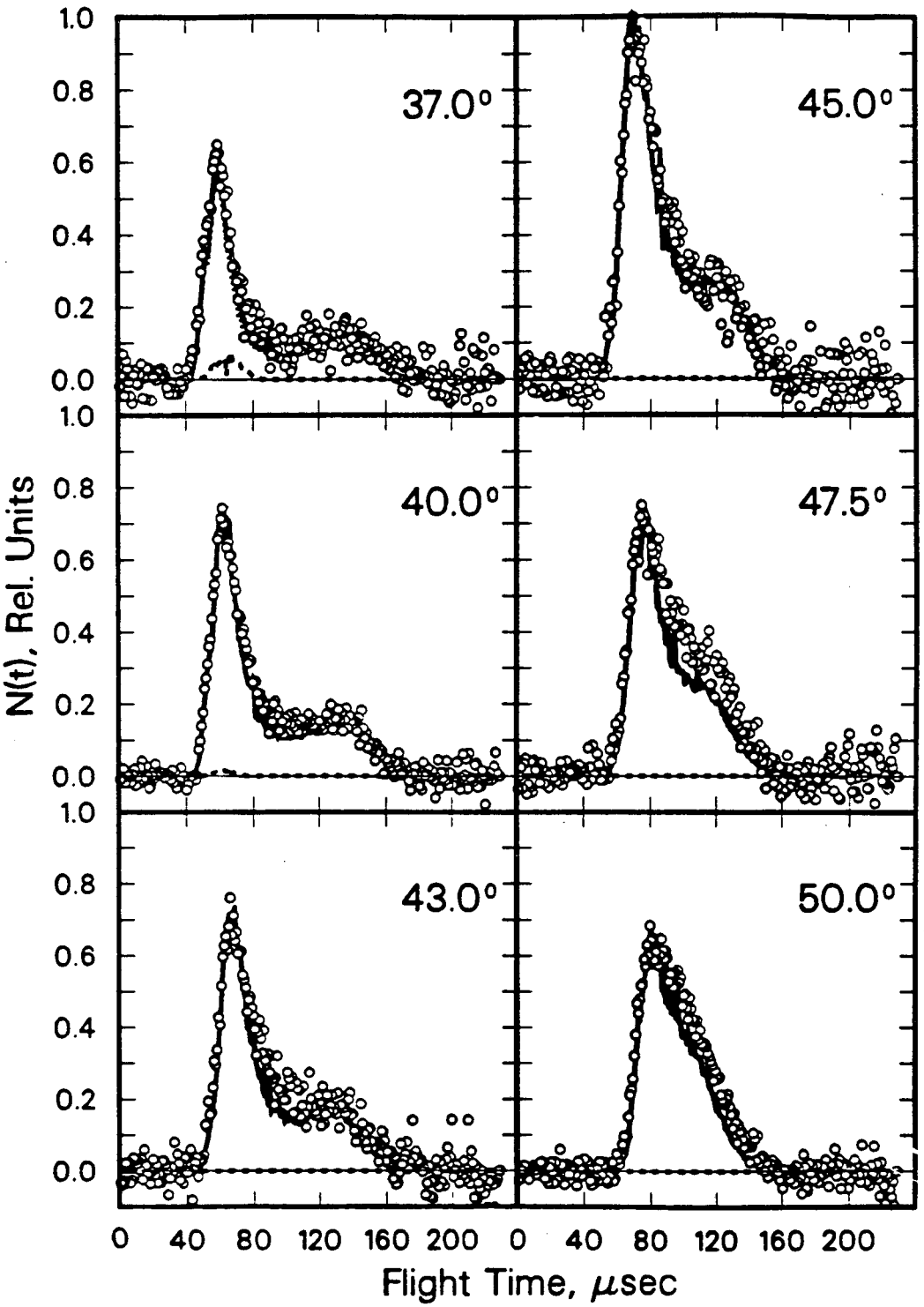
37.0°
45.0°
40.0°
47.5°
43.0°
50.0°
N(t), Rel. Units
1.0
0.8
0.6
0.4
0.2
0.0
0 40 80 120 160 200
Flight Time, μsec
XBL 904-1392

Figure 27b

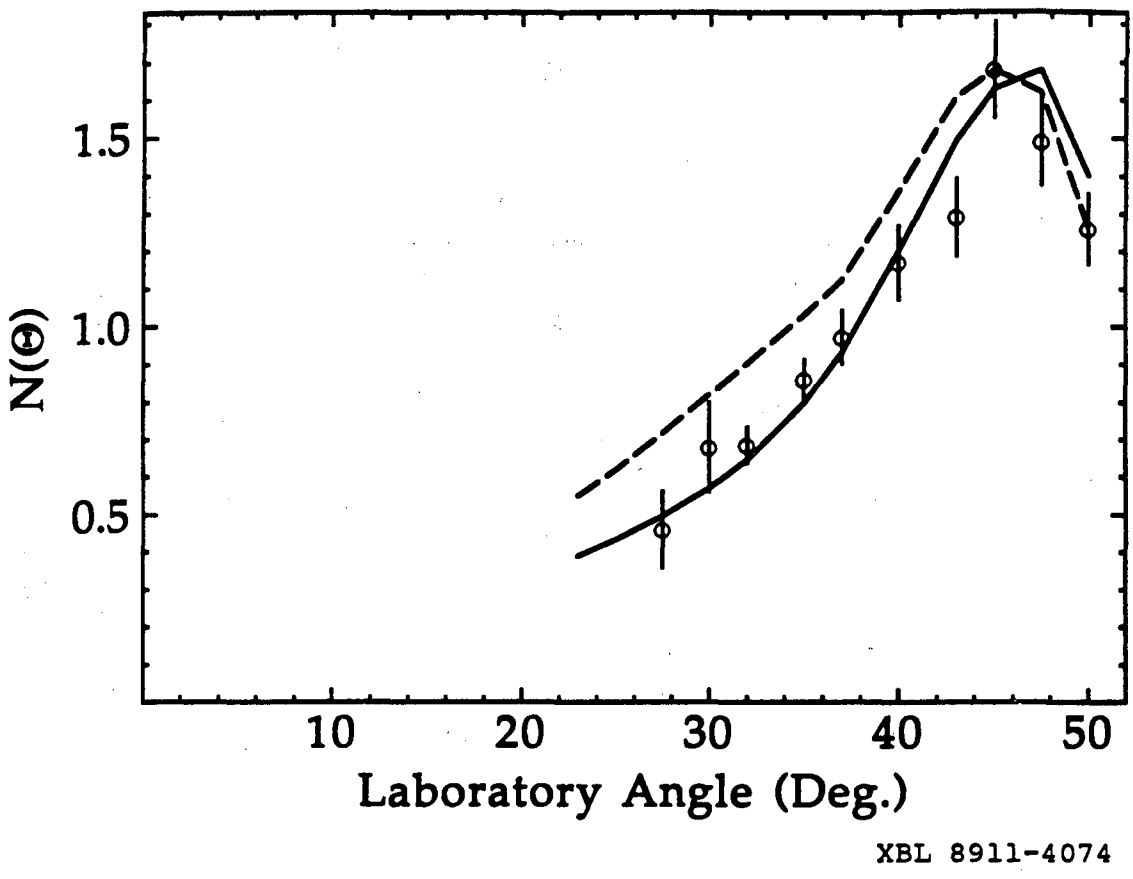

Figure 28

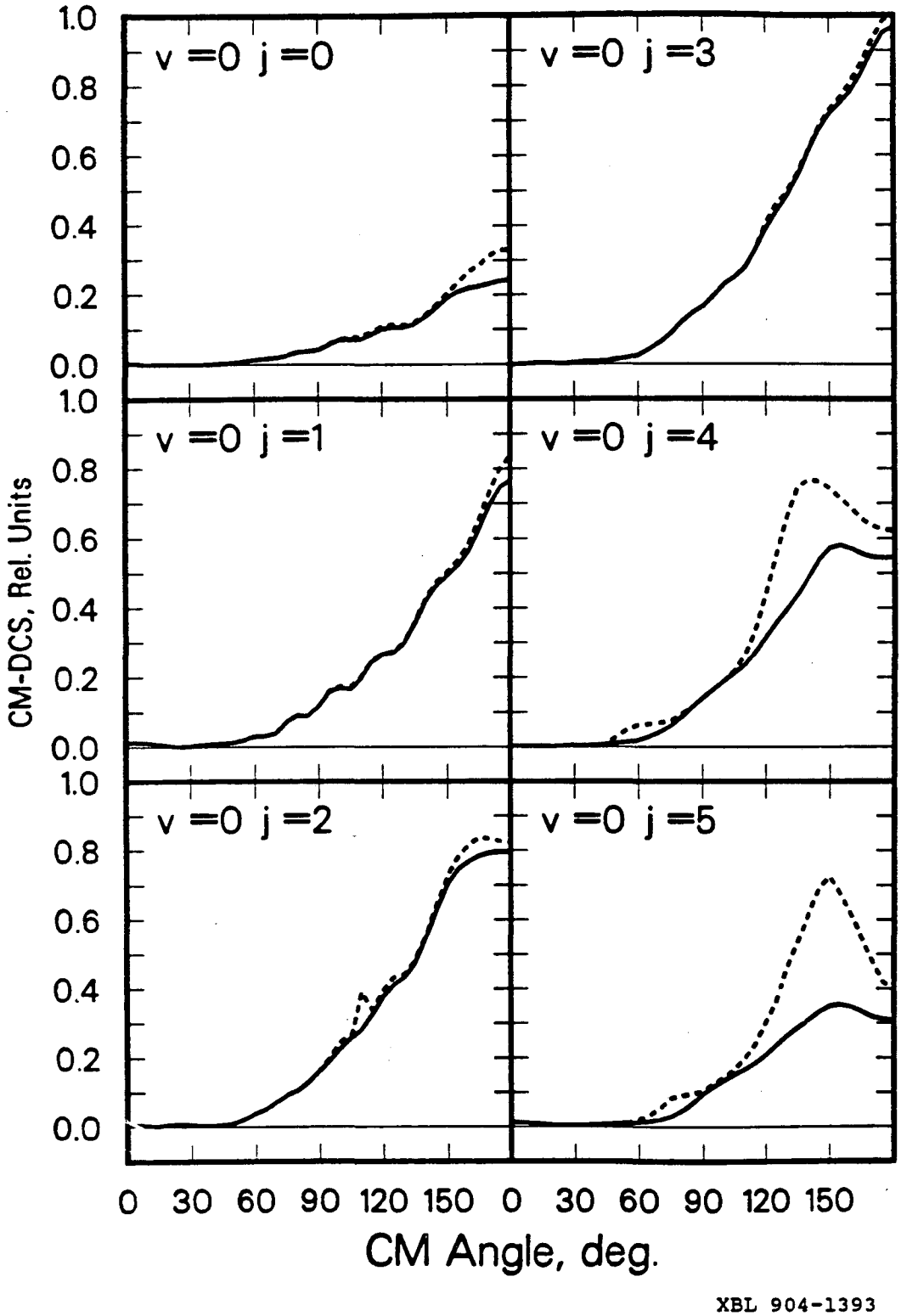
v =0 j =0
v =0 j =3
v =0 j =1
v =0 j =4
v =0 j =2
v =0 j =5
CM-DCS, Rel. Units
1.0
0.8
0.6
0.4
0.2
0.0
0 30 60 90 120 150 0 30 60 90 120 150
CM Angle, deg.
XBL 904-1393

Figure 29a

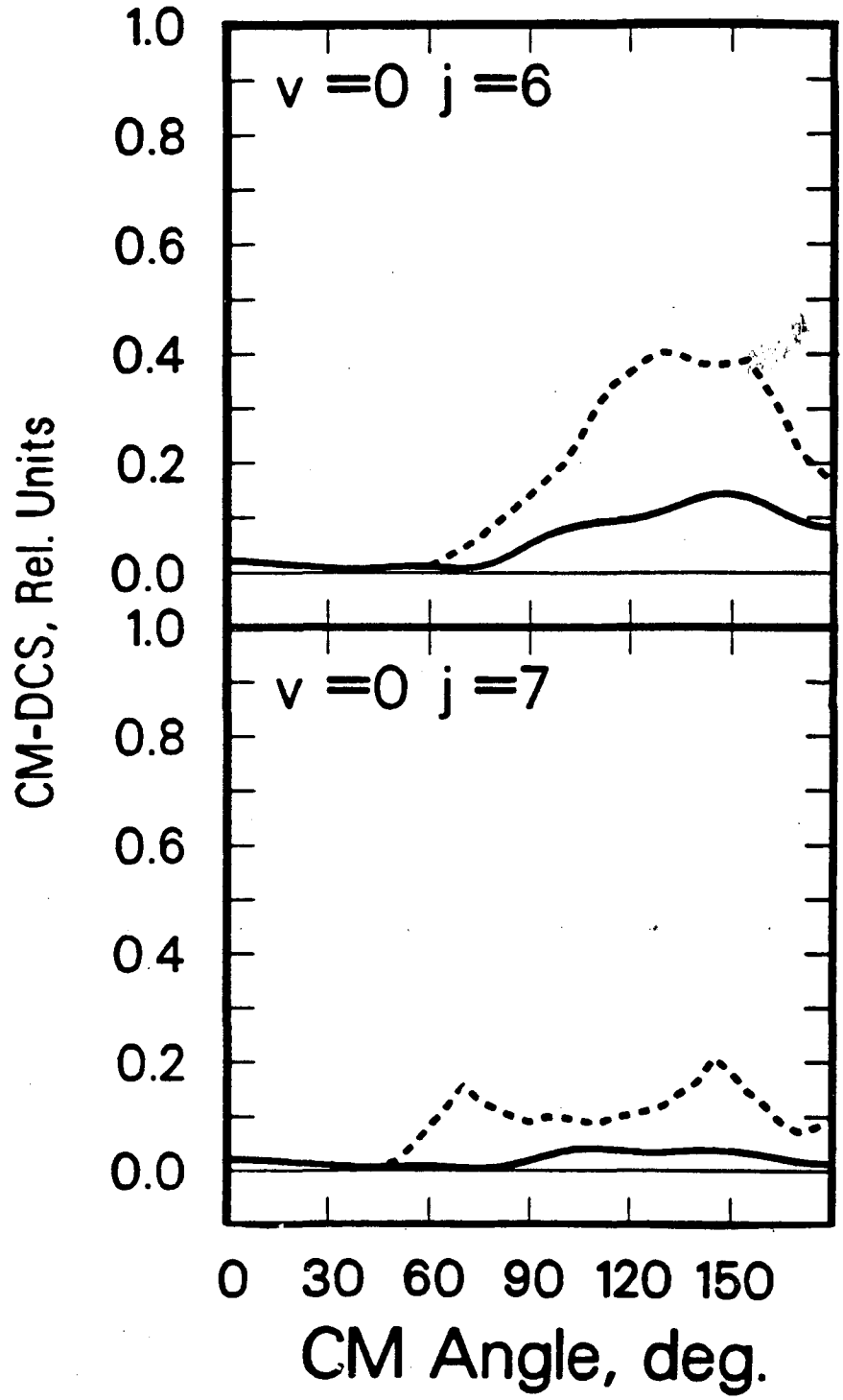
v =0 j =6
v =0 j =7
CM-DCS, Rel. Units
1.0
0.8
0.6
0.4
0.2
0.0
0 30 60 90 120 150
CM Angle, deg.
XBL 904-1394

Figure 29b

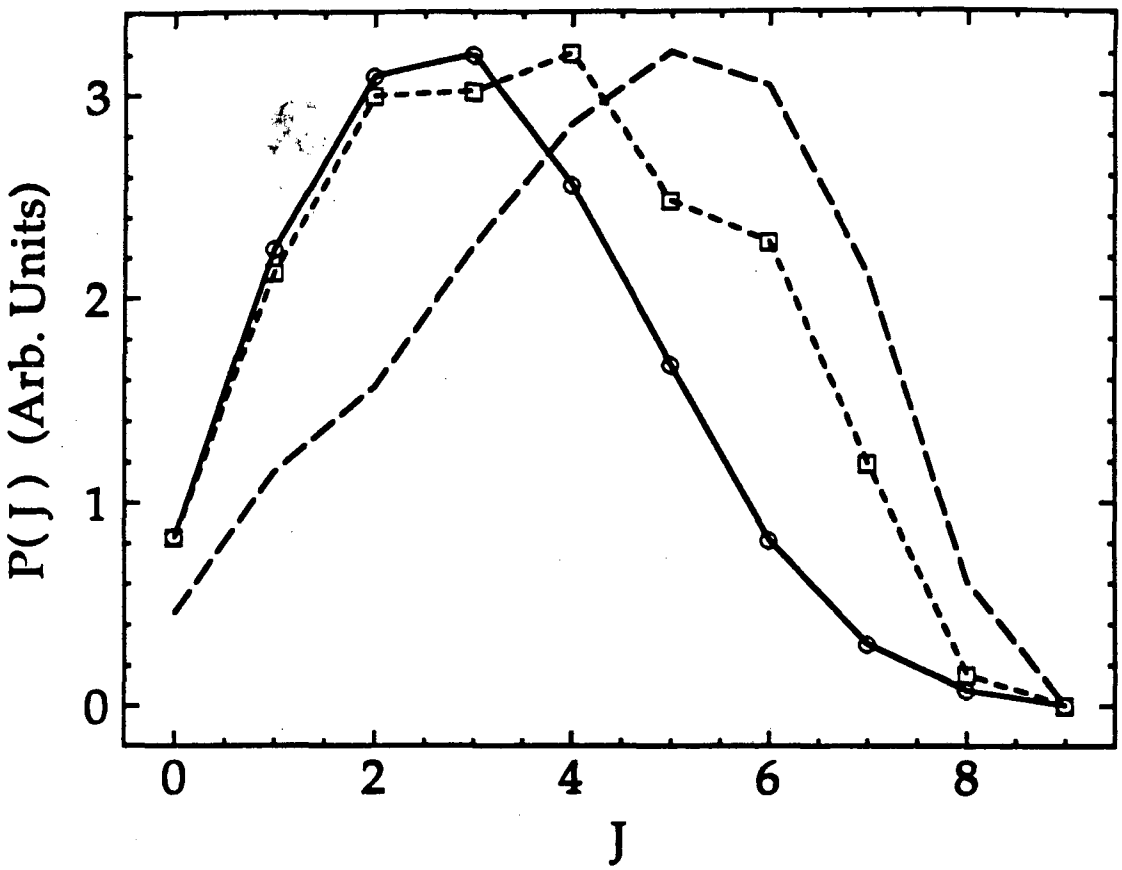

Figure 30

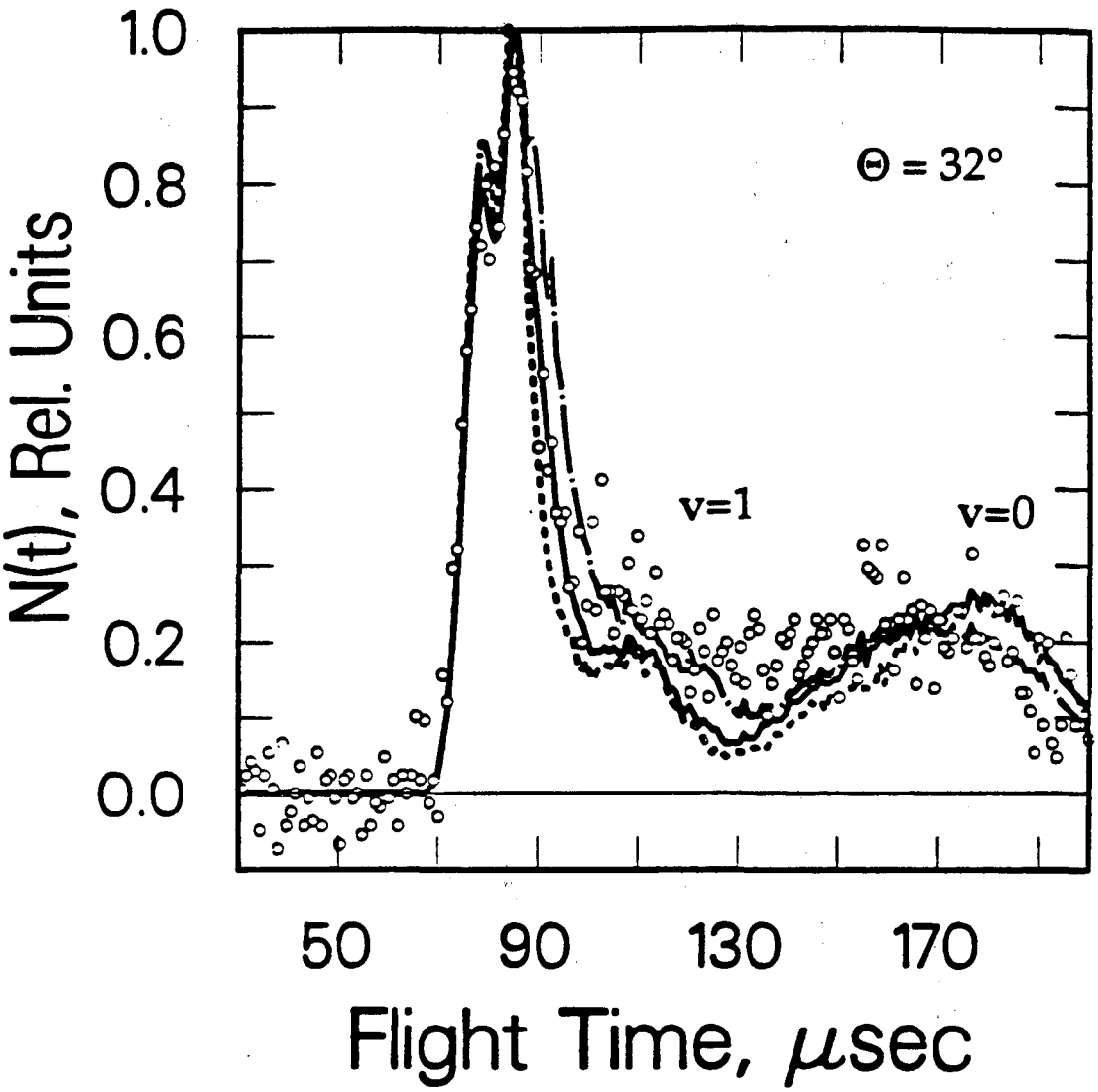
1.0
0.8
0.6
0.4
0.2
0.0
N(t), Rel. Units
Θ = 32°
v=1
v=0
50
90
130
170
Flight Time, μsec
XBL 904-1402

Figure 31

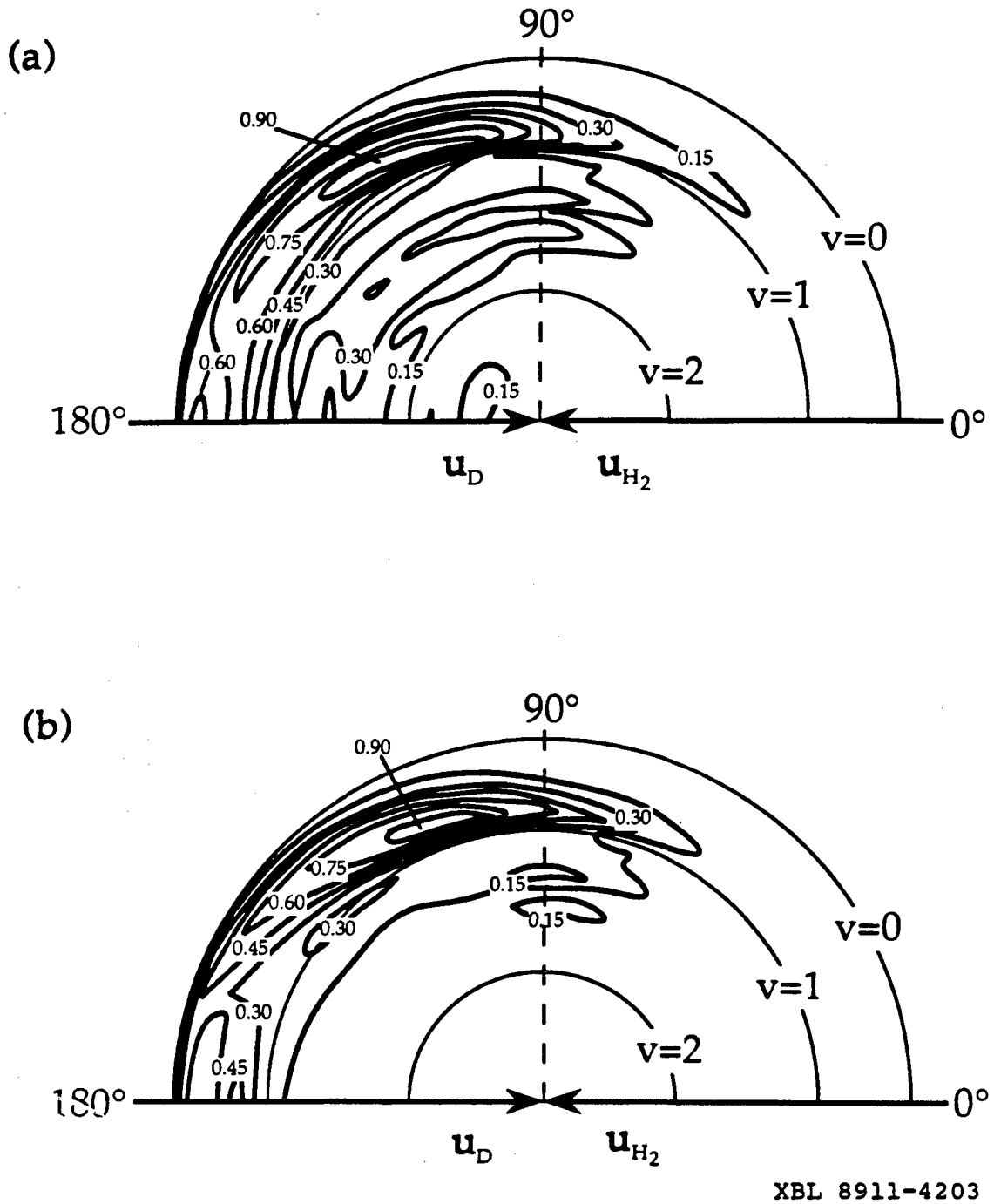
(a)
90°
0.90
0.30
0.15
0.75
0.30
0.45
0.60
0.60
0.30
0.15
0.15
v=0
v=1
v=2
180°
0°
u_D
u_{H_2}
(b)
90°
0.90
0.30
0.75
0.15
0.60
0.30
0.15
0.45
0.30
0.45
v=0
v=1
v=2
180°
0°
u_D
u_{H_2}
XBL 8911-4203

Figure 32

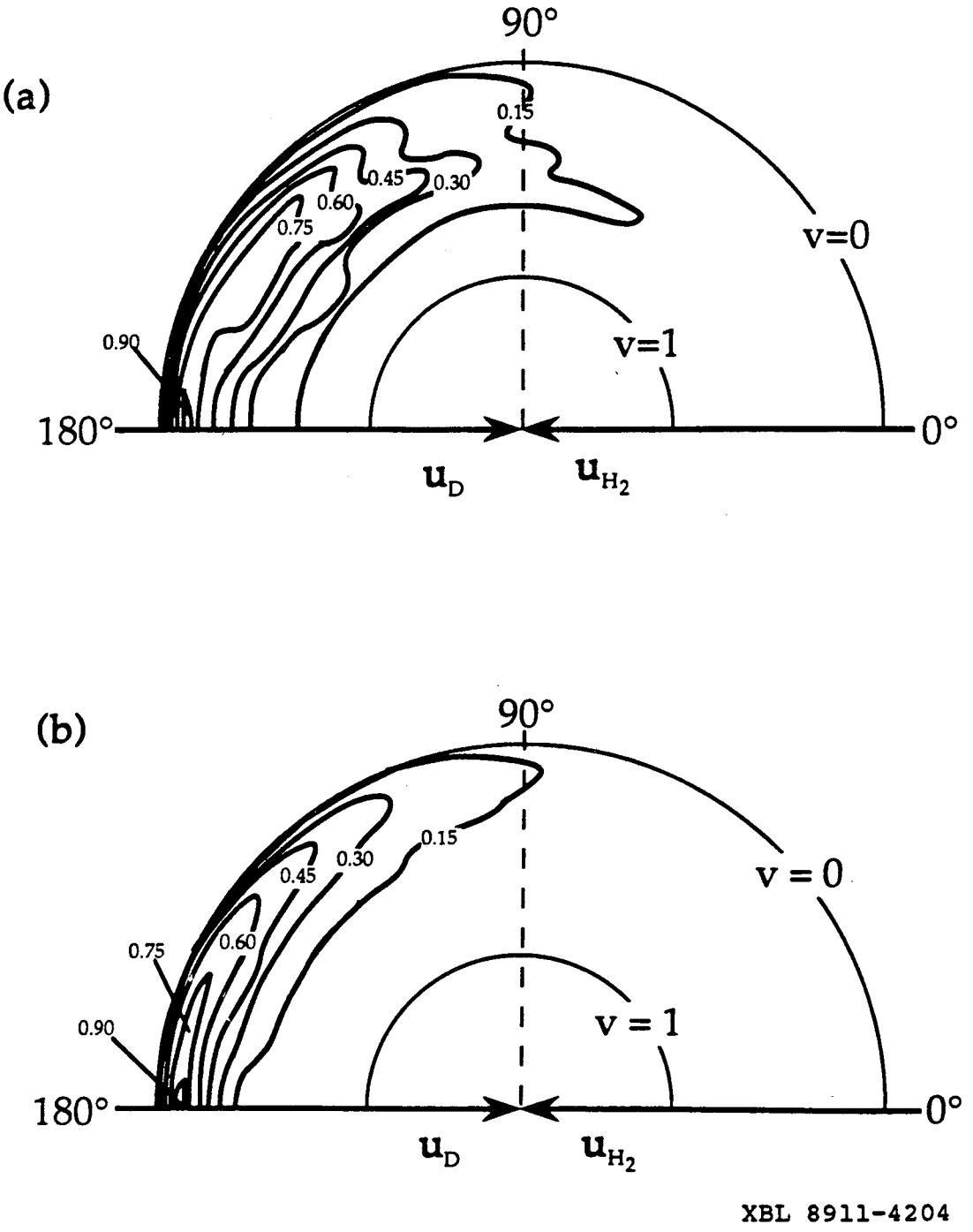
(a)
90°
0.15
0.45
0.30
0.60
0.75
v=0
0.90
v=1
180°
0°
u_D
u_{H_2}
(b)
90°
0.15
0.30
0.45
v = 0
0.75
0.60
0.90
v = 1
180°
0°
u_D
u_{H_2}
XBL 8911-4204

Figure 33

LAWRENCE BERKELEY LABORATORY
UNIVERSITY OF CALIFORNIA
INFORMATION RESOURCES DEPARTMENT
BERKELEY, CALIFORNIA 94720